分 类 号： O572　　单位代码： 10422
密　　级： 公开　　学　　号： 201311369

山东大学
SHANDONG UNIVERSITY

博士学位论文

Thesis for Doctoral Degree

论文题目： Measurement of Transverse Single Spin Asymmetry for π^0 at Forward Direction in 200 and 500 GeV Polarized Proton-Proton Collisions at RHIC-STAR

作者姓名 朱展文
学院名称 前沿交叉科学青岛研究院
专业名称 粒子物理及原子核物理
指导老师 徐庆华教授
合作导师 Elke C.Aschenauer研究员

2019年12月30日

原　创　性　声　明

本人郑重声明：所呈交的学位论文，是本人在导师指导下，独立进行研究所取得的成果。除文中已经注明引用的内容外，本论文不包含任何其他个人或集体已经发表或撰写过的科研成果。对本论文的研究作出重要贡献的个人和集体，均已在文中以明确方式标明。本声明的法律责任由本人承担。

论文作者签名：_____　日　期：_____

关于学位论文使用授权的声明

本人完全了解山东大学有关保留、使用学位论文的规定，同意学校保留或向国家有关部门或机构送交论文的复印件和电子版，允许论文被查阅和借阅；本人授权山东大学可以将本学位论文全部或部分内容编入有关数据库进行检索，可以采用影印、缩印或其他复制手段保存论文和汇编本学位论文。

（保密的论文在解密后应遵守此规定）

论文作者签名：_____　导师签名：_____　日　期：_____

Contents

List of Tables

List of Figures

ABSTRACT

The deep inelastic scattering (DIS) experiment in the 1960s for the first time uncovered the complicated structure of the proton and eventually helped to build the Quantum Chromodynamics(QCD), which in return greatly changed the picture of the proton structure. Later the research of the polarized proton structure opened a new path to the frontier of QCD. However it still remains largely unknown to the QCD community nowadays.

The results from the E704 experiment in the 1990s showed a large transverse single spin asymmetry (TSSA) in pion production, which could not be explained by leading order QCD calculations based on collinear factorization. The community proposed two approaches to explain the experimental data. One of them was the transverse momentum dependent parton distribution function(TMD-factorization) and the other one was the collinear twist-three factorization. These factorization schemes suggest nontrivial physics in the polarized proton structure.

In the TMD factorization, the Sivers function in the initial state describes the transverse motion of the partons in the polarized proton and the Collins function in the final state describes the fragmentation of a transversely polarized quark. They are considered as the main sources of the large TSSA observed in the experiment. In the collinear twist-three factorization, the higher twist distribution and fragmentation functions which are brought by quark-gluon correlation are considered the origin of the TSSA. The two approaches can be connected to each other in some circumstances. These proposed functions can be accessed in SIDIS and electron-positron annihilation experiments, and used to predict the TSSA in proton-proton collision.

Asymmetries in the production of final state particles from collider or fixed-target experiments with polarized beams or target can provide valuable information on the spin structure of the proton. In RHIC, the high polarization and high luminosity proton beam offer a unique opportunity to study the proton structure in the polarized proton-proton collision. In this thesis, the STAR Forward Meson Spectrometer (FMS), which is an electromagnetic calorimeter with a coverage of $2.5 < \eta < 4.1$ is used to measure the π^0 TSSA, electromagnetic jet TSSA and Collins asymmetry for π^0 in an electromagnetic jet.

Multiple corrections and improvements are made to the photon reconstruction algorithm for the FMS to get better precision for the analysis. They include taking

the vertex position into consideration, correcting the non-linear gain of the FMS and building an asymmetric shower shape model to neutralize the incident angle effect. The result of the π^0 reconstruction shows that these modifications are effective and provide a solid base for the analysis.

In this thesis, the TSSAs of two different datasets from Run11 ($\sqrt{s} = 500GeV$) and Run15 ($\sqrt{s} = 200GeV$) are measured, which provide a wide kinematic range for the TSSA. The 500 GeV data is the first of its kind. The result shows that the TSSAs arise as the Feynman-x(x_F), which is consistent with the previous experiments. Comparing with other measurements, it shows that the TSSAs weakly depend on the collision energy from 19.6 GeV to 500 GeV. The TSSA results are consistent with a theoretical prediction based on TMD factorization.

The topological dependence of the TSSA is also examined. It means that it divides the π^0 sample into two groups, which are the isolated π^0 and the non-isolated π^0. The isolated π^0 means there are no other particles around. Whether a π^0 is isolated is determined by its energy fraction inside a jet. Such distribution shows that there is a clear separation of the two different groups. The TSSAs of the isolated π^0 are significantly larger than the that in non-isolated π^0. It suggest that this type of π^0 is the main source of the large TSSAs. It could be related to the diffractive process in the proton-proton collision which is not well known so far.

In this thesis, the electromagnetic jet TSSA is also measured in 200 and 500 GeV. Since there is no fragmentation involved, the jet TSSA is considered only related to the initial effect. The result shows that the electromagnetic jet TSSA arise as x_F, and the trend seems to be independent of collision energy, which is consistent with the π^0 TSSA. However, the electromagnetic jet TSSA is much smaller than the π^0's at the same x_F. Due to the missing charged hadrons, the electromagnetic jet TSSA result is not contradicting with the one measured in ANDY experiment which construct a full jet.

In this thesis, the Collins asymmetry of π^0 in an electromagnetic jet is also measured to better separate initial state effect from final state effect. The Collins asymmetry is considered from the transversity and Collins fragmentation function which relates to the final state effect. The results show that the Collins asymmetries in both datasets are consistent with zero within the uncertainty, which is in agreement with a theoretical prediction based on collinear twist-3 factorization.

The above measurements together shows a full scope of the understanding the

π^0 TSSA. But due to the limitation of the detector, the results in this thesis cannot give a final proof of the origin of the TSSA. A more precise measurement will be performed after the STAR forward upgrade program. The STAR forward upgrade consists of a new tracking system and a new calorimeter system. It will offer high precision TSSA and Collins asymmetry measurement and allow to extend them to charge pions and other particle species, which will provide valuable data in understanding the origin of the TSSA, testing the different factorization schemes and finally probing the transversely polarized proton structure.

Key words: Polarized proton structure, Transverse single spin asymmetry, Collins asymmetry, TMD factorization, Collinear twist-three factorization

Chapter 1 Introduction

In the past century, there are a lot of great achievements in particle physics, the discovery of fundamental particles, the creation of the standard model, the construction of the powerful Large Hadron Collider at CERN (European Organization for Nuclear Research). Any one of them could be listed at the top rank in the hall of fame of science. However, if one asks a naive question to any top scientist in the world, "do we truly understand the proton, the little particle that was discovered one hundred years ago and exists in literally everything we see and touch?" The answer may be surprising for many people. Although great advancements have been made in the past few decades, we are still far away to answer some of the basic questions, such as how the proton spin is made of its constituent quarks and gluons and what is the confined movement of the quarks and gluons inside a proton.

The work of this thesis is aiming to study the latter one in experiment, and hopefully will be able to uncover the final answer. In this chapter, the history of proton structure study will be reviewed and a detailed motivation for the analysis presented in this thesis will be discussed.

1.1 Unpolarized Proton Structure

Unlike the electron, neutron, and nucleus, the discovery of the proton did not come from a specific experiment, but came from all three of the experiments that discovered the above three particles in some way. After the discovery of the electron, people realized there should be positively charged particles along with the electron to construct a neutral atom. The discovery of the nucleus not only demonstrated that these positive charges concentrated in a very small volume in the atoms, but also that the hydrogen nucleus played an important role in it. Later, people used the word "proton" for hydrogen nuclei as a part of the nucleus. As the neutron was discovered in 1932, people finally understood that the proton, neutron, and electron together were the basic elements that formed a general atom.[1]

1.1.1 From DIS to QCD

There is one question though, is the proton a point-like fundamental particle or can it be divided into even smaller new particles? Today we know that the electron together with its lepton family are fundamental particles, while the proton and neutron are not. One can even connect the fundamental particles with their interaction together in quantum field theory and propose the "standard model", which is one of the greatest triumphs in the history of science, see Figure(1.1). But 70 years ago, the question could not be answered. The breakthrough came from the SLAC (Stanford Linear Accelerator Center)-MIT fixed target experiment in deep inelastic scattering (DIS). The inelastic scattering means that the struck proton cannot keep intact in the collision. The "deep" in DIS refers that the momentum transfer $Q^2 >> M^2$, with M being the nucleon mass. The electron beam energy at SLAC was up to 20 GeV, which provided enough momentum transfer to the proton. An illustration of DIS is shown in Figure(1.2). For convenience, the independent variable used in DIS is chosen as momentum transfer Q^2 and Bjorken scaling variable x, where $Q^2 = -(k - k')^2$ and $x = \frac{Q^2}{2q \cdot p}$. The cross section of DIS cannot be calculated analytically. Compared to the elastic scattering, the parameterized cross section can be written as Equation(1.1), where the structure functions F are as functions of Q^2 and x.

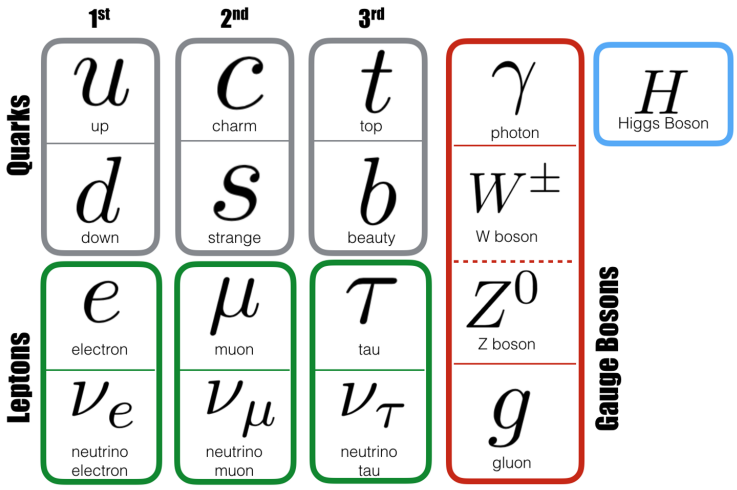

Figure 1.1: The fundamental particles in the standard model.

$$\left(\frac{d^2\sigma}{dE'd\Omega}\right) = \frac{(\alpha\hbar)^2}{4E^2\sin^4(\theta/2)}\left(\frac{F_2}{(E-E'}\cos^2\left(\frac{\theta}{2}\right) + 2\frac{F_1}{M}\sin^2\left(\frac{\theta}{2}\right)\right) \tag{1.1}$$

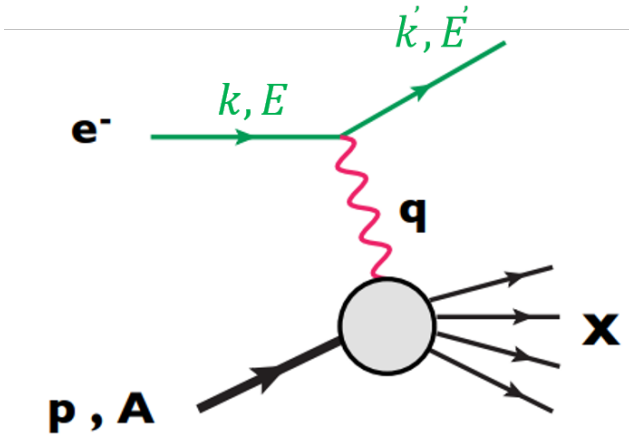

Figure 1.2: The deep inelastic scattering process.

Two important phenomena were observed in the DIS experiment: 1.) The inclusive DIS cross section is much larger than expected and only weakly Q^2 dependent. 2.) At large momentum transfer, the structure function F_2 in the in Equation(1.1) becomes a function of a single ratio $\omega = \frac{2M(E-E')}{Q^2}$. This was interpreted as point-like elementary constituents behaving as free particles inside the proton. It was a remarkable result because at this time the theory of Quantum Chromodynamics (QCD) was not yet developed. In today's point of view, when the Q^2 is large enough, the wave length of the virtual photon is small enough to probe point-like particles, which are nearly free at extremely short reaction time. But when the probe is smaller than the size of the point-like particle, the cross section is no longer sensitive to its scale. This behavior is called "Bjorken scaling" and the point-like particles are called "parton". The structure function F_2 was measured in detail in later DIS experiments. Figure(1.2) shows clearly Bjorken scaling for a modest Bjorken-x range, which is $x = 1/\omega$ from the ZEUS experiment [2].

At almost the same time, the quark model was developed by Gell-Mann and Zweig[3][4]. In the model, the already discovered baryons and mesons were assumed to be the combinations of hypothetical SU(3) triplet particles called quarks. The baryons can be constructed by three quarks as qqq and meson as $q\bar{q}$ states, where q=u,d,s represent the three flavors of quark. The proton is part of the baryon octet, made of two up quarks and one down quark, "uud", as shown in Figure(1.4). This model together with the physical interpretation of the DIS result generated the picture of proton according to the naive parton model. The

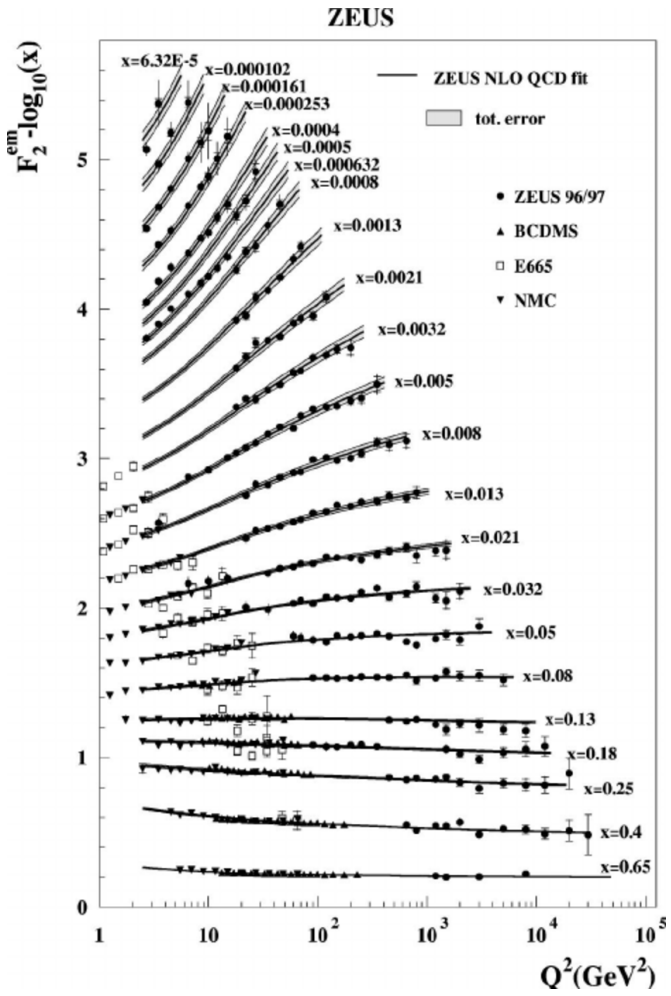

Figure 1.3: Structure function F_2 at different kinematics from ZEUS data[2].

next generation DIS and electron-positron annihilation experiments gave hints or evidence of the quark spin, charge, momentum fraction, generations and etc..

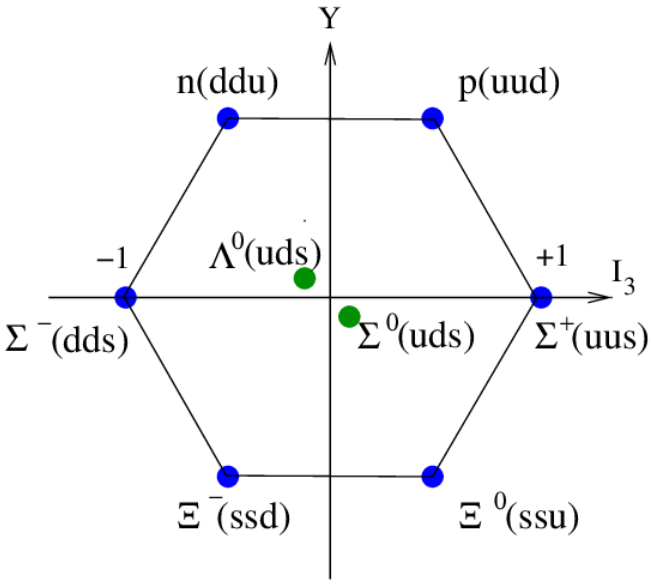

Figure 1.4: Proton in the baryon octet.

In the quark model, the Ω^- is made of three strange quark (sss) with spin $\frac{3}{2}$. This requires the three strange quarks to have their spins aligned parallel and to have vanishing orbital angular momentum, which forms a symmetric wave function. But this does not work for a fermion system. Another degree of freedom, the color, is needed to form an antisymmetric wave function. It was argued that a quark can carry one of the three "color" charges (red, green, blue), and the composite object, such as meson and baryon is a color singlet. The existing of color was proved by the cross section of hadron production in electron-positron annihilation. The color charge, similar to the electric charge in quantum electrodynamics (QED), was interpreted as a part of a gauge theory. A SU(3) gauge field theory which was named Quantum Chromodynamics (QCD) was constructed in the framework of quantum field theory to describe the interaction that binds the quarks into a proton. In this theory, the interaction between the quarks is generated by exchanging massless gauge bosons, which are named gluons.

The quark model was rather successful in explaining the hadron spectra. But individual quarks have never been observed. All the effort to produce a single quark in an experiment only results in producing a group of mesons and baryons. In the QCD theory, this is referred to as quark confinement. That refers to the interaction between quarks inside a bound state grows stronger as they are pulled

apart. The interaction is so strong that the energy of the field becomes large enough to produce quark-antiquark pairs from the vacuum. They merge with the outgoing quarks and become mesons and baryons instead of producing a single quark. That explains why no isolated quarks can be observed in experiments.

In electron-positron annihilation experiments, the virtual photon creates a quark and an antiquark, which move apart back-to-back due to momentum conservation. A bunch of particles is produced and they move roughly in the same direction due to the confinement property. Groups of particles can form a jet, whose total energy approximately equals the quark energy. This quark jet event had been observed at multiple experiments. QCD predicted that there was a chance that a quark can emit a high energy gluon. Similarly, these gluons would fragment just like the quarks and form gluon jets, which were observed in 1979 at DESY (Deutsches Elektronen Synchrotron) in three jet events [5].

On the other side, certain high energy cross sections, like the one in the DIS, suggest the quarks do not interact at all. In QCD framework, this is called asymptotic freedom which can be deduced from the property of the SU(3) gauge field. When quarks and gluons are close, the running coupling becomes so small that they act like free particles. An extraordinary feature of QCD is its ability to accommodate both kinds of behaviors. This makes QCD very different from the familiar QED. For the QED calculation, its running coupling constant is much smaller so that one is confident that the sum over the higher order processes will converge pretty quickly. In QCD, it is true only when the momentum transfer is very large so that the running coupling constant is small. The perturbative QCD calculation, often referred as pQCD, is valid under such circumstances. In the low energy case, soft processes dominate and cannot be calculated analytically. Therefore, in discussing the proton structure, the basic parameters usually can only be determined by experiment.

All these properties of QCD give a much more complex picture of the proton structure than the simple quark parton model at the beginning. Instead of three valence quarks, a lot of low momentum sea quark-antiquark pairs exist in the proton. They are continuously produced and vanish. These quarks have color charge and interact with each other by interchanging the proper color of glouns. The further they are apart, the stronger the interaction is. The gluons not only mediate strong interaction but also can interact with each other, therefore the low momentum gluon density is very high. Another influence of the gluon is that

the QCD correction due to the strong interaction introduces a mild, calculable Q^2 dependence in the PDFs [6]. In low energy, the proton looks like a soup full of quarks and gluons, which constantly keep emitting and absorbing gluons. In high energy collision, like proton-proton collision or lepton-proton scattering, the momentum transfer is large enough for the exchanged boson to probe a very small region where the interaction is weak due to the asymptotic freedom. In that way, the struck quark/gluon is likely to be free in the subprocess and fragment into a hadron when it is knocked out of the proton. The proton structure in Figure(1.5) shows the simple quark parton model on the left and the complex one with the knowledge of QCD on the right.

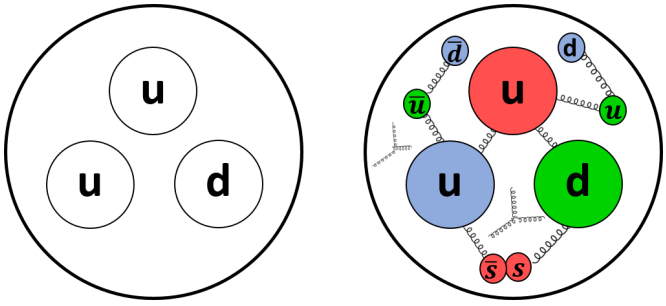

Figure 1.5: The evolution of the proton model. Left: simple quark parton model; Right: complex model based on QCD.

With this picture of the proton, to describe the partons in it, one needs a parton distribution function (PDF) for each type of quark and gluon instead of a simple number. The PDFs are functions of x, which is the momentum fraction of the parton to the parent proton. Since the PDFs directly relate to the DIS cross section, it is natural to extract their information from DIS result. Figure(1.6) shows the PDFs of quarks and gluons in the proton extracted from the ZEUS experiment data[2]. In order to describe how partons become hadrons in the experiment, a group of functions called fragmentation functions is needed. As the PDF of f_q is essentially the probability of finding a quark/gluon q in a specified hadron, the fragmentation function (FF) of D_H is the probability for a specific quark/gluon fragmenting into a final state hadron H. The PDF universality is assumed to be true for a variety of unpolarized PDFs and FFs. Therefore the PDFs extracted from DIS can be used in the more complex process like proton-proton collision where the PDF information is essential in analyzing the data.

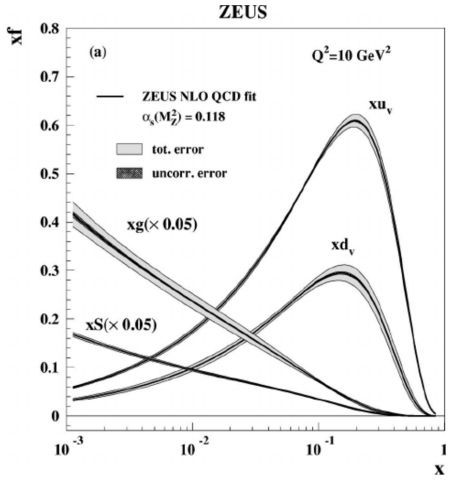

Figure 1.6: Parton distribution function extracted from ZEUS data[2].

1.2 Longitudinal Polarized Proton Structure

The above sections reviewed the exploration of the unpolarized proton structure. The success of QCD convinced the community that they now understood what was going on inside the proton. However, a surprising experimental result of polarized DIS later referred as "spin crisis" seeded some doubts.

In the simple quark model, the proton with spin 1/2 is made of three quarks whose spin is also 1/2. It would be easy to write down the combination of two spin up quarks and one spin down quark to form the spin of the proton. However, since it is known that there are more than just three valence quarks in the proton, a polarized PDF is needed to describe the quark/gluon spin structure inside a proton. The polarization direction of the proton can be either longitudinal or transverse relative to the proton momentum direction, each with profound physics. In this section, only the longitudinal one will be discussed.

The longitudinally polarized PDF can be written as $\Delta q(x)$ in Equation(1.2), which is, at momentum fraction x, the probability difference of finding a quark q whose spin direction is the aligned or anti-aligned to the spin direction of the proton spin. As comparison, the unpolarized PDF $q(x)$ is the sum of the two spin configurations rather than the difference.

$$q(x) = \overrightarrow{q(x)} + \overleftarrow{q(x)} \quad \text{œ}\Delta q(x) = \overrightarrow{q(x)} - \overleftarrow{q(x)} \tag{1.2}$$

In 1988 the European Muon Collaboration (EMC) experiment measured the asymmetry of the inclusive DIS cross sections of a longitudinally polarized muon beam scattering off a longitudinally polarized nucleon. The asymmetry A_1 in

Equation(1.3) contains the summed information of the polarized PDF. Therefore, the sum of longitudinally polarized PDFs can be accessed by the asymmetries. By comparing the results from different scattering nucleons (proton and neutron) in the experiment, one can separate the contribution from up and down quarks.

$$A_1 = \frac{\sigma_{1/2} - \sigma_{3/2}}{\sigma_{1/2} + \sigma_{3/2}} \simeq \frac{g_1}{F_1} = \frac{\sum_q e_q^2 \Delta q\,(x, Q^2)}{\sum_q e_q^2 q\,(x, Q^2)} \tag{1.3}$$

They obtained a surprising result that the total contribution from all three types of quarks/antiquarks was very small and compatible with zero [7]. Although the uncertainty was quite large, see Equation(1.4), it was clear the experimental result was contradicting with the theoretical prediction that the quark contribution should be about 60% [6]. So it became a puzzle to be solved.

$$\Delta\Sigma = \int dx(\Delta u(x) + \Delta d(x) + \Delta s(x) + \Delta\overline{u}(x) + \Delta\overline{d}(x) + \Delta\overline{s}(x)) = 12 \pm 9 \pm 14\% \tag{1.4}$$

Later, more DIS measurements were done to probe the polarized structure function $g_1(x) = \frac{1}{2}\sum_j \mathrm{e}_j^2 \left[\Delta q_j(x) + \Delta\overline{q}_j(x)\right]$ at SLAC, CERN, DESY, and Jefferson Lab. Inclusive DIS data alone, however, can not separate the contributions from quark and antiquark PDFs. Semi-inclusive DIS (SIDIS), can provide this separation. SIDIS means not only the scattering lepton, but an additional produced hadron (usually a pion or kaon) is also detected in the final state. Since the struck quarks of different flavors have a certain preference to produce a certain type of hadrons, it is possible to extract the polarized PDF of each flavor from the asymmetries of charged pion and charged kaon production in SIDIS in electron-proton and electron-neutrons scattering. Figure(1.7) shows the Particle Data Group's extraction of the polarized PDF from worldwide data. In the end, these measurements showed that the quark contribution to the proton spin is approximately 30% [8].

To hunt for the missing spin, it is important to take a look at what the possible contributions can be. One choice of decomposition is called the Jaffe-Manohar sum rule in Equation(1.5)[10]. It decomposes the proton spin into four parts: contributions from quarks $= \frac{1}{2}\Delta\Sigma$, gluons $= \Delta G$, and the angular momentum from quarks and gluons $L_q + L_g$. These terms are defined to be the proton matrix elements of free-field angular momentum operators in the infinite momentum frame. However, Ji argued that the angular momentum operators were gauge dependent. While ΔG was easyto define in the infinite momentum

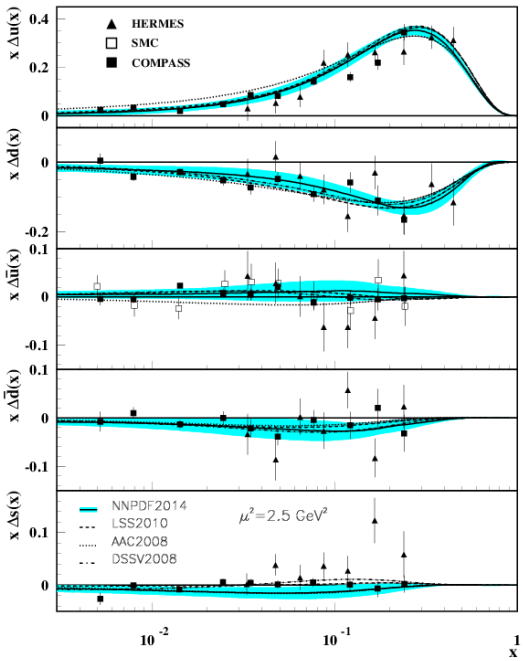

Figure 1.7: Polarized parton distribution functions $\Delta q(x)$ extracted from world wide data, compiled by the Particle Data Group[9].

frame, there was no natural gauge-invariant solution for the spin of gauge particles. Ji presented his frame-independent and gauge-invariant sum rule[11], see Equation(1.6).

Although this sounds the end of the story, there have been many efforts to validate the Jaffe-Manohar sum rule. There is a strong motivation for that because the ΔG which is hidden in the Ji sum rule is measurable in high-energy experiments, and it is easier to deal with in infinite momentum frame. On the other side, the Ji sum rule might be well defined but not quite straightforward to measure the gluon polarization in experiment. Recently, Ji proved that the Jaffe-Manohar sum rule can be related to the matrix element of a gauge-invariant, but frame-dependent operator through a matching formula in large-momentum effective field theory [12].

Disregarding the theoretical arguments, in experiment, the ΔG term is still widely used for practical reasons. In the above discussion, the quark spin contribution is about 30%, a natural suspect for the missing proton spin is the gluon contribution and the angular momentum. The angular momentum, however, still remains largely unknown to the community. A lot of efforts were dedicated to measure ΔG in experiment.

$$\frac{1}{2} = \frac{1}{2}\Delta\Sigma + \Delta G + L_q + L_g \tag{1.5}$$

$$\frac{1}{2} = J_q + J_g = \frac{1}{2}\Delta\Sigma + J_g + L_q \tag{1.6}$$

QCD has shown that the gluon plays an important role in the unpolarized PDFs. It would not be a big surprise that it is also important in polarized PDF. Theoretical calculations show that the gluon contribution depends on the renormalization scheme utilized [6]. So it needs to be constrained from experiment data. In recent years, the STAR Collaboration published the result [13] of the longitudinal double spin asymmetry in jet production, which is sensitive to the subprocess of quark-quark, quark-gluon or gluon-gluon scattering. The DSSV group has performed a global analysis [14] and showed the first evidence of non-zero $\Delta G(x)$. Figure(1.8) shows the integral of $\Delta G\left(x, Q^2 = 10\text{GeV}^2\right)$ over the range $x > 0.05$ is $0.20^{+0.06}_{0.07}$ at 90% C.L.. It indicates that the STAR jet data lead to the positive gluon polarization in the RHIC kinematic range.

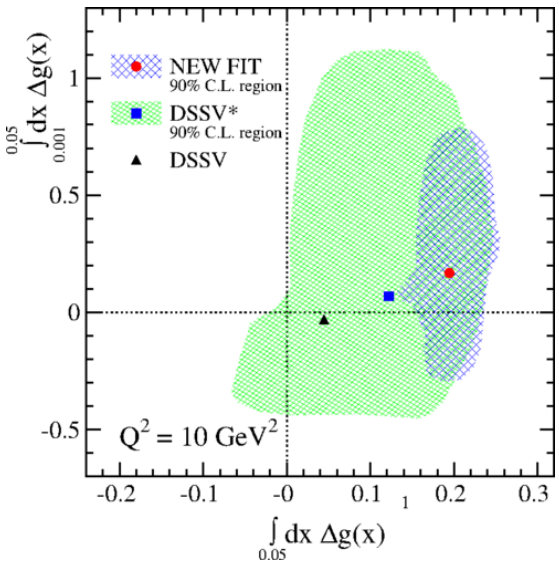

Figure 1.8: $\Delta G(x)$ from a global fit of the DSSV group comparing the previous fit results for DSSV, DSSV*, with the symbols corresponding to the values of each central fit [14].

1.3 Transversely Polarized Proton Structure

Similar to the longitudinal polarized proton structure, the transverse one draws a lot of attention in the community due to an unexpected experimental

result: the large transverse single spin asymmetries in pion production in proton-proton collisions[8]. These have been a hot topic in proton structure for more than a decade.

1.3.1 Transverse Single Spin Asymmetry

The transverse single spin asymmetry (TSSA) refers to the difference of cross section for different polarization direction in polarized scattering experiments, in which one beam/target is transversely polarized, and the other unpolarized. It could be done in DIS, proton-proton collisions, p-nucleon collisions, which associate with different underlying physics. A general form of the asymmetry, often written as A_N is shown in Equation(1.7).

$$A_N = \frac{d\sigma^{\uparrow} - d\sigma^{\downarrow}}{d\sigma^{\uparrow} + d\sigma^{\downarrow}} \tag{1.7}$$

Unlike the usually small longitudinal asymmetries, many of the TSSAs for the produced hadrons are large. The first large TSSA result was reported by an experiment of polarized proton-proton collision at 5 GeV in the zero-gradient synchrotron (ZGS) in Argonne National Laboratory [15]. Later around 1990, several experiments [16][17] were done in Fermi National Accelerator Laboratory (FNAL) which drew the same conclusion with better precision. The FNAL E704 experiment reported large asymmetries of charged and neutral pion production in fixed target polarized proton-proton collision with center of mass energies as high as 19.4 GeV. For charged pions, the TSSA is as large as 0.3 at high x_F. Later proton-proton collision experiments at RHIC with more statistics and better precision also validated the earlier results. Figure(1.9) shows the TSSAs in pion production in proton-proton collision at RHIC. These experiments were done at multiple collision energies and plotted as function of the Feynman-x (x_F), which equals to the longitudinal momentum of the hadron over the momentum of the polarized proton beam. It can be seen that the asymmetries rise with x_F. To measure the asymmetry in large x_F, it is preferable to do the measurement at forward rapidities. In this thesis, the measurement of pion production is performed at the forward rapidity region at the STAR detector.

This non-trivial result drew much attention from the QCD community. Because calculation based on the collinear QCD factorization framework predicted a much smaller asymmetry, due to the suppression from the Chiral-odd nature of the PDF for transversely polarized quarks [19]. It has to couple with anoth-

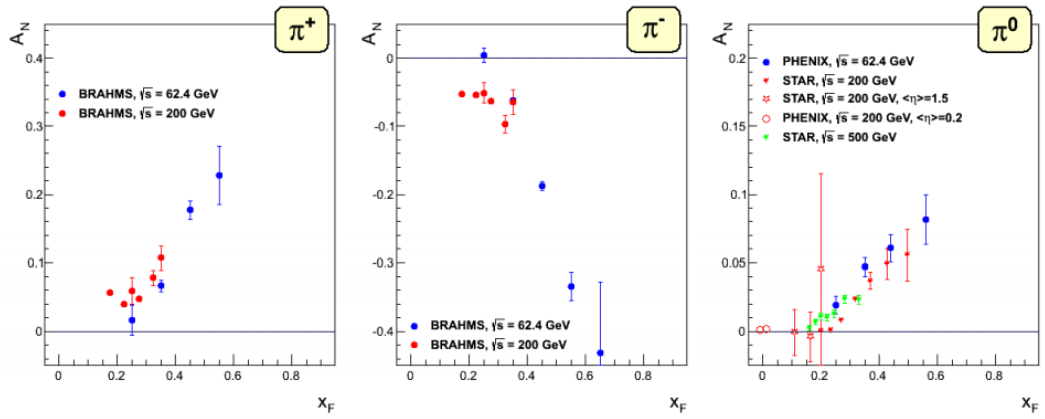

Figure 1.9: Transverse single spin asymmetry measurements at RHIC for charged and neutral pions at different center-of-mass energies as function of Feynman-x [18].

er chiral-odd counterpart because chirality for massless particle is conserved in strong interactions. In this way, the calculated asymmetry is highly suppressed. The obvious contradiction triggered theoretical and experimental interest.

On the theory side, a lot of efforts were put to build models that can generate large TSSAs. Most of them can be categorized into two sets. One is based on the Transverse Momentum Dependent (TMD) factorization and the other is called twist-three collinear factorization. Both of these two approaches concern the quark-gluon correlation but in a slightly different way and generally deal with different processes with different scale requirements. A paper [20] explored the relation of the two factorizations. It proved that both factorizations were describing the same physics in the kinematic region where they overlap.

On the experimental side, both in DIS and proton-proton collision experiments, people probe these new distribution functions by observing different processes and compares them to models, such as SIDIS and Drell-Yan measurements in the HERMES [21] and COMPASS [22] collaborations and the Jlab multi-Hall experiments [23]. It is also one of the important motivations for the future Electron Ion Collider (EIC) [24], as discussed in the EIC white paper. Although there is a lot of progress in understanding TMDs, however, many aspects of TMDs remain unexplored. Current measurements are greatly limited due to the restricted kinematic coverage or low luminosity beams or both for the existing facilities.

In this thesis, we are probing the transverse single spin asymmetry for π^0 using the process of $p^{\uparrow} + p \to \pi^0 + X$, at large pseudo-rapidity at STAR to study

the origin of the transverse single spin asymmetry

1.3.2 TMD Factorization

In early leading twist collinear factorization scheme, the parton distribution functions are expressed in one-dimension, the parton longitudinal momentum fraction. The transverse momentum of the partons is either considered negligible or integrated in the first step. So it is presumed that the cross section does not depend on the transverse momentum of the partons. As it is mentioned above, this theory cannot explain the large TSSAs. A group of distribution functions and fragmentation functions which are dependent on the parton transverse momentum (parton k_T) were proposed as a solution.

At leading twist, eight TMD distribution functions for quark initial state are proposed, see Figure(1.10). There are complementary fragmentation functions as well. This table illustrates the spin configuration of quarks and protons. The columns correspond to the three quark polarization states, while the rows are the three proton polarization states. The direction of the momentum of the proton is presumed to go to the right and the arrow pointing perpendicular to this direction means it is transversely polarized. For example, the top left corner shows the trivial unpolarized parton distribution $f(x)$ representing the probability of finding an unpolarized parton in an unpolarized proton. The one in the middle is the above-mentioned helicity distribution g_{1L} representing the probability difference of finding a parton with its helicity aligned or anti-aligned to the proton spin. The rest of them are new TMD PDFs. For example, the bottom left one $f_{1T}^{\perp}$ is called the Sivers function, representing the probability difference of finding an unpolarized parton in a transversely polarized proton with different polarization direction. This is the function first introduced by Sivers to explain the large TSSAs [25]. The definition of the remaining functions can be deduced from the polarization indicated by the arrows.

Note that the two functions indicated in red $f_{1T}^{\perp}$ and $h_1^{\perp}$ are T-odd, which means they would change sign under time reversal operation. Since any QCD process should be T-even, essentially these two terms should vanish in the calculation. However, it had been proven that they can exist if multi-parton correlations are considered. This would be mentioned in detail in the following discussion of the Sivers function. Another feature worth mentioning is that the four functions in the last column are chiral-odd, where the quark polarization is transverse. It

means that the function would change sign when apply to a chiral transformation. As it is known that the u and d quarks are approximately massless in high energy experiment, and therefore conserve chirality in strong interaction. A chiral-odd PDF alone cannot contribute to a physical observable. But it could still exist if it couples with another chiral-odd final state fragmentation function. For example, the transversity h_1 in the upper right corner of the table, it cannot be probed in inclusive DIS due to the chiral-odd nature. But it can be probed in SIDIS where a chiral-odd fragmentation function appears in the hardon production.

According to the TMD factorization concept, there is a two energy scale requirement for the processes that can be used to probe TMDs. It requires a large transfer momentum, as a "hard" scale, and a modest transverse momentum for the final state particle, as a "soft" scale, written as $Q \gg Q_T \geq \Lambda_{QCD}$. The QCD scale Λ_{QCD} is approximately 200 MeV. For example, in SIDIS, the momentum transfer is determined solely by the scattered lepton, which can be chosen by the appropriate scattering angle. This allows the pQCD calculation to work. It also requires that the produced hadron p_T be selected close to the QCD scale so that it is sensitive to the intrinsic transverse momentum of its parent parton. So far, some of the TMD functions, like transversity, the Sivers function, and the Collins function are measured in SIDIS and in the Drell-Yan process.

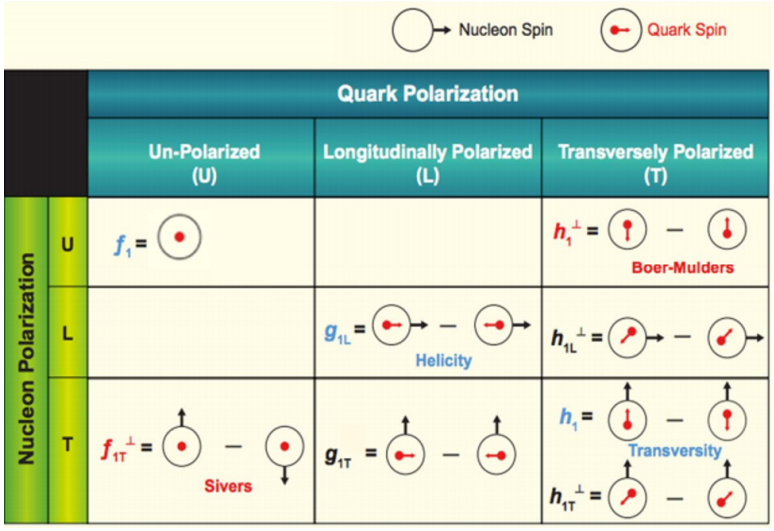

Figure 1.10: The TMD functions at leading twist.

1.3.3 Sivers function

From all the TMD functions, the Sivers function in the initial state and the Collins function in the final state are considered the major source of the large TSSA. The Sivers function was proposed by D. Sivers in 1990 as a way to explain the large pion TSSA as mentioned above [25]. It had a dramatic history in its development. The form of the Sivers function is in Equation(1.8). It states that the PDF of the quark q is composed of two parts. The first part is the trivial unpolarized part as the first term on the right of the equation. The second part shows that the parton transverse momentum coupled with the proton spin, modulated by the Sivers function. However, this particular form is considered to vanish due to the T-odd nature of the Sivers function. It means the function will change sign under time reversal transformation, which violates the principle that all physical distribution function should be T-even. In 2002, a theory study pointed out that the Sivers function could be nonzero if a final state interaction was considered[26]. Such interaction is called the gauge link. It refers to the final state interaction between the quarks/antiquarks and the proton remnant. These interactions are the keys for the Sivers function to exist.

$$\hat{f}_{q/p^{\dagger}}\left(x, \boldsymbol{k}_{\perp}\right)=f_{q/p}\left(x, k_{\perp}\right)+\frac{1}{2} \Delta^{N} f_{q/p^{\dagger}}\left(x, k_{\perp}\right) \boldsymbol{S} \cdot\left(\hat{\boldsymbol{P}} \times \hat{\boldsymbol{k}}_{\perp}\right) \tag{1.8}$$

Not for long, the HERMES experiments reported evidence of a nonzero Sivers function [27]. This was confirmed by the other experiments with better precision. These advancements forced a profound review of the transverse momentum distributions in the PDF model. Figure(1.11) shows the updated parton distribution function in the transverse-momentum plane for unpolarized quarks with $x = 0.1$ for a nucleon polarized along the y direction. The anisotropy due to the proton polarization is described by the Sivers function. The deep red(blue) zone indicates large negative (positive) values for the Sivers function. It can be seen that the u and d valence quark have the opposite preference along the direction perpendicular to the proton spin. Naturally it is related to the large TSSA in which the $\pi^{+}(u\bar{d})$ preferred outgoing to the right and the $\pi^{-}(\bar{u}d)$ to the left.

These calculations and measurements are merely first step in understanding the structure of the transversely polarized proton. Now both theory and experiment suggest that there is a rich content of physics in QCD that we still know very little off. The validity of the Sivers function or even the TMD factorization is one of the profound questions. One key prediction of the Sivers function pro-

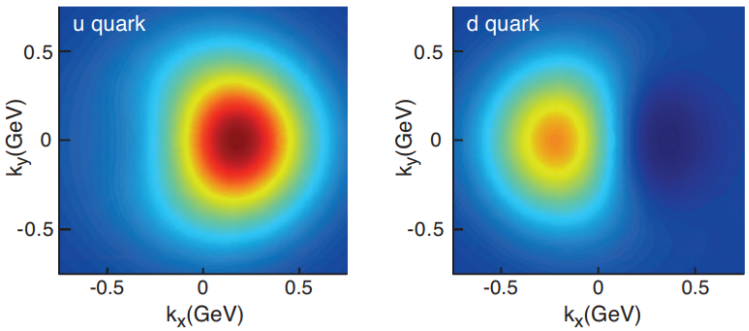

Figure 1.11: Parton transverse momentum distribution in momentum space inside a proton extracted from Sivers function. [24]

posed by J. Collins is a good validation (or falsification) [28]. In this reference, he argued that the Sivers function in SIDIS has the opposite sign compared to the one measured in the Drell-Yan process, see Equation(1.9). Based on the calculation of the gauge link, the Sivers function in SIDIS is generated by the final state interactions between the struck quark and the remnant, while in Drell-Yan process it is generated via the initial state interactions between the quark/antiquark and the remnant, see Figure(1.12). The different mechanisms result in different sign of the Sivers function. The two Sivers functions only differ in the sign. This interesting prediction will be tested by data from the COMPASS and STAR Collaboration. However, due to the limited experimental capability, the latest result is still unable to give a strong conclusion on the Sivers sign change effect. More data is needed to test the TMD factorization scheme. And it stimulates the next generation of high energy experiments to explore further, including the fore-coming EIC.

In this thesis, we are probing the transverse single spin asymmetry for the electromagnetic jet using the process of $p^{\uparrow}+p \rightarrow EM-jet+X$, at large pseudo-rapidity at STAR. Since there is no fragmentation involved, the asymmetry should reflect the Sivers effect.

$$f_{1T}^{\perp}\left(x, k_T, \zeta\right)\big|_{\mathrm{DIS}} = -f_{1T}^{\perp}\left(x, k_T, \zeta\right)\big|_{\mathrm{DY}} \tag{1.9}$$

1.3.4 Collins Asymmetry

It turns out that the TSSA is not an ideal observable to investigate the TMDs because the initial and final state effect entangle in the process. One of the most

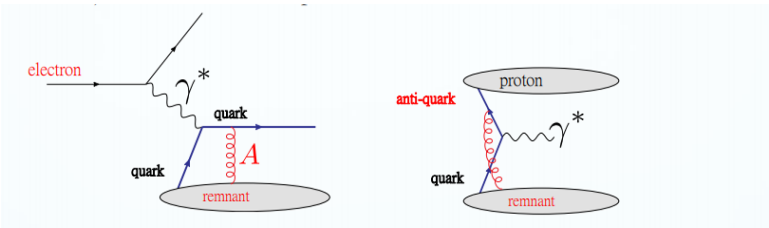

Figure 1.12: Illustration of different origin of the Sivers function in DIS (left) and Drell-Yan(right) process [28]

promising observables to disentangle them is the azimuthal angle dependence of hadron production within a jet. This process is associated with the Collins fragmentation function, which is one of the TMD fragmentation functions. It was first proposed by J.Collins [29], which described a transversely polarized quark fragmenting into a hadron. This azimuthal angle dependence property is usually referred to as the Collins asymmetry. Since the asymmetry correlates with the fragmentation function and the transversity distributions in the nucleon, it can disentangle the initial state effect caused by Sivers function and etc.

This process can be measured in multiple experiments, for example, in semi-inclusive deep inelastic scattering (SIDIS) and in proton-proton collision. For SIDIS, multiple collaborations, including the HERMES Collaboration [30], the COMPASS Collaboration [31], and the JLab HALL A experiment [32] reported non-zero Collins asymmetries for charged pions. For proton-proton collision, the STAR Collaboration also reported non-zero result[33] for charged pion in mid-rapidity, see Figure(1.13).

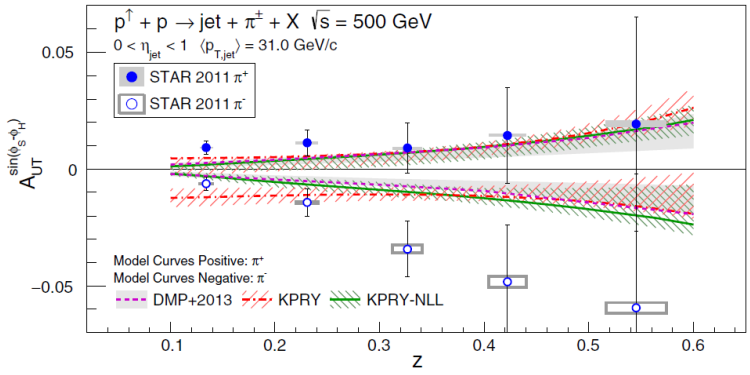

Figure 1.13: Collins asymmetries measured in STAR from 500 GeV proton-proton collision in mid-rapidity.[33]

Figure(1.14) illustrates the definition of the Collins angle $\phi_C = \phi_S - \phi_H$ in

proton-proton collision, in which ϕ_S is the angle between the proton spin and the production plane, and ϕ_H is the angle between hadron momentum projection on the plane perpendicular to the jet thrust axis and the production plane. Note that the angle definition could be slightly different for SIDIS, where the Collins angle is written as $\phi_C = \phi_S + \phi_H$, see Figure(1.15). But the physical meaning of ϕ_C is consistent. ϕ_C is the azimuthal angle between the spin of the fragmented parton and the final-state hadron's azimuthal angle with respect to the direction of the jet axis. The asymmetry is the cross-section modulation of ϕ_C angle in any process.

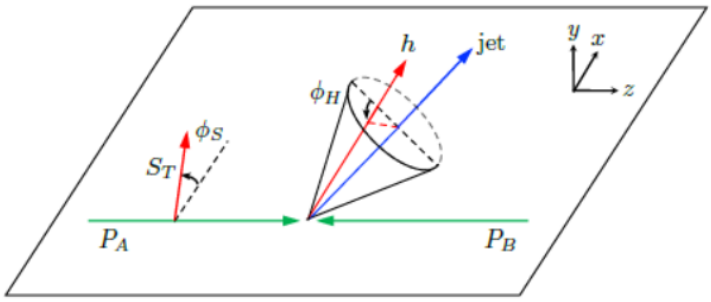

Figure 1.14: Illustration of the kinematics for the azimuthal distribution of hadrons inside a jet in proton-proton collision.

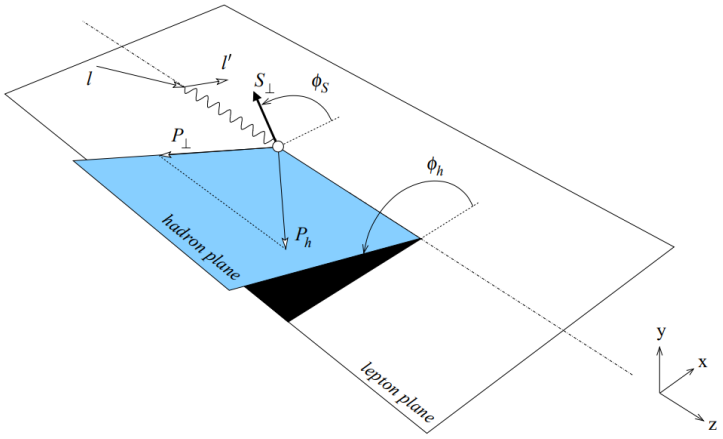

Figure 1.15: Illustration of the kinematics for the azimuthal distribution of hadrons production in SIDIS.

Regarding the Collins Fragmentation Function, a topic is of particular interest. It is the universality of the Collins Fragmentation Function. There is an

argument [34] that the Collins Fragmentation Function is the same for multiple processes of proton-proton collision, SIDIS, and electron-positron annihilation. Therefore the fragmentation function obtained in one experiment can be used to calculate the Collins asymmetry in the other, as shown in reference [34][35][36]. Currently the Collins Fragmentation Function was extracted from the SIDIS and electron-positron annihilation experiment which is used as input in calculation for proton-proton collision. The comparison of the prediction of such calculations with the experimental data from RHIC will provide an important test of the universality of the Collins fragmentation function.

In this thesis, we are probing the Collins asymmetry for π^0 in an electromagnetic jet using the process of $p^{\uparrow}+p \rightarrow EM-jet+\pi^0+X$, at large pseudo-rapidity at STAR.

1.3.5 Twist-3 Collinear Factorization

The Twist-three collinear factorization is another approach to explain the large TSSA. It was first developed by Qiu and Sterman for pion production in proton-proton collisions [37], and then applied to various other processes. The collinear twist-3 factorization framework is a natural extension of the original leading twist collinear factorization. Compared to the TMD factorization, the collinear twist-3 factorization only requires one "hard scale", usually a large momentum transfer. For example, inclusive hadron productions at high-pT in proton-proton collisions and in SIDIS. So the measurements performed in this thesis should fall into the allowed region of this factorization scheme.

The traditional parton model is introduced in momentum space. The infinite momentum frame is good in simplifying related calculation. In order to handle the complexities introduced by spin dependence and the sub-dominant effects associated with transverse spin, it is useful to perform the analysis in the coordinate space, which can exploit the formal methods of the operator product expansion(OPE). The OPE is a technique to expand the product of two local operators at a short distance in a series of non-singular local operators multiplying c-number singular functions, like Equation(1.10). The twist is a concept of the dimension analysis in the OPE. The detail of twist definition and twist analysis can be found in this reference[38].

$$\hat{A}(\xi)\hat{B}(0) \sim \sum_{[\alpha]} C_{[\alpha]}(\xi)\hat{\theta}_{[\alpha]}(0) \quad \text{as} \quad \xi^{\mu} \to 0 \tag{1.10}$$

In DIS, the definition of the hadronic tensor, which relates to the parton PDF, can be written as current operator products in Equation(1.11). The twist analysis shows that the complete specification of the light-cone quark correlation function requires nine distribution functions: three twist-2 (denote as f1, g1, h1), three twist-3 (denote as e, g2, h2), and three twist-4 (denote as f4, g3, h3). At each twist there is one spin-average distribution (f1, e, f4), one chiral-even spin distribution (g1, g2, g3), and one chiral-odd spin-dependent distribution (h1, h2, h3)[39].

$$4\pi W_{\mu\nu} = \int d^4\xi e^{iq\cdot\xi} \left\langle P,S \left| [J_{\mu}(\xi), J_{\nu}(0)] \right| P,S \right\rangle \tag{1.11}$$

Non-vanishing contributions to cross section is related to the collinear twist-3 parton distributions (correlation functions) $f_{a/A(3)}, f_{b/B(3)}$ and collinear twist-3 fragmentation function $D_{C/c(3)}$. Particle "A"("B") is presumed to be polarized(unpolarized) in the context. The three "H" are the hard scattering subprocesses. Note that the last term represent the chiral-odd twist-3 fragmentation function coupling with the chiral-odd twist-2 transversity distributions.

$$\begin{aligned} d\sigma\left(\vec{S}_{\perp}\right) =& H \otimes f_{a/A(3)} \otimes f_{b/B(2)} \otimes D_{C/c(2)} \\ &+ H' \otimes f_{a/A(2)} \otimes f_{b/B(3)} \otimes D_{C/c(2)} \\ &+ H'' \otimes f_{a/A(2)} \otimes f_{b/B(2)} \otimes D_{C/c(3)} \end{aligned} \tag{1.12}$$

The first term in Equation(1.12) is widely research, in which the Efremov-Teryaev-Qui-Sterman(ETQS) function[37] was proposed as a candidate for the origin of the large TSSA. It resembles the Sivers function in the TMD factorization, which comes from the initial effect. It had been proven that the ETQS function is related to the Sivers function in SIDIS in the way of Equation(1.13), where q is the quark flavor, and M is the nucleon mass[40]. Given this relation, a measurement constraining the ETQS function also constrains the Sivers function and vice versa. However, the ETQS function extracted from the proton-proton collision and the Sivers function extracted from the SIDIS does not coincide well[41]. The second term in Equation(1.12) in which the unpolarized proton contains the collinear twist-3 functions, is considered to be small. In recent years, people started to focus on the third term in which the collinear twist-3 fragmentation function and

transversity function are extracted from SIDIS and electron-positron annihilation experiments, alone can generate large TSSA[41].

$$T_F^q(x,x) = -\int d^2\vec{p}_\perp \frac{\vec{p}_\perp^{\,2}}{M} f_{1T}^{\perp q}\left(x, \vec{p}_\perp^{\,2}\right)\Big|_{\text{SIDIS}} \tag{1.13}$$

However, these terms in collinear twist-3 factorization entangled in the TSSAs of π^0 so that one single measurement is far from getting a clear picture for the origin of the large TSSA. Other measurements like TSSAs of the direct photon and of W boson and etc. can provide crucial information about a lot of questions raised by the collinear twist-3 factorization and the TMD factorization.

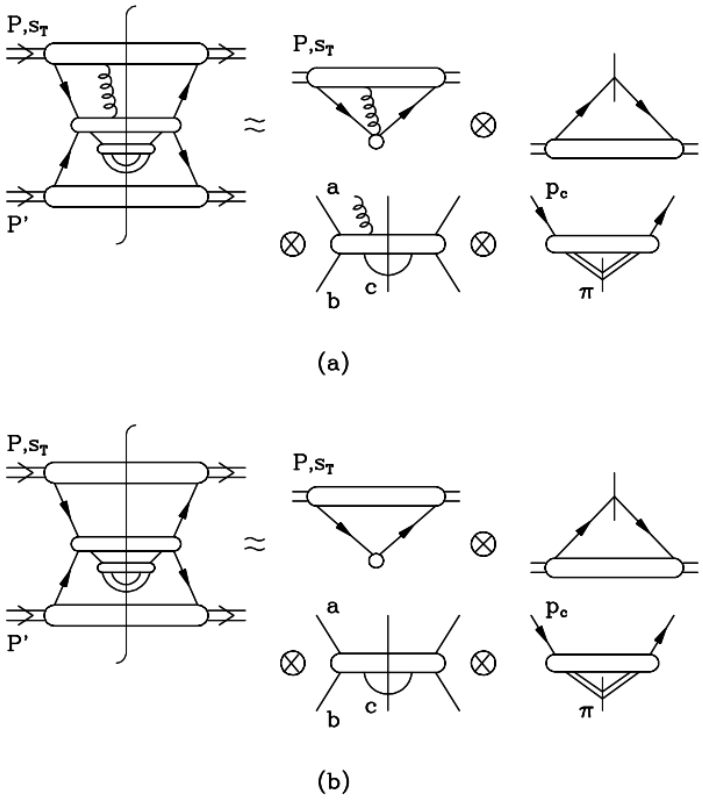

Figure 1.16: General cross section decomposition of scattering amplitude of hadronic pion production in polarized proton-proton collision. (a) with chiral-even three-parton matrix elements, (b) with chiral-odd transversity [37].

1.4 Structure of this Thesis

The remaining chapters of this thesis are arranged as follows: Chapter two describes the experimental facilities of RHIC, the Forward Meson Spectrometer

(FMS) detector at STAR, which is used in the measurements of TSSA for inclusive π^0 and the Collins asymmetry of π^0 inside an electromagnetic jet; Chapter three explained how these measurements are made from the basic step of the cluster reconstruction in the FMS to the extraction of the π^0 signal asymmetry. It also describes several improvements made to increase the precision of these measurements; Chapter four shows the final results as well as the calculation of their systematic uncertainty; Chapter Five provides a summary and outlook.

Chapter 2 Experimental Setup

This chapter is dedicated to the general description of the experimental apparatus. It includes a brief introduction of Relativistic Heavy Ion Collider(RHIC) in Brookhaven National Laboratory(BNL) and the STAR detector that installed in the RHIC ring. The sub-detector of the Forward Meson Spectrometer(FMS) and the polarimetry which is related to this thesis would be outlined in detail.

2.1 Relativistic Heavy Ion Collider

The Relativistic Heavy Ion Collider is a high energy physics experiment facility. It locates at Brookhaven National Laboratory in Long Island, New York State. It was and still is one of the key experiments in high energy physics. It was officially brought up in the long-range plan for nuclear science in 1983, finished its construction in 1999, and began its first physics run in 2000[42].

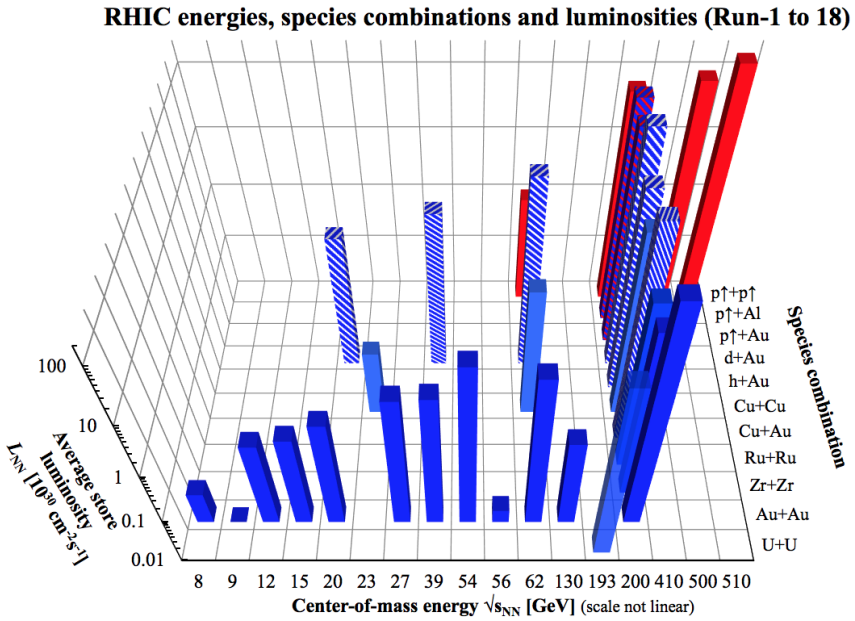

Figure 2.1: RHIC energies, species combination and luminosity from Run1 to Run18.[43]

RHIC is by design able to produce high energy and high luminosity beams of different species including proton and heavy ion. Figure(2.1) shows the RHIC energies, species combination in collision and luminosity from Run1 in fiscal year

2000 to Run18 in fiscal year 2017. Figure(2.2) shows the luminosity evolution of RHIC over the years in comparison with other hadron colliders in the world . For the gold beam, the specifications of the beam energy by design can be as high as 100 GeV, while the design luminosity is $2 * 10^{26} cm^{-2} s-1$. For the proton beam, the design specifications of the beam energy can be as high as 250 GeV, while the design luminosity is $1.4 * 10^{31} cm^{-2} s-1$[42]. That makes it the most powerful heavy ion collision machine back in the days until the Large Hadron Collider built in 2010 at CERN. These extreme conditions allow the experiment to mimic the conditions of the early universe and to create the quark gluon plasma, a new state of matter which is the hottest matter ever created in a laboratory, measuring some 4 trillion degrees Celsius, or 250,000 times hotter than the center of the Sun[44]. The cutting edge technology of the RHIC facility is the cornerstone of the fruitful scientific discoveries in heavy ion filed over the years. Other than that, RHIC is also the only facility that can provide the high luminosity polarized proton beam at relativistic energies in the world, which makes it a unique opportunity for spin physics. The RHIC spin group is an active workgroup dedicated to multiple topics in nuclear spin physics. The work of this thesis is part of the RHIC spin program.

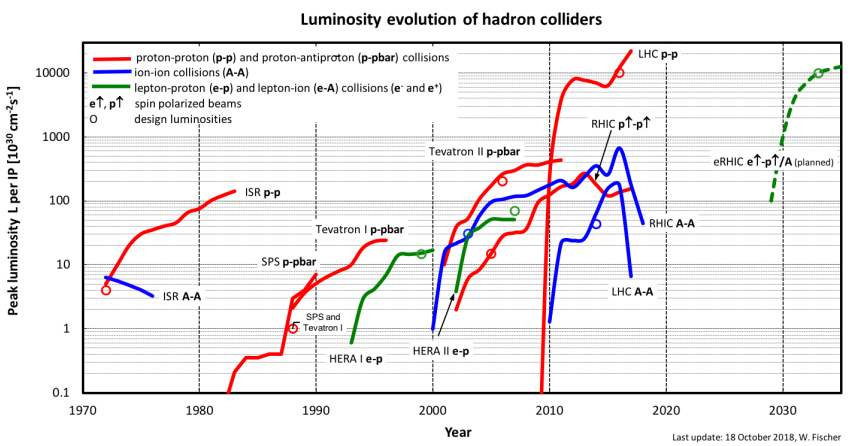

Figure 2.2: RHIC luminosity evolution over the years in comparison with other hadron colliders in the world.[43]

Figure(2.3) shows the layout of the key components in RHIC facility featuring the essential ones for the spin physics program. Full detail of the detectors can be found in the [45]. Proton beam is used in spin physics and it is the only beam that can be polarized in RHIC. Here presents the brief process of the production of the polarized proton beam. At fitst, the hydrogen anion beam is generated by

electron cyclotron resonance proton source in the optically pumped polarized ion source (OPPIS), which was specifically developed for the RHIC polarization program. The Hydrogen anion beam gets polarized by spin-transfer collisions with Rb vapors. The Polarized hydrogen anion beam is produced at 35 keV beam energy at about 80% polarization. By narrowing the pulse in time, OPPIS can produce 0.5 mA current in a 300 ms pulse in order to meet the designed luminosity[46]. The beam is accelerated to 200 MeV by radio frequency quadrupole(RFQ) and the linear accelerator(Linac). Then it is ready for the strip-injection to the booster. The Hydrogen anion pulse is captured in a single booster bunch with its electrons stripped off. The single bunch is accelerated in the booster to 1.5 GeV and then transferred to the Alternating Gradient Synchrotron (AGS), and then accelerated to 25 GeV. These accelerators have already existed for decades for the previous generation of high energy physics experiment before RHIC. The AGS was built in the 1960s and was well known for pioneer works done there that won three Nobel prizes. The design of alternating gradient focusing, in which the magnets filed changes direction constantly, allows particle beam to maintain focus in the Synchrotron, increasing limitation of beam intensity[47].

After the AGS, the polarized proton beam is injected into RHIC ring, where it is accelerated to higher energies. RHIC consists of two 3.8km circumference long quasi-circular concentric rings, one (“Blue Ring”) for clockwise and the other (“Yellow Ring”) for counter-clockwise beams movement. There are six interaction points for the two beams to collide head on where the two rings are oriented and intersect with one another. The detectors are located at one of these interaction points. There were five detectors once in the RHIC ring, two major ones: STAR(Solenoidal Tracker at RHIC) at 6 o’clock of the ring and PHENIX(Pioneering High Energy Nuclear Interaction eXperiment) at 8 o’clock, three small scale ones: PP2PP at 2 o’clock, PHOBOS at 10 o’clock and BRAHMS(Broad Range Hadron Magnetic Spectrometers Experiment at RHIC) at 2 o’clock. The three small experiments have been decommissioned. PHENIX has stopped running for an upgrade since 2016. So STAR is currently(2019) the only active experiment in RHIC.

The key of the RHIC spin program is the polarized proton beam. When the beam travels in the ring of a circular accelerator with a guiding magnetic field, its spin evolves with time. Such effect is governed by the Thomas-BMT equation [48], see Equation(2.1). The polarization vector $\vec{P}$ is expressed in the proton

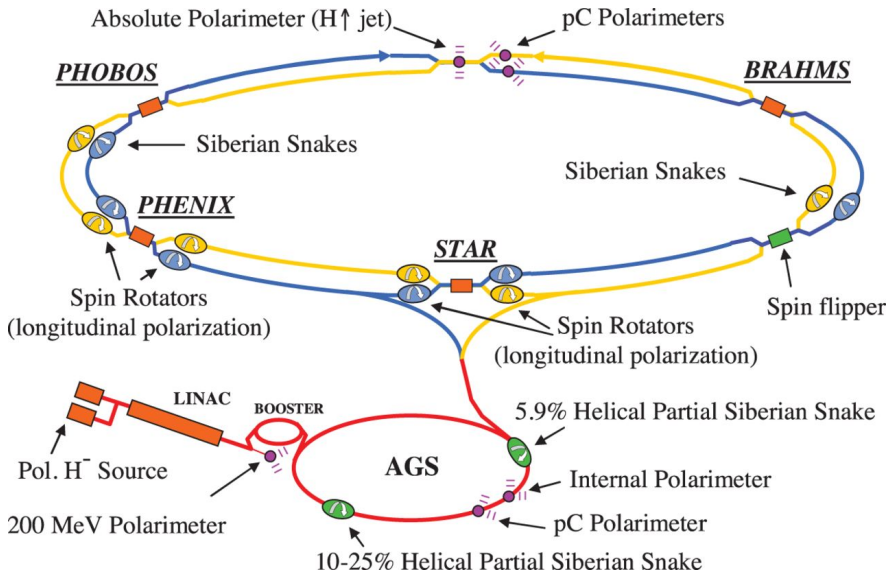

Figure 2.3: Accelerator configuration of RHIC facility for the spin physics program.[42]

moving frame. G equals to 1.793 being the anomalous magnetic moment of the proton. B is the magnetic field. e is the change, m is the mass and $\gamma = E/m$. Comparing to the motion equation function of a charged in a magnetic field, see Equation(2.2), it is easy to see that for a general magnetic field, the spin rotates along the axis of $\vec{B}\times\vec{P}$ and is $G*\gamma$ times faster than the orbital motion. Therefore, the existence of disturbance could induce the spin precession of the protons. The major source of the disturbance comes from two part, the intrinsic existence of focusing magnetic field and localized imperfections magnetic field. Usually, these disturbances could be random or so small that it hardly does too much harm to the beam polarization. However, they could be enhanced in some cases. For example, in any real accelerating machine, there is always some imperfections such as slightly misaligned magnet, creating some sort of disturbance periodically somewhere in the ring causing the polarization direction to move a little bit as the equation above predicts. During the acceleration, as the proton energy increases, the precession frequency also increases. When it reaches to integer times of the disturbance frequency, the disturbance is magnified by the resonance. This is called depolarizing resonance. For the kinematic of RHIC, every 523 MeV energy increase, this resonance takes place[45]. This makes extremely hard to maintain the high polarization for the high energy proton beam.

$$\frac{d\vec{P}}{dt} = -\left(\frac{e}{\gamma m}\right)\left[G\gamma\vec{B}_{\perp} + (1+G)\vec{B}_{\parallel}\right]\times\vec{P} \tag{2.1}$$

$$\frac{d\vec{v}}{dt} = -\left(\frac{e}{\gamma m}\right)\left[\vec{B}_{\perp}\right] \times \vec{v} \tag{2.2}$$

To compensate this, a novel system called "Siberian Snake" which was first invented by Derbenev and Kondratenko from the Institute of Nuclear Physics, Novosibirsk[49] was installed in RHIC. This new device is composed of four groups of helical dipoles. For each ring, two groups are installed at the opposite side of the ring. A group of helical dipoles is used to force the spin to rotate 180° along a fixed axis. By manipulating this set of rotation axis, the Siberian Snake would change the phase of the precession of the spin by 180° after a whole revolution. For non-depolarization resonance, the effect of the newly added device is trivial. But in the case when depolarization resonance happens, it will force the polarization to correct itself for two full revolutions in the ring. An example in Figure(2.4) would show how this operation is able to fight the depolarization resonance. The left part of the figure shows the spin precession in a cone, and a disturbance magnetic field is making it depolarized. After a full revolution, passing through two groups of helical dipoles, the new polarization direction is pointing now as the right part of the figure shows. Under the transition of the phase of the precession, the same disturbance magnetic field is going to pull the polarization back to its place in the next revolution. In this way, the "Siberian Snake" allows RHIC to store about 50% polarization proton beam for more than 10 hours.

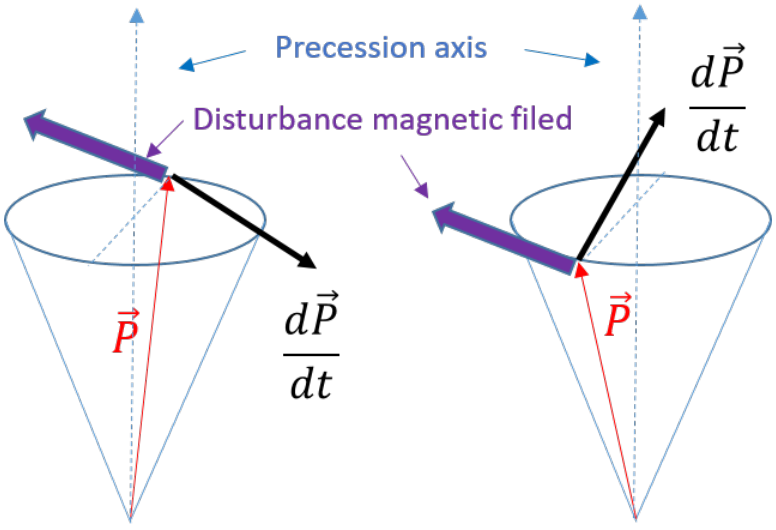

Figure 2.4: A example showing how the "Siberian Snake" compensate the depolarization resonance by rotating the spin direction, details in the text.

The proton beams are transversely polarized in the store ring. There are two sets of spin rotator installed near at the two major interaction points at STAR and PHENIX. These rotators are composed of helical dipoles. They are set to rotate the proton spin by 90° to the longitudinal direction. That allows RHIC to collide longitudinally polarized protons. After the interaction point, the other rotator will recover the spin to the transverse direction so the beam remains in transverse polarization in the store ring.

2.2 STAR Detector

The Solenoidal Tracker At RHIC (STAR) is one of the two major detector systems at RHIC featuring its large coverage and powerful tracking ability. It serves multiple physics goals, from investigating the quark gluon plasma to probing the nuclear spin structure. The configuration of STAR varies year from year. Sub-detectors could be added or removed due to the operation plan. Run-11 and Run-15 are two datasets analyzed in this thesis. The biggest difference of the detector configuration between the two years is the installation of HFT in Run-15. Figure(2.5) shows a general layout of the major part of the detector system, which is not specified for one year. Some of the key sub-detectors are labeled. The major sub-detector used in the analysis of this thesis is the Forward Meson Spectrometer(FMS), which is highlighted in the figure. Other relevant detector includes the TPC and BBC. Below is a brief description of some of them.

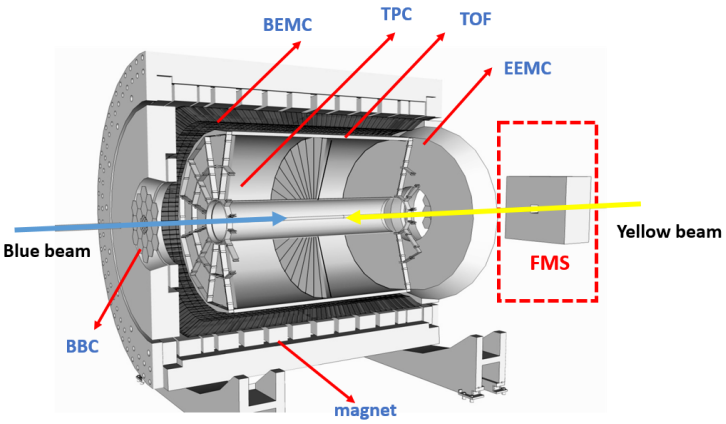

Figure 2.5: Layout of the STAR detector system, labeling some of the key sub-detector and highlighting the Forward Meson Spectrometer in a red square.

- TPC - Time Projection Chamber[50]. Figure(2.6) shows the layout of the

TPC. It is one of the main detectors in STAR. It is 4.2 m long and 4 m in diameter, covering large pseudo-rapidity range from -1.8 to 1.8. When charged particles are moving in the TPC, they ionized the P10 gas, which is made of 10% methane, 90% argon. The ionized electrons are drifted by the electric field and collected by the Multi-Wire Proportional Chambers with 136,608 readout pads at the two sides of the detector. The TPC provides good tracking measurement for charged particles with momentum range from 100 MeV/c to 30 GeV/c. With the tracks information, it can reconstruct the vertices of the events. It is also capable of particle identification of tracks whose momentum ranges from 100 MeV/c to greater than 1 GeV/c by using the ionization energy loss method.

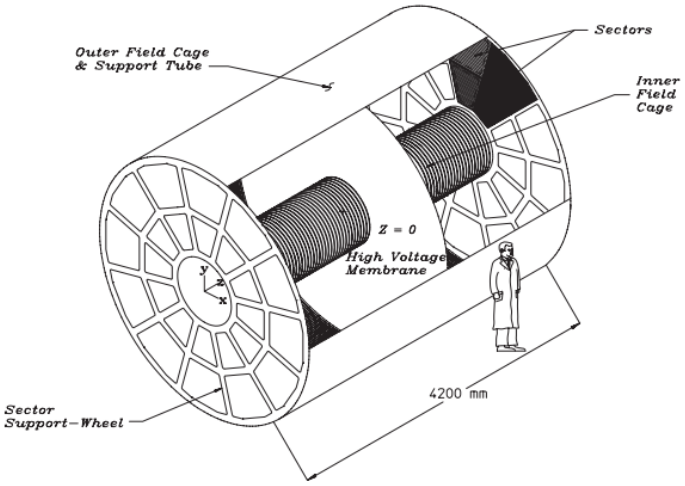

Figure 2.6: Layout of the STAR Time Projection Chamber[50].

[50]

• BEMC - Barrel Electromagnetic Calorimeter[51]. Figure(2.7) shows the layout of the BEMC and one of its tower module. The BEMC locates outside the TPC, covering a pseudo-rapidity range from -1 to 1. The BEMC has 4800 towers, each of them subtending 0.05 in $\Delta\eta$ by 0.05 in $\Delta\phi$, is divided into 120 tower modules. The BEMC is a sampling calorimeter, in radial direction, it consists of a lead scintillator stack of 20 layers of 5 mm thick lead, 19 layers of 5 mm thick scintillator and 2 layers of 6 mm thick scintillator. When an electron or photon is passing through the BEMC, it will develop an electromagnetic shower and leave pretty much of all the energy in the detector since the BEMC has a total depth of approximately 20 radiation length. The excited light produced by the incident electron or photon would be collected by the Photo-Multiplier

Tubes(PMT). The energy and the position can be reconstructed based on that.

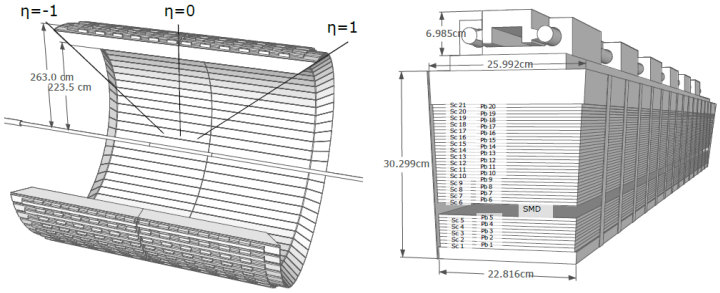

Figure 2.7: Layout of the STAR Barrel Electromagnetic Calorimeter and one of its module[51].

• BBC - The Beam-Beam Counter. Figure(2.8) shows the layout of the BBC. The BBC consist of two sets of scintillator annuli installed around the RHIC beam pipe on the EAST and WEST side of the STAR detector, just outside of the TPC. Both annuli are 3.75 meters from the center of the TPC. Each of them has 16 packed hexagonal scintillators which are divided into two rings: six tiles for the inner ring and 12 tiles for the outer ring, covering a pseudorapidity range from 3.4 to 5.0. These scintillators are only 1 cm thick, designed to pick up signals from minimal ionized particles. It can be used as a local polarimeter as well as a minimum-bias trigger system.

• FMS -Forward Meson Spectrometer. The FMS is the main sub-detector

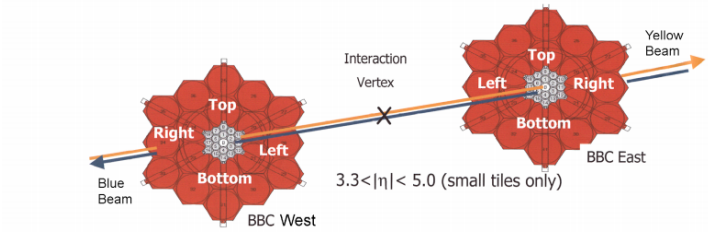

Figure 2.8: Layout of the STAR The Beam-Beam Counter[52].

used in this analysis. It is an electromagnetic calorimeter placed at forward pseudorapidity at the west side of the STAR. It will be introduced in detail in the next section.

2.3 Forward Meson Spectrometer

The Forward Meson Spectrometer, is an electromagnetic calorimeter built for finding the mesons by their decay photons at the forward pseudorapidity. It allows probing the physical process at different kinematics that other sub-detectors cannot. The FMS is made of 1264 led glass towers of two specifications. The outer one is called the large cell, which is 5.8 cm x 5.8 cm in size, covering a pseudorapidity range from 2.5 to 3.1. The inner one which provides better granularity for photon separation is called the small cell, which is 3.87 cm x 3.82 cm, covering a pseudorapidity range from 3.1 to 4.1. The small cell is a little bit off a square shape. But it is separated by spacers of 0.05 cm thickness, which makes it a square shape together with the spacers. The specifications for both cell types are listed in Table(2.1).

Table 2.1: FMS cell specification

Cell Type	Radiation Length	Width	Length	Numbers
Small cell	2.50 cm	3.87 cm	45.0 cm	476
Large cell	3.75 cm	5.81 cm	60.2 cm	788

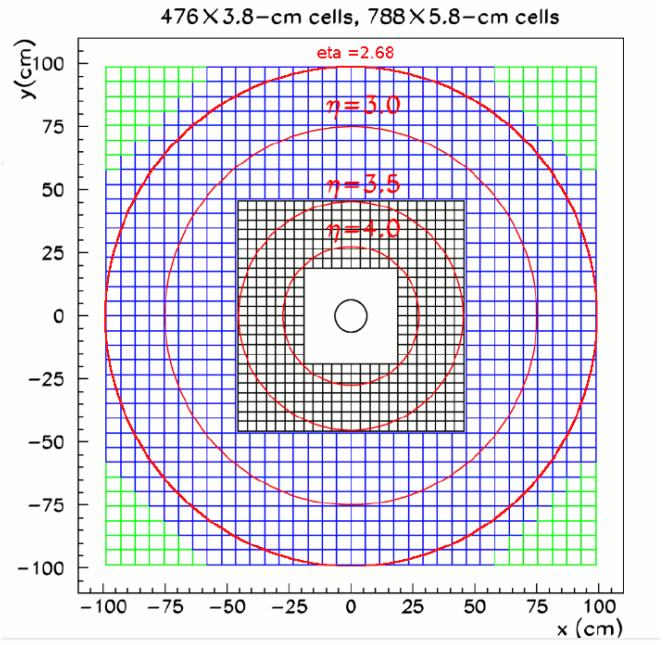

Figure 2.9: Layout of the STAR Forward Meson Spectrometer.

The FMS is a full absorption calorimeter, in which the lead glass acts as both absorber and means of detection. This differs from the BEMC due to the

different requirement of being compact. Like other electromagnetic calorimeter, the FMS can detect both the electrons and photons but unable to separate them without additional detectors. But since the photon yield is much higher, it could approximately consider all signals are from photons. When a high energy photon from the collision hits the FMS, it will interact with the material inside and loss energy mainly by pair production. The resulted electron and positron excite bremsstrahlung photons. If the energies of bremsstrahlung photons are high enough, they will create more electron-positron pairs. The Pb added to the glass act as the heavy nucleus which could increase the probability of the above process. Continuing this cycle will result in an electromagnetic shower[53]. The electromagnetic shower develops longitudinally and transversely. In the longitudinal direction, since both types of cell have a length of about 18 times of radiation length, the electromagnetic shower mostly deposit all the energy when traveling inside the FMS. In the transverse direction, the shower grows bigger and extend to adjacent towers as it travels deeper in the FMS. The width of the shower is limited by the Molière radius. Usually, an incident photon could fire from a few to more than ten towers. When the energies of the particles in the shower are lower than the critical energy E_c, the shower terminates. E_c is the critical point in which photon energy loss from bremsstrahlung equals to that from Compton scattering. It is given by approximation $E_c = \frac{800MeV}{Z+1.2}$. For the FMS, Z=82 for Pb, so the critical energy $E_c \simeq 10MeV$. From this point, the main process for photon interaction with the material switches from pair production to Compton scattering.

In a developing shower, when the secondary particles are moving faster than light in such material, the Cerenkov radiation takes places. The Cerenkov photons are moving towards the end of the FMS where they are collected by the PMTs. The advantage of using Cerenkov light over the scintillation light as the calorimeter signal is that the signal generation is much faster[54]. It allows shorter time from the production of a signal to the signal integration at the Front-End Electronics, which results in faster read-out speed. In order to isolate the Cerenkov photons produced from different cells, each cell is wrapped by a $10\mu m$ thick aluminized mylar. The photon-electron yield per unit energy deposition in the glass is estimated to be around 1000 photo-electrons/GeV for large cells and 700 photo-electrons/GeV for small cells[55]. After calibrating of the PMTs, the energy deposition inside a tower can be calculated by the number of the Cerenkov photons times the gain. However, due to the combined effects of Cerenkov pho-

ton absorption by the glass and loss at glass/mylar surface reflections during light propagation, and limited quantum efficiencies of PMT cathodes, the energy readout in the PMTs suffers from some non-linear effect. This means that, even a more precise calibration of the tower energy is done, the tower energy is only correct for the specific energy where the calibration is done. This problem will be discussed in detail in the next chapter.

The FMS trigger system is similar to the STAR trigger system. Both share many basic concepts, software, and hardware. The details of the STAR trigger system can be found in reference[56]. For the FMS triggers, the most detailed description can be found in reference[57].

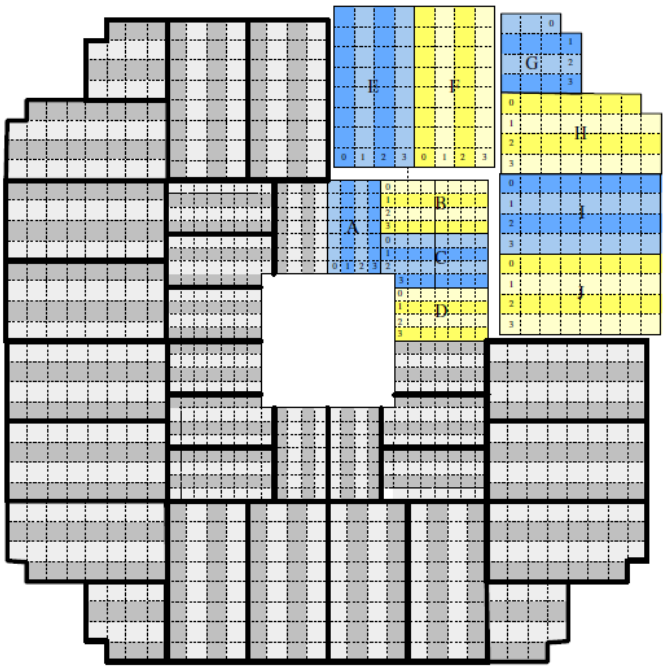

Figure 2.10: FMS Cell to QT and Layer-0-DSM Assignment Scheme.[58]

The FMS triggering is based on the information of the integration of the current that comes from the PMTs. The total charge is digitized to a 12-bit integer from 0 to 4,095, denoted as the number of ADC (Analog-to-Digital Conversion) counts. There are four so-called QT crates handling this task, associating to four quadrants of the FMS. These four quadrants are exactly the same and symmetric with respect to the center of the FMS, see Figure(2.10). In the figure, one quadrant is highlighted. The zones with labels from A to H associate 10 QT boards in the QT crate. For each labeled zone, it is divided into four strips with a number on each of the strip. Each strip is associated with one of four the QT8 cards in

one QT board. In such an arrangement, all tower in the FMS associates one QT8 card in the QT crate.

The Data Storage and Manipulation (DSM) boards are used in the STAR triggering system as a processing unit. It is used to judge whether an event meets certain criteria of a predefined trigger. It has a layer structure, in which the higher layer is for the complex thus time-consuming triggers. So the DSM takes information from the detector and decides whether the next move is to perform the next level DSM or discard the event or record the event.

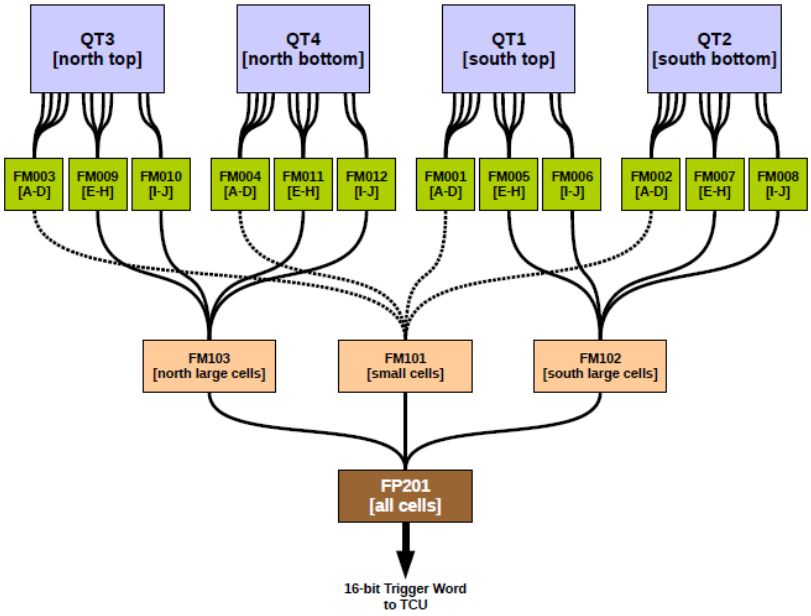

Figure 2.11: FMS DSM information flow and decision tree.[58]

The ten QT boards in a quadrant are separated into 3 groups, A-D,E-H,I-J. The information of each one group including the truncated ADC sum of each QT8 card($5 \times 4bits$) and the channel number of the highest tower of the group is sent to one layer-0 DSM board. It compares the high tower ADC to a threshold and sums up the ADC sums in various combinations of 4 adjacent QT8 stripes:

• A). sum over all QT8 cards of each QT board individually:

- sumA, sumB, sumC, sumD, sumE, sumF, sumG, sumH, sumI, sumJ

• B). sums split between adjacent QT boards (4 adjacent QT8 cards):

-sumBC = B2 + B3 + C0 + C1

-sumCD = C2 + C3 + D0 + D1

-sumEF = E2 + E3 + F0 + F1

-sumGH = G2 + G3 + H0 + H1

-sumIJ = I2 + I3 + J0 + J1

The combination of ADC sums and the high tower comparison results of all layer-0 DSM board are passed to the layer-1 DSM board in which the sums are compared to corresponding thresholds, forming the board sum triggers for the large and small cell. This board sum technique is essentially a fast but very crude way to emulate cluster finding. Again, sums and comparison results are sent to the layer-2 DSM board where more complex triggers like the FMS Jet Patch are formed. It sums up the ADC in a quadrant which is shown in Figure(2.3) and compares them to the corresponding thresholds. The final decision is made based on all the comparison results and sent to the Trigger Control Unit(TCU) to record/reject the event. The whole DSM information flow is shown as a tree structure in Figure(2.11)

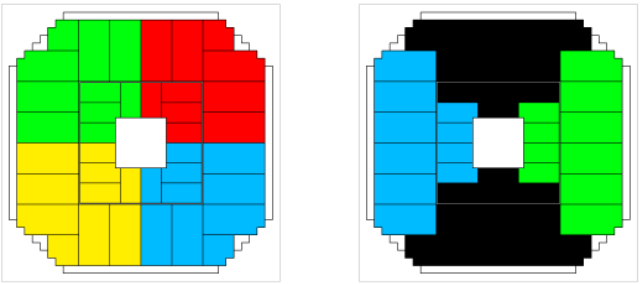

Figure 2.12: FMS quadrants for Jet Patch trigger .[58]

The FMS Board Sum triggers and FMS Jet Patch triggers are used in this analysis. An additional but non-physical trigger is the FMS LED trigger. The fiber optic cable for every PMT is connected with the LED flasher system, which flashes at 1Hz and triggers the FMS. These events are used in tracking time-dependence of the gain of the PMTs and radiation damage in the Pb-glass, which would be discussed in the calibration session. The LED trigger is independent of the physical ones above.

In Run13, the trigger rate was observed constantly decreasing during the run. It was because the Pb-glasses suffered from serious accumulated radiation damages. The ionizing radiation inside the glass caused the electrons to be stripped from the atom valence shell. Some of them ended up in an anionic vacancy or some types of crystallographic defect. it would cause additional photon absorption which darkened the glasses[59][60]. This effect is visible in appearance ,see

the left panel in Figure(2.13). It is worse in cells closer to the beam line because of the higher amount of radiation there. Refurbishment work was done before Run-15. The Pb-glass was unstacked and exposed to sunlight. The ultraviolet radiation of the sunlight was found to be able to reverse the radiation damage by exciting the misplaced electrons, pushing its way away from the crystallographic defect so that the glass became clear again. There are some researches on this photon-bleaching process,see references [61][62][63]. The right panel in Figure(2.13) shows the more transparent Pb-glass after the treatment. During Run 15, the higher luminosity was found to cause the Pb-glass to accumulate radiation damage more rapidly than before. Despite the heavy labor work of unstacking the FMS and exposing all cells to sunlight, the radiation damage will cause enough trouble for an ongoing run. As a solution, a UV-LEDs photo-bleaching system was built [57] for Run17, which can be operated during the beam dump time in RHIC. It could fully cure the glass within approximately 48 hours.

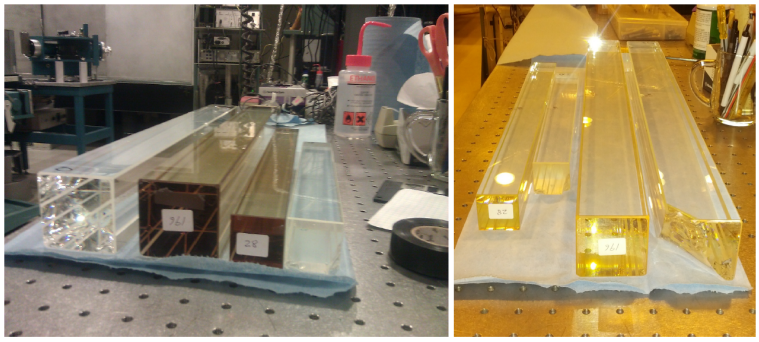

Figure 2.13: lead glasses before and after a 40-hour UV treatment.[58]

Besides of the radiation damage, the PMT bases were problematic in Run-11, which caused the gain jumping all the time. This effect will be discussed in the calibration section. In addition to curing the radiation damages, before Run-15, the PMT bases of all the large cells had been replaced, a few hundred of the small cell as well. So, Run-15 and later runs are totally free of this problem.

2.4 Polarimetry

The measurement of the proton polarization is crucial to any asymmetry analysis because the raw asymmetry is scaled by the polarization. In the 12 o'clock of the RHIC ring liesthe two polarimeters: the hydrogen gas jet (H-jet) and the proton-carbon (pC) polarimeters. The detail of the polarimetry at

RHIC can be found in these references[64] [65]. There is a well-known effect of nuclear scattering in the Coulomb-Nuclear Interference(CNI) region, in which the nucleon scattering or particle production cross section differs in the left-right direction with respect to the proton beam. The asymmetries associate with the proton polarization. In general, vertical beam polarization can be determined by measuring the left-right asymmetry, using a known reaction like proton-proton or proton-Carbon, with an analyzing power Ap, see Equation(2.3). The analyzing power is significant and largely independent of energy for energy above a few GeV, which makes it an ideal tool to measure the polarization. Both of the results of the polarimetry are provided by the RHIC spin group.

$$P_B = \frac{1}{A_p}\frac{N_L - N_R}{N_L + N_R} \tag{2.3}$$

Two identical pC-polarimeters are installed in the yellow and blue rings. It measures relative polarization to a few percents statistical accuracy by observing the asymmetry of the Carbon nucleus scattered off from a carbon ribbon target (2.5 cm length with 10-20 $\mu g/cm^2$ thick and 4-10 μm width). Six silicon strip sensors are placed around to pick up the signals from the scattering. Figure(2.4) shows the layout of pC polarimeter. This measurement is usually done within a minute, providing the required statistics, so that it could be done multiple times during data taking. The targets are normally kept away from the beam line and rotated into the beam when the polarization measurement is executed, which is usually done at the beginning of a fill and every a few hours in between. These measurements keep tracks of the beam polarization during the run which reduces the systematic uncertainty for any polarization related analysis.

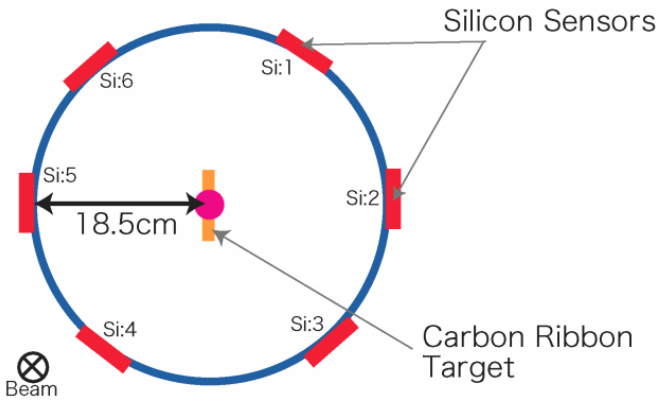

Figure 2.14: The RHIC pC-polarimeter layout.[64]

The H-jet polarimeter uses a longitudinally polarized hydrogen atomic beam as a target, which crosses the RHIC beam in the vertical direction, see Figure(2.4). In that case, the hydrogen atomic beam polarization direction will be either aligned or anti-aligned with the proton beam polarization. Similar to the pC polarimeters, the H-jet polarimeter takes advantage of the CNI region of proton-proton elastic scattering, which the recoiled proton has a left-right asymmetry distribution. There is also an array of silicon strips to pick up the signals from the recoiled protons. The H-jet polarimeter, compared to the pC polarimeter is much slower. It could need data for a couple of days to get enough statistics. So it is used to provide an absolute polarization measurement which is used to calibrate the pC polarimeter measurement.

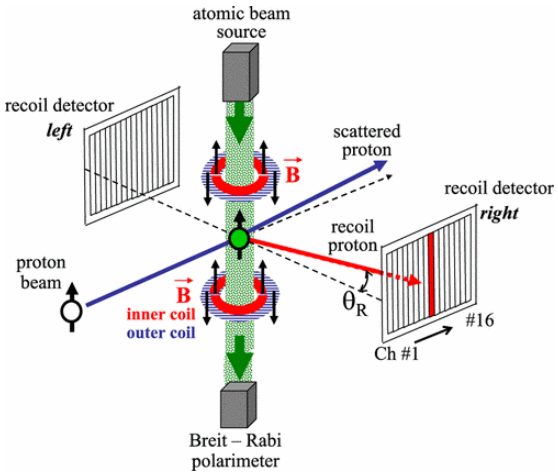

Figure 2.15: The RHIC H-jet polarimeter layout.[66]

Chapter 3 Data Analysis

This chapter describes the data analysis of transverse single spin asymmetry A_N of π^0 and electromagnetic jet and Collins asymmetry A_{UT} of π^0 in an electromagnetic jet. It includes several sections of data selection, data quality assurance, FMS calibration, photon/pion reconstruction, improvement of the photon reconstruction algorithm, jet reconstruction, calculation of the asymmetry and simulation. Although there are two analyses in this thesis, a large portion of them are quite the same such as data quality assurance, calibration, and the photon/pion reconstruction, asymmetry calculation and so on. In the following sections, the discussion will be performed at the same time. Both analyses are done using STAR data in Run-11 and Run-15. The data in these two run periods are different in collision energy and detector status. However, the infrastructure of the analysis for the two different years of data is just the same. The parameters and results could be different though, see details in the following sections.

3.1 Dataset

The basic unit in data taking in STAR is a run. A run is usually shorter than half an hour. It is also the basic unit of the data QA. The following script generates all the run numbers that fit the conditions which are set in the script. These conditions specify the trigger setup name, file name, production ID and file type.

get_file_list.pl -keys runnumber -cond filename st_fms,
trgsetupname=pp500_production_2011,production=P11id,
filetype=daq_reco_MuDst,storage! HPSS -limit 0

get_file_list.pl -keys runnumber -cond filename st_fms,
trgsetupname=production_pp200trans_2015||production_fms_pp200trans_2015,
production=P15ik, filetype=daq_reco_MuDst,storage! HPSS -limit 0

After that, there are a few runs kicked out of the list due to various of reasons, including too short runtime, missing spin information, abnormal hit energy

and abnormal trigger rate. For Run-11, 341 runs from day 79 to day 98 are selected. For Run-15, 711 runs from day 66 to day 93 are selected.

Table 3.1: Summary of dataset that used in the analysis Run-11 and Run-15

Year	Fills	Runs	Energy
Run-11	29	341	500 GeV
Run-15	37	711	200 GeV

In the selected dataset, only the data from the FMS is used to reconstruct the π^0 in the analysis. So it relies on the FMS triggers to provide the high event rate. Table(3.2) list all the triggers used in the analysis.

Table 3.2: Triggers and trigger ID in Run-11 and Run-15

Run-11 Trigger	Run-11 Trigger ID	Run-15 Trigger	Run-15 Trigger ID
		FMSJP0	480830
FMSJP1	320220	FMSJP1	480809/480829
FMSJP2	320231	FMSJP2	480808/480828
		FMSLgBS0	480804/480824/480844
FMSLgBS1	320226	FMSLgBS1	480805/480825
FMSLgBS2	320227	FMSLgBS2	480806/480826
		FMSSmBS0	480801/480821/480841
FMSSmBS1	320222	FMSSmBS1	480802/480822
FMSSmBS2	320223	FMSSmBS2	480803/480823/480843

3.2 Quality assurance

Data quality assurance (QA) is the first step before any further physics analysis. It assures the physics conclusions are not compromised by the corrupted data. It includes online and offline examination of the data. The online QA is the real time data quality monitoring. During the data taking, on site shift crew are responsible for operating the detectors, setting up the data taking configuration, and monitoring any abnormalities and fixing any problem if they can. There could be problems like malfunctioned detectors, abnormal beam status, unstable

trigger rate, problematic electronics and etc., which render the data useless in the dataset. The Shift crew monitors the indicators like trigger rate and online data QA plots and keep a log about the problems and operations, in which some of the data would be marked as good/bad or questionable.

Offline data QA examines in details the operation status of the detectors which cannot be done in online data QA due to the limit of online processing. It could find the outliers of the key parameter of the detector and eventually give a list of the good runs that can be used in the physics analysis.

1.) The first item to check is the short running time. If the running time of a run is too short(less than 3 minutes), there is not enough information to judge if it is good or not. It had better be removed from the analysis.

2.) The second item to check is the trigger rate which indicates the condition of the FMS. A sudden change, usually a boost of the trigger rate of a certain trigger suggests abnormal occupancy which may be caused by hot towers. Figure(3.1) shows the trigger rate of FMSJP1 over the run time. The rate has been normalized by the mean over the run time. The vertical lines are marker which records any operation or status change of the detector, such as the high voltage change. The outliers are defined as three sigma away from the mean and should be excluded from the run list. The trigger monitor tool was developed in 2012, so there was no such check for Run-11 data.

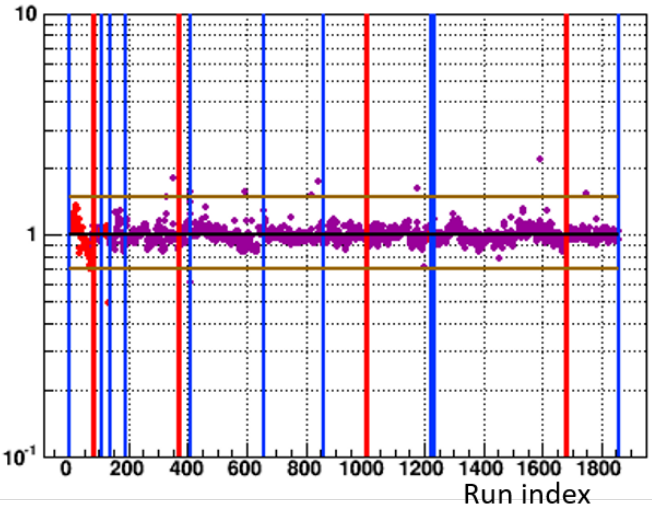

Figure 3.1: Example for checking FMSJP1 trigger rate over the runs in Run-15. The rate has been normalized by the mean over the run time[67].

3.) The third item to check the data quality is to look at the energy distribution of the reconstructed object. Figure(3.2) shows the FMS point energy which is normalized by the number of triggers over the runs. A stripe on the left indicates something unusual in that run which will be excluded in the run list.

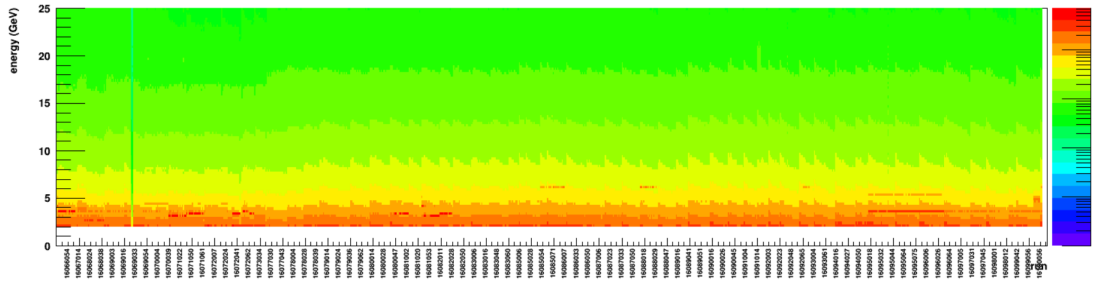

Figure 3.2: Example for checking FMS point energy over the runs in Run-15[68].

4.) The fourth item is to find out the bad channels. Bad channels include hot and problematic ones. A hot channel refers to the one with too many hits comparing to the average hits of the whole detector within a certain range of time. It could be something wrong with the tower itself, or the photo magnifier tube, or the electronics, or an inappropriate gain being applied. These hot channels could corrupt the calibration and the analysis since their hits are not physical. It also distorts the detector acceptance and reports incorrect energy scales. In order to find out the hot towers, one needs to compare the hit number of each channel. In practice, one could sum up the hit number of each channel and normalize it with the event number in a run. Besides the hot channels, there are other problematic channels whose hardware structure may be damaged. Since these channels only reveal themselves in the calibration iteration, they will be discussed in the next section. Altogether a list of bad channels can be made. To Mask them out, one just simply sets their gain to zero. Figure(3.3) and Figure(3.4) show these two types of bad channels in shade in the FMS for Run-11 and Run-15.

5.) The fifth item to check is the bit shift of the FMS channel. It refers to the binary bit which is used to store the ADC value not starting from the normal lowest bit. It has been discussed in the last chapter how the PMTs of the FMS pick up the induced photons and magnify them when there is a hit in the FMS. The photon yield which is linear to the energy deposited in the FMS tower is recorded by the electronics and stored in a 12-bit binary digit as the ADC value. For example, 000000001111 refers to ADC 15. However, during data taking, bit definition could be changed due to some practical reason. For example, when the

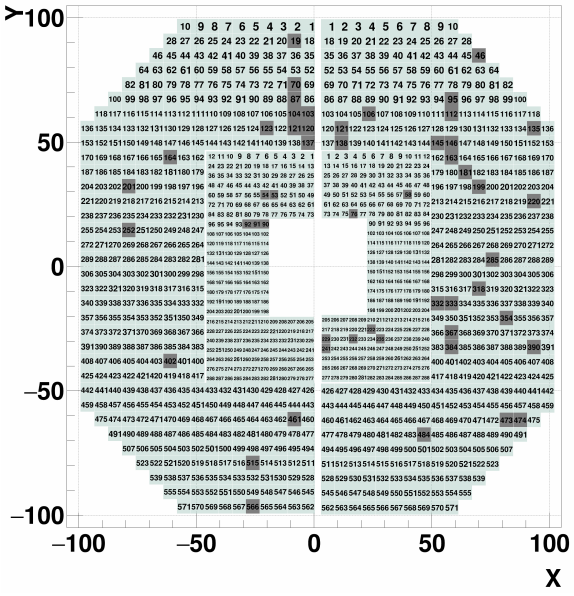

Figure 3.3: Run-11 bad channel in the FMS layout.

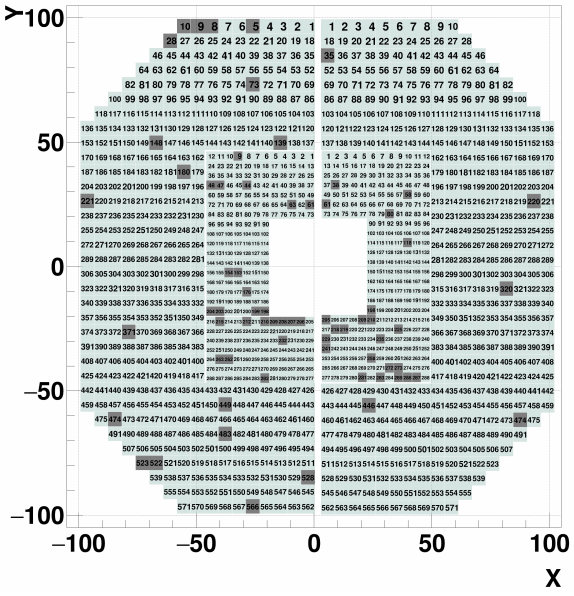

Figure 3.4: Run-15 bad channel in the FMS layout.

FMS operates at lower PMT voltage for optimization, the photon yield and also the ADC would decrease significantly so that the ADC would lose precision when it is recorded. As a countermeasure, the operator would change the bit definition by shifting it by one or more bits. In such operation, it is equivalent to multiply the ADC with a factor of $2 * bit_{shifit}$ for positive bit shift and $1/2 * bit\_shifit$ for negative bit shift.

Usually these changes are recorded in a log and thereafter put into the database. But in the offline QA, it is found that the one in the database was not consistent with what has been observed in the data. The reason why the database bit shift is not correct is not quite known. But it is possible to recover some of the bit shift information by looking into the data itself. Since the ADC after a positive bit shift could only record certain integers, one might discover if a channel has a positive bit shift or not by observing the ADC pattern. For example, in the case of +4 bit shift, the ADC could only be $4, 8...4 * n$ and any combination of them. It will exhibit a very clear stripe pattern when one checks the ADC distribution of such chancel. This method works for the positive bit shift, but not for the negative bit shift because one cannot tell whether the missing highest bit comes from the negative bit shift or simply there are no such high energy hits ever landing on this tower. The detail of bit shift QA can be found in this note[69]. In this note, it adopted the method discussed above to check the bit shift of Run-11 and Run-15. And it compared with the bit shift table in the database and then updated it if there was any conflict showed up. Eventually, the new founded bit shift table would merge into the one in the database. Figure(3.5) and Figure(3.6) show the final result of the bit shift channels in the FMS in Run-11 and Run-15.

3.3 FMS calibration

The FMS is calibrated by the mass of the reconstructed π^0. The high yield of the π^0 makes it possible to apply this method to each channel. The initial gain of each channel is determined by the tower and the corresponding PMT status. This provides a rough gain table for the detector which can be used in triggering. However, it is not accurate enough for the analysis. And the status of the detector could be changing during the run time. There are some situations that the gain would change significantly during data taking. For example, the radiation damage each tower suffered, and possible PMT high voltage adjustment. It requires an

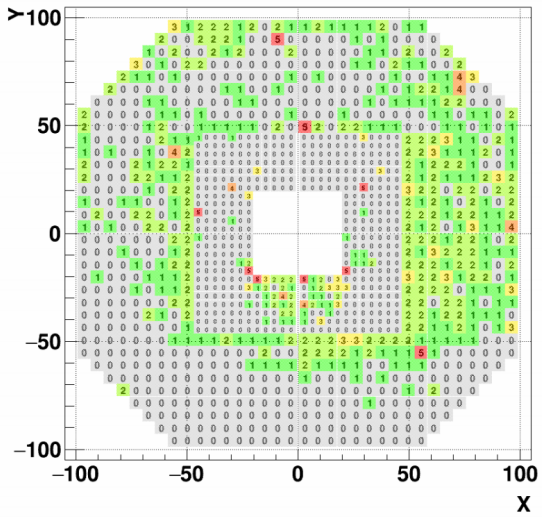

Figure 3.5: Run-11 bit shift for all the channels in the FMS layout.[69]

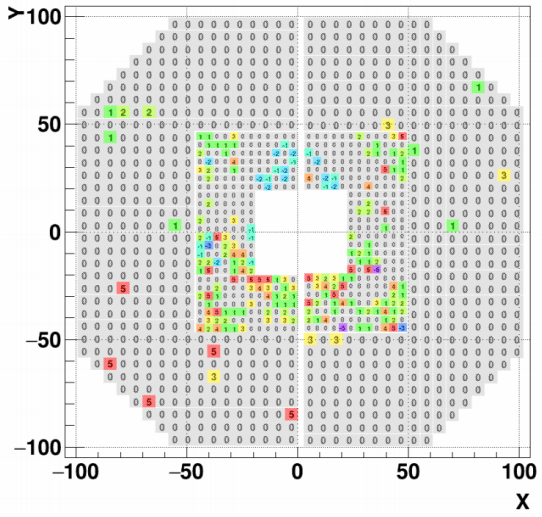

Figure 3.6: Run-15 bit shift for all the channels in the FMS layout.[69]

offline calibration to get the correct gain with better precision. The difficulty of using the π^0 mass to calibrate the channels is that the two decay photons from the π^0 always land on multiple towers. Therefore, to calibrate one channel, it must need the information of other channels. And Changing the gain of one channel must affect the others. There is a procedure for handling such correlations of the towers. The idea is to adjust the gain tower by tower recursively until all the gains of the channels converge. Usually it can be achieved in less than ten iterations. After all the channels finish their iterations, a gain correction factor is assigned to each of the channels.

The reconstruction detail of photon/pion will be discussed in the next section. The selection for π^0 is similar to the physics analysis because a good calibration relies on the good reconstruction. The only difference is that it requires the tower energy being larger than 30% of the total energy of the whole FMS cluster so that this tower plays a major role in its own calibration. There are a few additional rules for the calibration though. First, only the one-photon-type cluster would be used in the calibration. Otherwise, the result can be affected by the photon separation algorithm. Second, there are constraints on the π^0 energy range used in the calibration. The width of the range needs to be balanced between background, statistics and non-linear energy response. Lower energy means higher statistics but higher background. Wider energy range means higher statistics but stronger non-linear energy respond. Take the small cell as an example. For the upper limit, it is set to 45 GeV since decay photons from even higher energy π^0 become more difficult to form two clusters in the detector. And when they do, it is probably a mistake made by the algorithm. For the lower limit, it is set to 35 GeV. There are two reasons not to choose even lower energy. The first one is that the background increases a lot in lower energies. The second one is that the energy uncertainty of the reconstructed low energy photon is high. For the large cell, both the upper and the lower limits are lower than those in the small cell due to the larger cell size. The photons tend to merge into one cluster in lower energy given larger cell size. The final choice is 20-30 GeV for the large cell. There is an additional cut for the energy deposition in the calibrated tower.

In Run-11, there is another correction due to some problematic PMTs. Some of the PMTs suffered from broken zenner diodes, which causes the PMT gain to jump back and forth within minutes, even during a run. The LED flasher system was built to monitor this dynamically. The flasher system is made of an array

of optical fibers which link to each of the PMT in one end and to a LED light source in the other end. The LED constantly flashes to the PMTs every minute. Since it is totally different from normal events of proton collision, it can be easily detected by the relevant LED trigger or even the sum of the ADC of all the channels. By analyzing the change of the ADC, one can track down the sudden gain change. In the end, one can divide a run into several segments and assign an additional time-dependent correction factor to the gain. In Run 15, those problematic PMTs were replaced before the data taking. So the LED system is no longer needed in calibration afterward.

In summary, the overall gain is composed of three parts, see Equation(3.1).

$$Gain = initial\_gain * gain\_correction * time\_dependent\_gain\_correction \quad (3.1)$$

Not all the channels behave good enough in the iteration. The left panel of Figure(3.7) shows a good π^0 signal and the fitting works fine. The right panel shows no π^0 peak at all in this channel. So it is pointless trying to calibrate it in the first place. They are the problematic channels mentioned above in the QA section. These channels might have been damaged in some way. They cannot get clear π^0 signals, and therefore should be excluded in the iteration in case they contaminate the signals in other channels. They are marked as bad channels in the calibration and assigned zero to their gain correction factor, therefore excluded in the analysis. The overall bad channels including the hot ones and the problematic ones are plotted in Figure(3.3) and Figure(3.4).

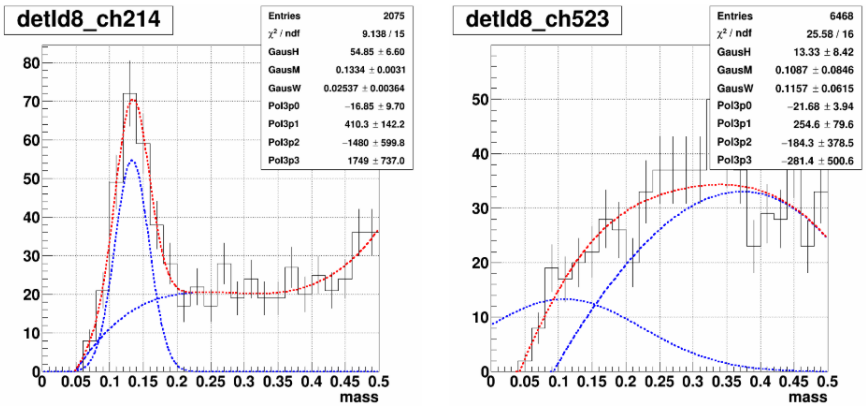

Figure 3.7: Example of good and bad tower in calibration[70].

3.4 Photon/Pion Reconstruction

The whole FMS is divided into 4 quadrants. Each one of them has an index called detector ID which is denoted as 8,9,10,11. Detector ID 8/9 refers to the northern/southern part of the large cell while 10/11 refers to the northern/southern part of the small cell. The reconstruction would be performed in each quadrant independently. That means if a photon lands on the edge of the two quadrants, it will be reconstructed as two photons in different quadrants. Since the small cell and large cell are different in size and material density, the reconstruction for them could be different in settings too.

There are three major steps to construct a π^0 candidate in the FMS, which are the cluster finding, shower shape fitting, and π^0 reconstruction. The basic reconstructed object in the FMS is the FMS hit. It refers to a tower with non-zero ADC. The cluster finding is meant to put several adjacent FMS hits together and form a FMS cluster. A FMS cluster could contain one or two FMS points in it which are photon candidates. The cluster finding also would identify which type the FMS cluster belongs to. After all clusters are found and processed, the shower shape fitting procedure is going to determine the position of the FMS point for each type of the cluster. In the end, a list of FMS points are generated and every two of them are used to build a π^0 candidate assuming they are from a decay π^0.

3.4.1 Cluster Finding

The first step is the cluster finding in the FMS. The minimum energy of the FMS hit participating in the cluster finding procedure is 0.01 GeV. Any FMS hit which passes this cut would be put into a pool to be processed. The FMS hits that have the highest energy within all the adjacent towers will be chosen as seed towers. All the other towers from another list are called the neighboring towers. They will be assigned to one of the seed towers based on the distance to the centroid of the seed tower. A seed tower with its assigned neighboring towers forms a FMS cluster. It is easy to recognize an isolated cluster. For those clusters that overlap with each other, the neighboring towers are assigned to one of the seed towers based on the distance to them. If the distances to more than one seed tower are equal, such neighboring towers are marked as ambiguous. After most seed towers are now associated with their neighboring towers, it is possible to calculate the cluster position with Equation(3.2).

Note that the weighting scheme in Equation(3.2) is logarithmic rather than linear. This comes from the former FPD research[71] which was a similar but smaller detector before the FMS. According to the research, the logarithmic weighting has an advantage of being insensitive to the cluster topologies, meaning whether the center of the cluster is close to a tower center or to the tower boundaries does not affect the cluster moments as much as that with linear weighting. There is an energy offset of 0.5 GeV in the equation, which means if tower energy is less than 0.5 GeV, its weight would be simply zero and excluded from the sum. Therefore there is a minimum energy requirement of 0.5 GeV for the FMS hits to come into the calculation of the position of the FMS cluster.

$$\begin{aligned} x_{clu} &= \frac{\sum_{i\in clu} \ln(E_i+0.5)x_i}{\sum_{i\in clu} \ln(E_i+0.5)} \\ y_{clu} &= \frac{\sum_{i\in clu} \ln(E_i+0.5)y_i}{\sum_{i\in clu} \ln(E_i+0.5)} \end{aligned} \tag{3.2}$$

The calculated position is used as the new seed centroid instead of the naive geometric centroid of the seed tower. After that, the ambiguous towers could be associated with each of the former reconstructed clusters again and integrated into the closest one. At last, all the towers end up being assigned to one cluster only. The cluster now has all its tower and the final position can be recalculated and the second order moment of the position also can be calculated using Equation(3.3), which would be used later.

$$\begin{aligned} \sigma_x^2 &= \frac{\sum_i \ln(E_i+0.5)(x_i-x_{clu})^2}{\sum_i \ln(E_i+0.5)} \\ \sigma_y^2 &= \frac{\sum_i \ln(E_i+0.5)(y_i-y_{clu})^2}{\sum_i \ln(E_i+0.5)} \\ \sigma_{xy}^2 = \sigma_{yx}^2 &= \frac{\sum_i \ln(E_i+0.5)(x_i-x_{clu})(y_i-y_{clu})}{\sum_i \ln(E_i+0.5)} \end{aligned} \tag{3.3}$$

It is known that the FMS cluster could contain one or two FMS points which are potentially photons. After the cluster finding is done, each cluster will be categorized into two groups based on its size and shape. One type is for the clusters which contain only one photon, the other type is for the clusters which contain two photons. At higher π^0 energies, the opening angle of the decay photons becomes very small, which increases the possibility that the two photons will merge into one cluster due to the tower size limit. This process is critical for a correct photon reconstruction. It is obvious that the algorithm of finding the photons in these two types of clusters would be very different, it is very important to clearly identify these two types. The only information can be used is the size of the cluster and energy distribution in it.

If a cluster is very small, meaning its tower number is less than 5, then it is automatically categorized as one photon cluster. Otherwise, it needs further examination. The categorization algorithm uses the parameter of $\sigma_{Max} * Energy$ to separate these two types. σ_{Max} is denoted as the second order moment of the tower position along the major axis of the cluster whose direction can be determined by Equation(3.4). The major axis of a cluster is similar to that ofan ellipse assuming the cluster has an elliptic shape. The Atan2 function in the equation is the generalized Arctangent function which maps a position(x,y) to its azimuthal angle.

$$\begin{aligned} \theta &= \tfrac{1}{2} Atan2(2\sigma_{xy}, \sqrt{\sigma_x^2 + 4\sigma_{xy}^2} + \sigma_x^2 - \sigma_y^2) \quad if(\sigma_x^2 > \sigma_y^2) \\ \theta &= \tfrac{1}{2} Atan2(\sqrt{\sigma_x^2 + 4\sigma_{xy}^2} + \sigma_x^2 - \sigma_y^2, 2\sigma_{xy}) \quad if(\sigma_x^2 > \sigma_y^2) \end{aligned} \tag{3.4}$$

The π^0 simulation[72] in the upper panels in Figure(3.8) shows the $\sigma_{Max} * Energy$ with respect to the π^0 energy. There are two clear separated bands representing two different types of clusters. The two-photon-type cluster in no doubt is larger in size and therefore sit on the upper band in the figure which is separated by the colored lines. However, this separation is not good enough since there is a photon background existing in the data. The photon simulation in the bottom panels in Figure(3.8) shows the $\sigma_{Max} * Energy$ for single photons. So there is a chance that a cluster which is from a high energy photon would be misidentified as a two-photon-type cluster. Although in the real data, this problem would not be so serious because of the low cross section of such high energy photon. So between the well-separated bands, the clusters are marked as ambiguous. The combination of the cuts of the colored lines for categorization is dividing the $\sigma_{Max} * Energy$ plot into several zones and judge which type a cluster belongs to based on its position in the plot. The cut combinations are listed in Table(3.3). They work for both large and small cell. In some zones, where the two types are well separated, it requires no more test and the cluster is ready for the next step. But for those clusters which are identified as ambiguous, they will try the corresponding shower shape fitting schemes for both types of the cluster in the next step and judge which way is better by the chi-square of the fitting.

3.4.2 Shower Shape Fitting

After the cluster categorization, the next step is to perform the photon shower shape fitting to determine the precise position of the FMS points. There is a

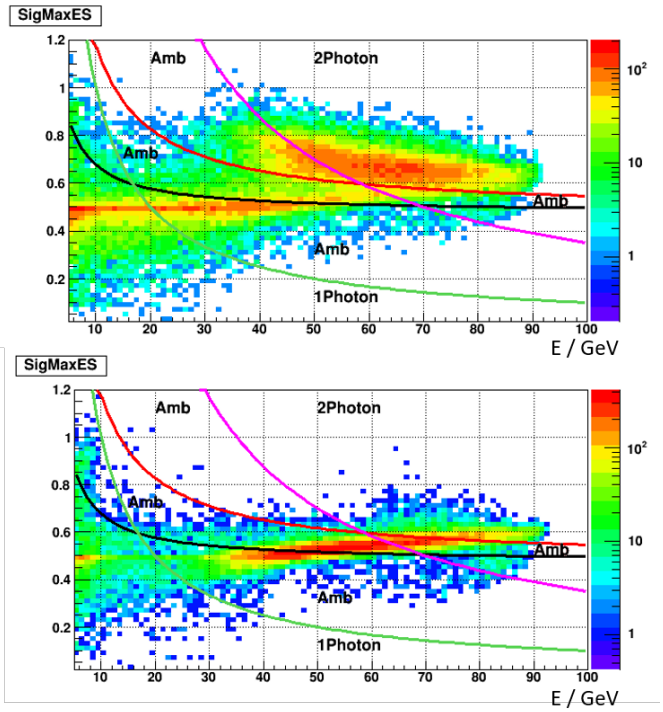

(a) Small cell

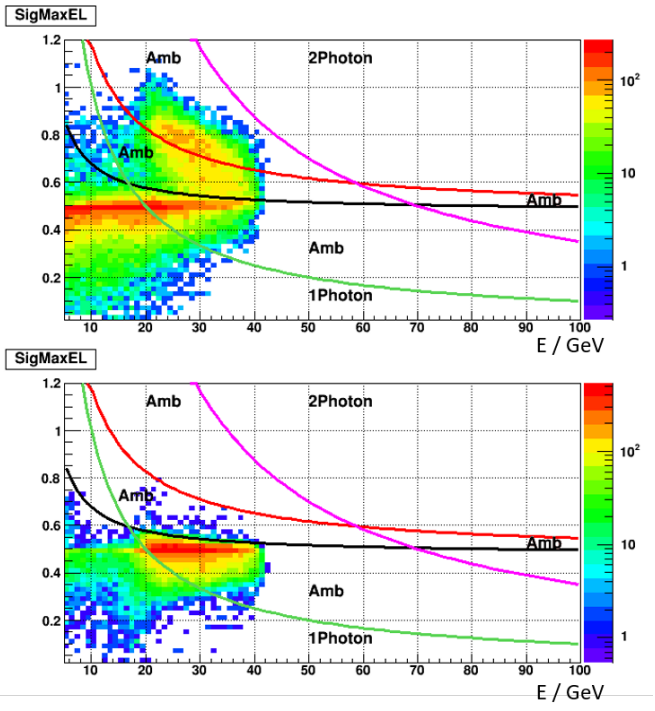

(b) Large cell

Figure 3.8: $\sigma_{Max} * Energy$ distribution verse energy in simulation[72]. Left panel is for small cell and right panel is for large cell. In each panel, the top figure is for single π^0 simulation and bottom figure is for single photon simulation.

Table 3.3: Cuts combination of the cluster categorization

Zone	Cuts	Identified as	Zone in the figure
1	$\sigma_{Max} > E/2.1 + 7.0$ & $\sigma_{Max} > 35/E$	two photon	Above red & Above magenta line
2	$\sigma_{Max}E > E/2.1 + 7.0$ & $\sigma_{Max}E < 35$	ambiguous	Above red & Below magenta line
3	$\sigma_{Max}E < E/2.1 + 2.0$ & $\sigma_{Max}E < 10$	one photon	Bleow black & Bleow green line
4	$\sigma_{Max}E < E/2.1 + 2.0$ & $\sigma_{Max}E > 10$	ambiguous	Bleow black & Bleow green line
5	everything else	ambiguous	Between red and black line

minimum energy cut for FMS cluster to get rid of the very low energy clusters which are not used in the analysis. In Run-11, it is 0.75/2 GeV for large/small cell while in Run-15, it is 0.5/0.5GeV.

When a photon hits the FMS, the energy would distribute isotropically around the hit point. Assuming the distribution pattern has already been known, when the position of the hit point is given, the energy deposition in a tower can be calculated by the distance of the tower to the hit point. Reversely, given the energy in each tower, this distribution pattern which is called the shower shape here could find the location of the hit point by a fit.

For a one-photon-type cluster, the shower shape fitting algorithm will try to pinpoint the actual location of the FMS point by setting an arbitrary position inside the cluster as the centroid of the FMS point and compare the distribution pattern with the actual one in the data. The best fitting result can indicate the location of the FMS point. The shower shape function has the following form as Equation(3.5)[73]. The parameters of a_is and b_is in the function are listed in Table(3.4).

$$\begin{aligned} f(x,y) &= \textstyle\sum_{i=1}^{3} a_i f_i(x,y) \\ f_i(x,y) &= \frac{1}{2\pi}\left[\frac{1}{1+\left(\frac{x}{b_i}\right)^2+\left(\frac{y}{b_i}\right)^2}\right]^{\frac{3}{2}} \end{aligned} \tag{3.5}$$

Function $f(x,y)$ is the differential form of the shower shape. It contains three identical isotropic functions of $(\frac{1}{1+r^2})^{\frac{3}{2}}$ with three parameters b_is which are

Table 3.4: Parameters of the shower shape function.

a1	a2	a3	b1	b2	b3
1.06841	0.150087	-0.171292	0.37491	0.860969	0.386676

used to describe the width of the shower and three parameters a_is which are the weight of each part. It represents the fraction of energy deposition in an area of $dx * dy$ located at position (x, y) when the photon is placed in the origin of the coordinate system.

Calculating the energy deposition inside a tower requires the integral form of the shower shape function, which is shown in Equation(3.6). It represents the integral of function $f(x, y)$ from $(-\infty, -\infty)$ to (x, y). Then the energy deposition inside a tower can be calculated by the combination of this function and the coordinates of the four corners of the tower, which is $G(x.y)$ shown in Equation(3.7). When the position of the FMS point is assumed to be somewhere within the cluster, the difference of the expected energy and the measured energy of each tower can be calculated. A weighted least squares estimation is used in the fit. The weight is the inverse of the error function in Equation(3.8). This error function is inherited from the early FPD research[71]. It is designed in such way so that the very small energy tower could have significant weight in the fitting since these towers on the boundary of the FMS point plays an important role in constraining the point position.

$$F(x,y) = \frac{1}{2\pi}\sum_{i=1}^{3} a_i \left[\arctan\left(\frac{x}{b_i}\right) + \arctan\left(\frac{y}{b_i}\right) + \arctan\left(\frac{xy}{b_i\sqrt{b_i^2+x^2+y^2}}\right)\right] \tag{3.6}$$

$$G(x,y) = F\left(x+\frac{d}{2}, y+\frac{d}{2}\right) - F\left(x-\frac{d}{2}, y+\frac{d}{2}\right) - F\left(x+\frac{d}{2}, y-\frac{d}{2}\right) + F\left(x-\frac{d}{2}, y-\frac{d}{2}\right) \tag{3.7}$$

$$Error = 0.03 * \left(\frac{E_{cell}}{E_{cluster}}\right)^{1-0.001*E_{cluster}} * \left(1-\frac{E_{cell}}{E_{cluster}}\right)^{1-0.007*E_{cluster}} * E_{cluster} + 0.01 \tag{3.8}$$

The same technique also applies to two-photon-type clusters. But it is more complicated because the positions of the two FMS points are correlated. The

positions are fixed on the major axis of the cluster, which leaves three free parameters for the positions. Two of them are the position of one FMS point and the third is the distance between the two FMS points. The total energy is fixed while the energy sharing between the two FMS points is not. The latter two variables are the exact ones which are used to calculate the invariant mass of the π^0. So the quality of the fitting directly impacts the reconstruction of the π^0 mass. The final step is to repeat the fitting again using the result of the first fit as the input parameters. The constraints on the position of the FMS points would loose up so that this secondary fit acts like a micro adjustment of positions. The energy, in the other way, is fixed in this secondary fit because there is a tendency to increase the total energy if otherwise. When the position and energy of all the FMS points are determined, they can be used to reconstruct π^0.

3.4.3 π^0 Reconstruction

The π^0 decay into two photons quickly after its production. After getting the full FMS point list, all of the FMS point pairs would be considered as a π^0 candidate. The π^0 mass can be calculated using the photon energy and position with Equation(3.9). θ is the opening angle of the two FMS points. It approximately equals to the distance of the two photons over the distance from the π^0 position to the vertex of the event. For two-photon-type cluster, the mass can be written as function of total energy and energy sharing $Z_{\gamma\gamma}$, like Equation(3.10). An example of the reconstructed π^0 mass distribution is shown in Figure(3.9). It has a clear peak around the 0.1345 GeV which is the known mass of π^0. The background comes from the combinations of the FMS points which are photons from two different π^0s or photons from η meson or hadrons depositing sizable amount of energy in the FMS. Later, the signal and background shape will be obtained from the simulation and used to get the signal fraction by fitting the mass distribution.

$$m = \sqrt{E_1 * E_2(2 - 2\cos(\theta))} \tag{3.9}$$

$$\begin{aligned} m &= \frac{1}{2} * E_{\text{total}} \sqrt{\left(1 - Z_{\gamma\gamma}^2\right) * (2 - 2\cos(\theta))} \\ Z_{\gamma\gamma} &= |(E1 - E2)/(E1 + E2)| \end{aligned} \tag{3.10}$$

The number of π^0 candidates increases rapidly with an increasing photon number since there are $n(n-1)/2$ π^0candidates for n photons, so does the back-

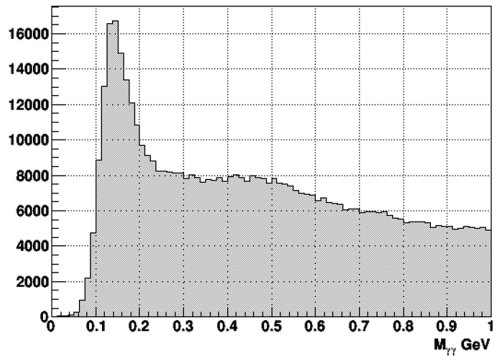

Figure 3.9: Reconstructed π^0 invariant mass between 38 to 43 GeV.

ground. In order to reduce the background, it is important to exclude some photons which are unreliable. The π^0 selection includes fiducial volume cut, $Z_{\gamma\gamma}$ cut, and energy cut.

The FMS clusters that are close to the edge of the detector, are missing part of their energies and cannot perform a decent shower shape fitting. So those FMS points whose location is along the outer edge of the large cell and inner edge of the small cell shall be removed from the FMS point list. The fiducial volume cut is set as half of the cell width. $Z_{\gamma\gamma} = \frac{E_1 - E_2}{E_1 + E_2}$ is the energy sharing of the two photons. In a two-photon-type cluster, when the two photons are so close enough, the shower shape fitting is unable to separate them. It is likely that the algorithm would assign most energy to one photon and very little to the other, which make the Z_{gg} closer to one. These photon pairs are unlikely to be in good quality. Thus the $Z_{\gamma\gamma}$ is required to be less than 0.7. A lower limit for the π^0 energy is also needed in the analysis because there is much more background in low energy region and especially the single photons being misidentified as two-photon-type clusters. So the asymmetry analysis only focuses on high energy π^0. In the TSSA analysis, the π^0 energy is chosen to be between 38 to 90 GeV. In the Collins asymmetry, the energy threshold is 10 GeV. It is different from the TSSA because the Collins asymmetry is measured as function of the ratio of π^0 energy over the jet energy which needs a lower energy limit when the ratio is low.

To ensure a unbiased inclusive pi^0 sample, an additional trigger-dependent transverse momentum cut is applied on the pi^0. The minimum transverse momentum for each trigger is 15% higher than the threshold of the specific trigger. The additional ratio of 15% is meant for the radiation damage effect in later of

the dataset. The threshold applied can be found in Table(3.5) and Table(3.6) .

Table 3.5: Minimum transverse momentum requirement for each trigger in Run-11

Run-11 Trigger	Run-11 Trigger ID	p_T cut (GeV)
FMSJP1	320220	1.84
FMSJP2	320231	2.88/2.05
FMSLgBS1	320226	1.72
FMSLgBS2	320227	2.53
FMSSmBS1	320222	0.92
FMSSmBS2	320223	1.61

Table 3.6: Minimum transverse momentum requirement for each trigger in Run-15

Run-15 Trigger	Run-15 Trigger ID	p_T cut (GeV)
FMSJP0	480830	1.84
FMSJP1	480809/480829	2.77
FMSJP2	480808/480828	3.68
FMSLgBS0	480804/480824/480844	1.26
FMSLgBS1	480805/480825	1.84
FMSLgBS2	480806/480826	2.76
FMSSmBS0	480801/480821/480841	1.26
FMSSmBS1	480802/480822	1.84
FMSSmBS2	480803	2.2
FMSSmBS2	480823/480843	2.53

3.5 Improvement of π^0 Reconstruction Algorithm

The major drive of improving the reconstruction algorithm is the increasing trend of π^0 mass with respect to the π^0 energy. Figure(3.10) shows such trend in Run-11 data. Note that the mass at 80 GeV is almost 50 MeV above the one at 40 GeV which is almost 40% higher than the know π^0 mass of 134.5 MeV. The original reconstruction algorithm has its limit on getting the right invariant mass for the high energy π^0. This trend appears both in simulation and data, which suggests it is not caused by the calibration of the data. Usually, a deviation

away from the exact π^0 mass is somehow acceptable since the asymmetry is determined by the events numbers in different spin patter of the collision beam in an asymmetry analysis. And the mass shape should remain identical in every spin pattern. What it does affect is the fitting when one tries to get the signal fraction for background subtraction. This makes it difficult to define a decent signal region and sideband region for the high energy bins. It also causes a lot of trouble to estimate the energy uncertainty and the quality of the calibration. The primary goal of the improvement is to understand the reason for the growth of the π^0 invariant mass and correct it. It turns out the lower limit of the distance of the two photons in the shower shape fitting is the major problem. In attempting to do this, there are some corrections and modifications which turn out not contributing greatly in solving the problem but do offer improvement on better precision of the π^0 energy and position. These corrections and modifications will be kept in the analysis. Altogether they will be discussed in this section.

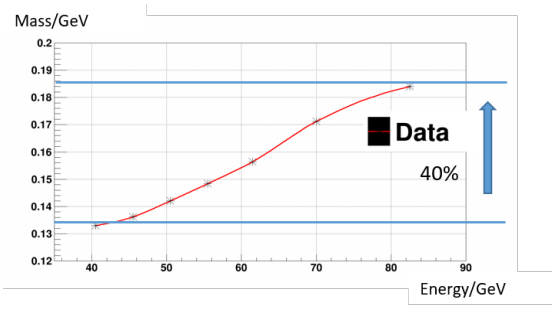

Figure 3.10: Growing reconstructed pion invariant mass versus the π^0 energy.

3.5.1 Vertex z Position Correction

The original reconstruction code assumes the vertex z position is zero. This could introduce a bias when the average vertex z position is not zero and increase the uncertainty of the FMS point position in the reconstruction. There are two ways for the vertex z position to affect the photon reconstruction. The first one is the incident angle which is used by the asymmetric shower shape model in Section(3.5.4). The second one is the opening angle of the two FMS points which is used to calculate the π^0 mass. The FMS itself does not have any information about the vertex in an event. Usually, in STAR, the time projection chamber(TPC) is used to find the vertex information. But the TPC has totally different coverage from the FMS and it is way slower than the FMS. When an

event triggers the FMS detector, there is not enough time for the TPC to collect enough information to find out the vertex in the event.

As an alternative, the beam-beam counter(BBC) is used to get the vertex z position. The BBC is a detector composed of two planes of very thin scintillators locating at both sides of the STAR detector. When a collision takes place and triggers the system, the BBC should record some particles passing through. When both sides of the BBC receive a signal, it is possible to calculate the vertex z position by measuring the different arriving time to the two sides of the BBC. Since the time difference of the BBC is given as a linear function of the actual time, it requires calibration to get the relation between the vertex z position and the BBC time difference. This calibration can be done using the events of low trigger rate where the TPC can record enough tracks. The result of this relation in Run-11 is shown in Figure(3.11). For each BBC time bin, the mean of the vertex z distribution is drawn as a black dot in the figure. A linear fit is done to get the function, and the result is $V_z = 633.544 - 0.158 * Time\_Diff$ (cm). Using this function, one could get the vertex z position in the FMS data chain.

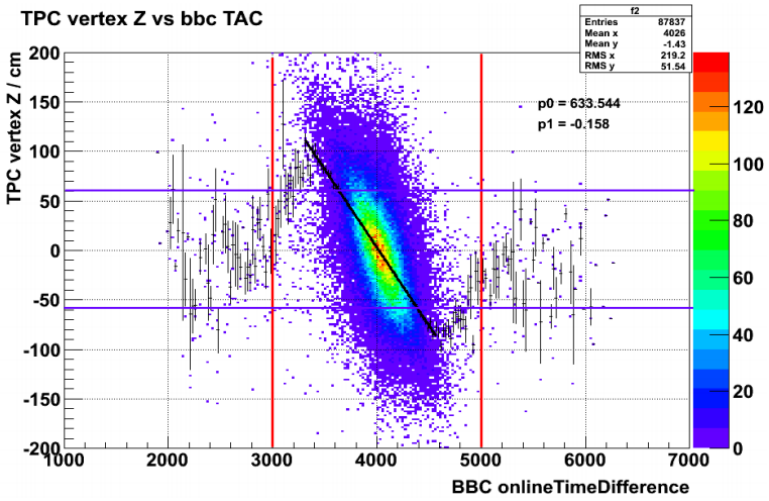

Figure 3.11: TPC vertex vs. BBC time difference in Run-11.

Figure(3.12) is an example of the vertex z position distribution for π^0 energy 38-43 GeV in Run-11 data. It is similar in other energy range. Note that there is an abnormal peak around zero. Those are the events that do not have the BBC time difference information in the data. This is because sometimes it is just one side of the BBC picking up a signal or even no signal for both sides. In that case, the vertex z position cannot be reconstructed in this method. Since the mean of

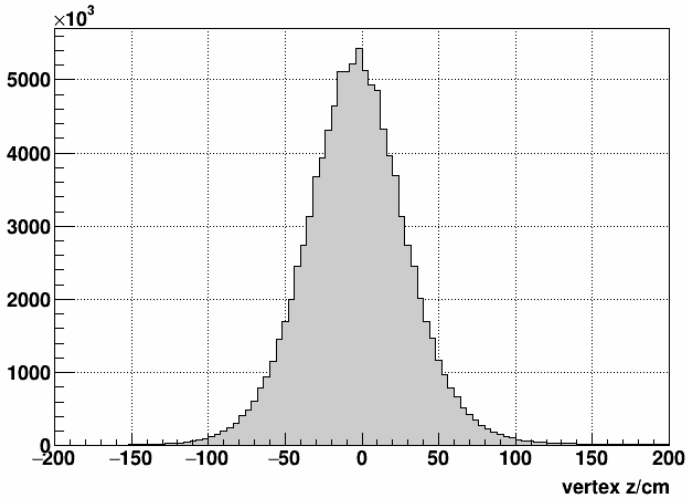

Figure 3.12: Example of vertex distribution of Run-11 data, with π^0 energy between 38 to 43 GeV.

the distribution centers at almost zero, it is appropriate to treat these vertex z positions as zero.

The Vertex calculation for Run-15 is similar to Run-11. The details can be found in this reference[74]. For Run-15, some of the FMS triggers are not set as energy threshold but transverse momentum threshold. And also the trigger time window in Run-15 is sometimes too short for the whole signal to pass through, which is an effect depending on the vertex-z position. As a result, the vertex z position is significantly biased by the triggers. Because the trigger system has no information about the actual vertex position, it has to assume all events happen at $z = 0cm$. So the events that take place at $z < 0cm$ would have an overestimated transverse momentum than it really does, which made it easier for them to trigger the system. This effect is energy dependent. When the π^0 energy is higher, it is more prominent, therefore the vertex z position is even further towards the negative direction. Figure(3.13) shows the vertex z position distribution for all π^0 energies in Run-15 data. Note that when there is no BBC time difference read from the detector(not shown in the figure), the vertex z position of such event will be set to -36 cm, which is the average vertex z position of all events recorded.

With these actual numbers, one can estimate the influence of the vertex information. Take Run-15 as an example. For the incident angle, it approximately equals to the distance of the photon to the center of the FMS over the distance of vertex z position to the FMS center. When the mean vertex z position is -35

cm, it is going to create a bias to the reconstruction by 5%. The width of the distribution can easily go up to 70 cm, which is about 10% change of the incident angle. As it will be discussed in Section(3.5.4), the incident angle is used in the shower shape to determine the photon position. For the opening angle of the two photons, it approximately equals to the distance between the two photons over the distance from the photons to the vertex. The 70 cm change in vertex z position could bring 8-14% change of the opening angle, which directly affects the reconstructed π^0 mass by the same amount of change. In conclusion, getting the right vertex z position is good for finding the π^0 position and reducing the uncertainty of the π^0 mass, not to mention that such influence would indirectly affect the analysis by affecting the photon reconstruction in the calibration.

Finally, the vertex z cut is set to $-70cm < z < 70cm$ for Run-11 and $-175cm < z < 105cm$ for Run-15.

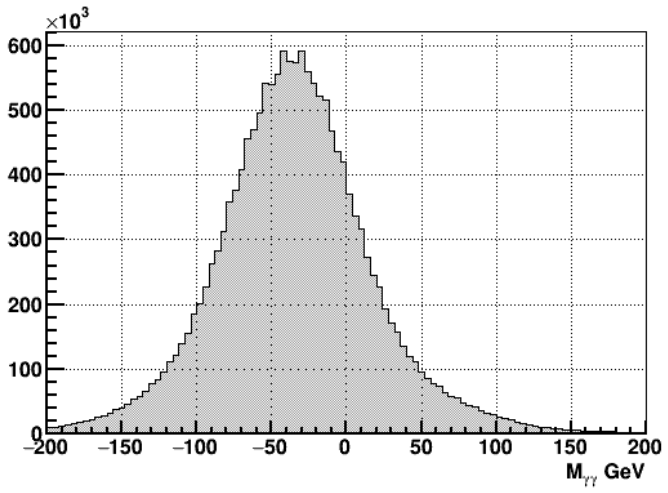

Figure 3.13: Example of vertex distribution of Run-15 data, with all π^0 energies.

3.5.2 Energy Correction

The non-linearity of the PMT response is a known issue of the FMS. It had been observed that the energy of the reconstructed FMS point was overestimated in higher energies. One of the evidence is the energy-dependent invariant mass of the high energy η meson whose decay photons do not merge in a cluster unlike the π^0, which makes it much simpler in photon reconstruction. This effect may be caused by the combined reasons of reflectivity of the Pb-glass and aluminized mylar interface, transparency of the Pb-glass and perhaps other unknown reasons.

These elements are either hard to find out or changing over time due to the radiation damage of the channel. What can be assured is that they altogether change the amount of the Cerenkov light production rate or survival probability when the EM-showers develops in the tower. Different energy photon develops the EM-shower at different depth of the Pb-glass. The distances that the Cerenkov photons need to travel to the PMT are also different and therefore they are affected by the effects mentioned above differently. As a result, it exhibits as the corruption of the linearity of the energy dependence of the Cerenkov photons received by the PMT, and equivalently as a non-linear response of the PMT in the measurement. The higher the photon energy is, the deeper the EM-show takes place, then the less distance the Cerenkov photons need to travel to the PMT, therefore the less influenced by the effects. Since the calibration of the FMS is done in a certain energy range, energy at the center of that range is considered well calibrated. But for other energies, the calibration is not suitable to use due to this non-linear effect. So when the calibration is done at some energy, for example, 20GeV for small cell in this analysis, the FMS point energy above 20 GeV is overestimated since it suffers from less energy loss than in 20 GeV while at the same time, the FMS point energy below 20 GeV is underestimated.

It would be beneficial to recreate this effect in the simulation. There was an attempt to adjust the shower shape by tuning the optical properties of the medium in this reference[71]. The tuning included the index of refraction, the absorption length in the Pb-glass, and surface reflection coefficients so that the shower shape in the simulation would coincide with the one in the data. These parameters were used in Cerenkov photon simulation of the FMS. It was found that the tuned model can lead to an energy-dependent gain, which is consistent with the discussion above.

In the Monte Carlo simulation, it would be inefficient to do a full Cerenkov photon tracking. For practical reason, a parameterization model is introduced in the simulation[75]. The attenuation model simply forces a fraction of the energy loss as function of the depth in the FMS tower. The attenuated energy follows Equation(3.11), in which L is the total length from the cell surface to the PMT, l is the distance from the cell surface. λ is the attenuation parameter, which is 0.03 and 0.04 for large and small cell respectively. In this model, the closer the shower is to the PMT end, the less the energy loss in Pb-glass, which coincides with the above discussion.

$$E_{attentuation} = E * \exp^{-\lambda*(L-l)} \tag{3.11}$$

In this analysis, the non-linear energy is corrected based on this attenuation model. Later it can be proved that such parameterization is effective. To learn about how to correct the reconstructed energy in the data, a series of single photon simulations with different energy from 3-85 GeV are done with this attenuation model. The sample of simulation is 5000 single photon events. The photons are targeting the FMS uniformly at pseudorapidity and azimuthal angle. After reconstructing the photons, one could compare the reconstructed energy with the input energy and obtain a correction factor from them. A requirement of photon number being one is placed on these events to filter the abnormal ones, in which the photon is mistakenly identified as two photons. An example of the photon energy distribution is shown in Figure(3.14) and is fitted with the skewed Gaussian function. A table of the comparison between reconstructed energy and the true energy can be generated eventually. A correction function can be made out of it using a second-order polynomial fit in Figure(3.15).

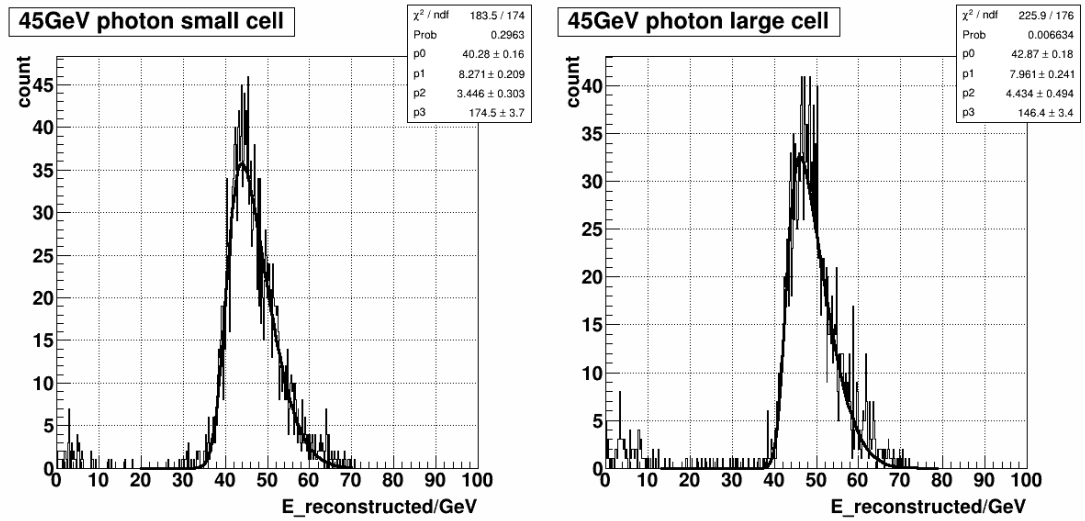

Figure 3.14: Energy of reconstructed photon in 45 GeV single photon simulation using scale factor 0.35, left panel is for large cell, right panel is for small cell, the black curve is the fitted result of a skewed Gaussian function.

However, this correction function cannot be used directly in the data, because of the inappropriate scale factor set in the simulation. According to the attenuation model, the restructured energy for a photon will be much less than its original energy due to the forced energy loss. So the reconstructed energy

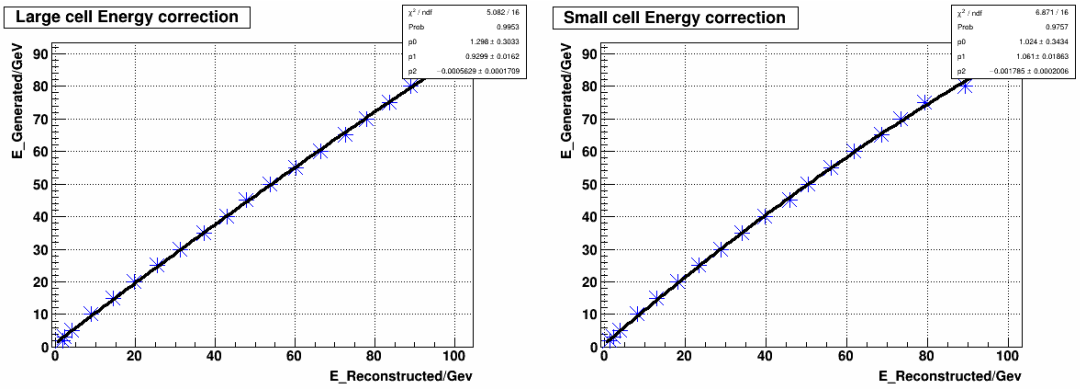

Figure 3.15: Energy correction function using scale factor 0.35, left panel is for large cell, right panel is for small cell, the black line is the fitted result of a second order polynomial.

needs to be divided by a scale factor which is less than one. The scale factor is somehow arbitrary. It was set to 0.35 in the simulation. Due to the non-linear nature, after scaling, there exists only one energy point which has a correct reconstructed energy and requires no further correction. Such point is called the "anchor point". Note that such point also exists in the calibration due to the same reason. In the calibration, the anchor point is the mean of the energy range that is chosen for the calibration. Only when the two anchor points are equal then the correction function obtained in the single photon simulations can be used in data. The current choice of the scale factor of 0.35 actually meant to set the anchor point right for the large cell which is 12.5 GeV in the calibration. But it certainly is not right for the small cell whose anchor point in the calibration is 20 GeV.

In simulation, the anchor point can be adjusted by changing the scale factor. Repeating the single photon simulations to find the new anchor point will be inconvenient but fortunately not necessary. Instead, the new scale factor and the corresponding energy correction function can be calculated given a new anchor point. Suppose the already known correction function F now has the form in Equation(3.12), it maps the reconstructed energy to its true value. The new anchor point E_{anchor} is set to the same one that used in the calibration. The new scale factor S_f can be obtained by solving Equation(3.13). The form of the correction function will change accordingly. G in Equation(3.14) is the new correction function corresponding to the new anchor point which can be obtained from the function F using the relation in Equation(3.14). For the anchor point

that used in this analysis for Run-11 and Run-15, which is 12.5/20 GeV for large and small cell respectively in Run-11 and 15 GeV for both large and small cell, the corresponding energy correction function is shown in Table(3.7) and Table(3.8).

$$F(E_{rec}) = E_{true} \tag{3.12}$$

$$F(E_{anchor}/0.35 * S_f) = E_{anchor} \tag{3.13}$$

$$G(E_{rec}) = F(E_{rec}/0.35 * S_f) = E_{true} \tag{3.14}$$

Table 3.7: Energy correction function for anchor point 12.5/20GeV for large and small cell in Run-11

Cell type	Correction function
Large	$1.177 + 0.915 * E_{rec} - 0.000754 * E_{rec}^2$
Small	$0.909 + 0.987 * E_{rec} - 0.00166 * E_{rec}^2$

Table 3.8: Energy correction function for anchor point 15GeV for large and small cell in Run-15

Cell type	Correction function
Large	$1.177 + 0.933 * E_{rec} - 0.000783 * E_{rec}^2$
Small	$0.909 + 0.963 * E_{rec} - 0.001577 * E_{rec}^2$

The validity of the attenuation model depends on the attenuation parameters used in the Cerenkov photon simulation. Since these parameters cannot be calculated analytically or measured from solid ground, its validity can only be examined by the data. In Run-15, there was a research which used the mass distribution of the η meson of different energies to correct the reconstructed photon energy[76]. The result is expressed as the ratio of reconstructed energy over the true energy $g(E_{true}) = E_{rec}/E_{ture}$. It contains three linear functions in different segments, see Equation(3.15) and Table(3.9). Its result can be used to compare the energy correction function obtained above. Note that both of the energy correction function has been set to the same anchor point. The comparison is shown in Figure(3.16) in which the blue points are from the attenuation model and the red circles for the Run-15 research. The black line is fitted result of the blue points using the second order polynomial. It can be seen that two correction functions are consistent with each other, especially in the region of less than 60

GeV which is heavily used in the analysis. So this can validate the choice of the attenuation parameters in the Cerenkov photon simulation.

$$g(E_{true}) = \begin{cases} g_A(E_{true}) = 1 - (N - K_t^A)\epsilon_B - (K_t^A - E_{true})\epsilon_A & E_{true} < K_t^A \\ g_B(E_{true}) = 1 - (N - E_{true})\epsilon_B & K_t^A < E_{true} < K_t^B \ \Gamma \\ g_C(E_{true}) = 1 - (N - K_t^B)\epsilon_B - (K_t^B - E_{true})\epsilon_C & E_{true} > K_t^B \end{cases} \tag{3.15}$$

Table 3.9: Parameters for the radiation damage model

Cell type	$N(GeV)$	$K_t^A(GeV)$	$K_t^B(GeV)$	ϵ_A	ϵ_B	ϵ_C
Large	12.5	8.6	20.1	0.015	0.0082	0.0023
Small	20	10.2	34.1	0.020	0.0048	0.0020

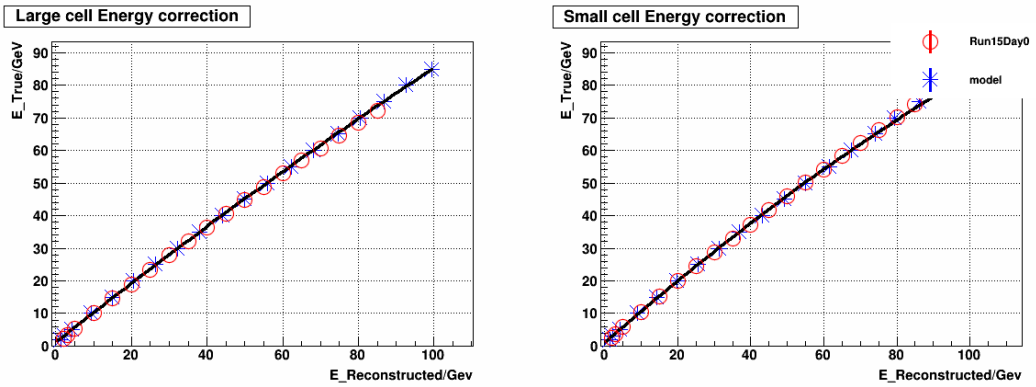

Figure 3.16: Energy correction function from model(blue point) and Run-15 research(red point),left panel is for large cell, right panel is for small cell, the black line is the fitted result of the model.

At last, let's review the improvement of the energy correction. For a photon with measured energy 40 GeV, the correction is about -7%. The mass of the π^0 which is made of two such photons should be corrected by -7%. It is a sizable effect although it can not be held fully responsible for overestimating the π^0 mass at the beginning of this section. The reason is as follow. In a rough estimation, the π^0 energy would be corrected from 80 GeV to 74.4 GeV which crosses the boundary to the lower energy bin in Figure(3.10). And the new 80 GeV π^0 samples are from the even higher energies like 90 GeV which has an even higher π^0 mass at the beginning. However, this improvement is very important in getting the right energy for π^0 and the electromagnetic jet.

3.5.3 Opening Angle

The opening angle of the two decay photons is directly related to the distance of the two FMS points which is a parameter in the shower shape fitting. At π^0 energies as high as 80 GeV, the distance of two decay photons with different energy sharing $Z_{\gamma\gamma}$, projected onto the surface of the FMS, is around 3 cm, see Table(3.10). Comparing it to the size of the small cell, 3.875cm, it is most likely that the two photons merge into one compact cluster, which makes it difficult to separate them. The original shower shape fitting parameters are designed for the Forward Pion Detector(FPD). The FPD is a decommissioned sub-detector in STAR[71]. The former research was aiming at modest π^0 energy around 40 GeV, where the average distance of the two decay photons is two times larger than that in 80 GeV. It turns out that the parameter limits inherited from the FPD research are the dominant source of the bias of the π^0 mass distribution in high energy.

Table 3.10: Distance of two photons in different kinematics

Pion energy(GeV)	$Z_{\gamma\gamma}$	Opening angle (radian)	Distance of two photon on FMS(cm)
40	0	0.007	4.86
40	0.4	0.007	5.30
40	0.7	0.009	6.81
80	0	0.003	2.43
80	0.4	0.004	2.65
80	0.7	0.005	3.40

The cluster type which matters in high energy π^0 is the two-photon-type. The lower limit of the distance of the two photons in shower shape fitting for this type was originally set in the way of Equation(3.16) which is a function of σ_{Max} and energy. It was obtained within a modest range of energy in simulation and extended to other energies. The half of the cell width limit is the constraint of the detector resolution. This function provides a lower limit which is higher than the theoretical one, which can be calculated by setting the $Z_{\gamma\gamma} = 0$ for a given total energy. However, in higher energy case, it fails to predict the right lower limit of the distance. The solution to this problem is to replace the original lower limit with the theoretical one instead of doing more simulations. The new

lower limit is set as Equation(3.17), where the vertex z position is considered in calculating the photon distance.

In a very rough estimation, this improvement account for about 60% of the π^0 mass bias in high energies.

$$lower\_limit = max(18/(\sigma_{Max} * E_{cluster})^{0.8}, 0.5) * cell\_width \tag{3.16}$$

$$lower\_limit = max(\frac{0.1345 * 2(735 - vertex\_z)}{E_{cluster}}, 0.5 * cell\_width) \tag{3.17}$$

3.5.4 Shower Shape and Incident Angle Effect

The function form of the shower shape is shown in Equation(3.5). Note that it is symmetric azimuthally because the shower shape model is built upon the assumption that the direction of the incident particle is perpendicular to the surface of the FMS. However, in the experiment, this assumption is only approximately true. Based on the geometry of the detector, the incident angle is never zero from the collision point to the FMS. Fitting a real shower in the FMS with a symmetric shower shape will introduce a displacement towards the radial direction and influence the fitting of two-photon-type cluster.

The FMS is about 7 meters away from the collision point. The towers of the FMS are 0.2 to 1 meters away from the beam pipe. So the incident angle could range from about 30 to 150 mrad. It is very small. But considering that the show maximum position for the large cell is about 20-30 cm from the surface of the detector, for a tower 70 cm away from the beam pipe, the displacement of the center of the shower can be as much as 3 cm, which is not a small number comparing to the cell size. It suggests that the non-zero incident angle is not a negligible effect. In this reference[77], the simulation shows the bias of position of the FMS point could be as much as half of the cell width using the symmetric shower shape.

The solution is to introduce an asymmetric shower shape. The strategy for building an asymmetric shower model is to maintain the original shower shape function form while it can vary according to different incident angles. In such an idea, the shower shape can be asymmetric as a whole, while it can also be viewed as the combinations of a series of symmetric shower shape at different depth. The longitudinal dependence of the shower shape can be learned in simulation. A 40 GeV single photon simulation was done in reference [55] to investigate the shower

shape and incorporate the incident angle effect. Only one energy is chosen in the simulation because the shower shapes are found to be almost energy-independent in data[78] and this conclusion can be backed up by this reference[79], in which the shower shape is investigated in simulation.

In this single photon simulation, the detector geometry was changed into a way that it is divided into six layers in the longitudinal direction. Each layer is chosen as 7.5 cm thick. It allows measuring how the shower develops transversely in each layer and the energy distribution in longitudinal direction. For a single layer, the displacement caused by the incident angle is considered invariant inside of it. So it can be treated as a simple case which the symmetric shower shape can describe the shower well enough. By fitting the shower layer by layer using the function form in Equation(3.6), one could get the six parameters for the shower shape for each layer. The normalization requires that the sum of the a_is in a layer is one. After that, a group of weight factors is needed to combine all six shower shapes. The weight is the energy fraction of a layer over the total energy. The weight in principle varies for different energy of the incident photon. But in this study, it is considered a higher order effect and the constant weight is used in this model.

The fitted shower shape parameters are shown in Table(3.11). When this new shower shape function is called by the fitting algorithm, the centroid of the shower in each layer (x_{ci}, y_{ci}) is linked by the incident angle which can be calculated based on the cluster position, which is shown in Equation(3.18). In the equation, θ is the incident angle and θ_x, θ_y are its components. They can be calculated as $\theta_x = x_{cluster}/Z, \theta_y = y_{cluster}/Z$ where Z is the distance from the collision point to the FMS centroid. In this way, the new shower shape is automatically asymmetric and incident angle dependent. The (x_{cmax}, y_{cmax}) in the equation are from the layer that has the highest weight which should contain the shower maximum. The position of the FMS point would be reported at the back of this layer which is 735.45 cm from the interaction point instead of a fixed shower maximum position in the original symmetric shower shape fitting which is 734.1/729.7 cm for the large/small cell.

Since the two types of cell are made of the same material, and only differ in size and density, in principle, this new shower shape which is obtained by the simulation in the small cell can be used for the large cell after minor modification. Since the radiation length for the large cell is designed as 1.5 times longer as that

of the small cell, the Moliere radius is the same amount larger. So the shower shape width should be enlarged by 1.5 times.

$$\begin{aligned} x_{ci} &= x_{cmax} + \tan\theta_x \left(z_{ci} - z_{c\max}\right) \\ y_{ci} &= y_{cmax} + \tan\theta_y \left(z_{ci} - z_{c\max}\right) \\ i \quad &for \quad ith \quad layer \end{aligned} \tag{3.18}$$

Table 3.11: Asymmetric shower shape parameters for small cell

a1	a2	a3	b1	b2	b3	Weight
0.998	0.222	-0.221	0.177	0.000473	0.178	0.0372
1.077	-0.0281	-0.0489	0.199	3.50	2.35	0.202
1.079	0.0650	-0.144	0.446	0.00544	1.64	0.293
0.922	0.0778	1.07e-07	0.593	0.619	3.49	0.236
0.999	0.000151	2.20e-07	0.949	1.84	3.40	0.146
0.997	0.00254	1.02e-06	1.43	2.91	3.44	0.0832

3.5.5 Testing the Improvement in Simulation and Data

After discussing all the efforts above, a final test is needed to see if they can solve the problem of high energy π^0 mass distribution. A simple but effective test to check the improvements is to see whether the π^0 invariant mass can be correctly reconstructed in high energy single π^0 simulation which is isolated from any interference from the background. The test sample in simulation is 80 GeV π^0 which uniformly targeting at the whole FMS coverage with vertex positioning at the origin. The selection cuts are chosen the same as in data. The invariant mass distribution is shown in Figure(3.17) top left panel. The mean of the peak is much closer to 0.1345 GeV, which was almost 40% higher before. The quality of the π^0 reconstruction depends on the three elements that are used to calculate the invariant mass, the energy, the energy sharing, and the opening angle, see Equation(3.10). The other three panels in Figure(3.17) show the differences between the reconstructed and true value of these three elements. All three of them suggest that the biases from the reconstruction are relatively small. This is clear evidence that the modifications of the reconstruction algorithm work as expected.

The final check is π^0 reconstruction in the data. With the improved π^0 mass shape, the π^0 mass fitting is more stable and more reliable. The fitted means of

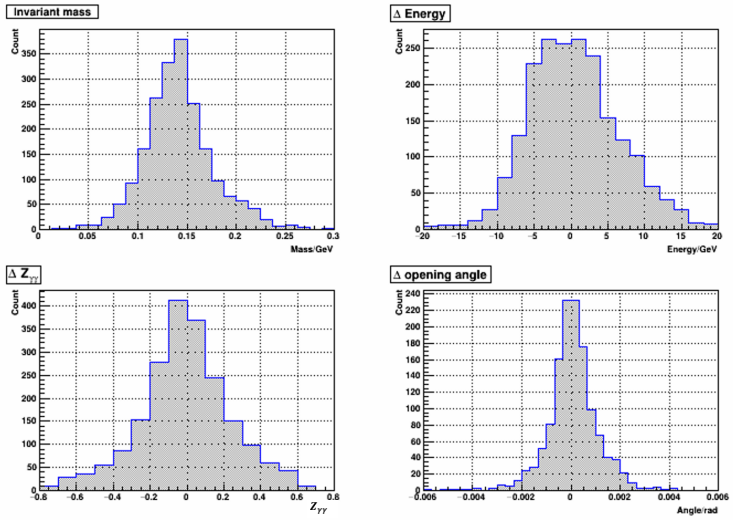

Figure 3.17: Reconstruction quality in single pion simulation. Top left panel for pion mass, top right panel for energy difference , bottom left for $Z_{\gamma\gamma}$ difference, bottom right for the opening angle difference.

different energies are shown in Figure(3.18). It can be seen that the mass now maintains stable across 40 to 80 GeV. Note that the mass means is still 3 to 5% higher than it should be.

There are several reasons for it. The first one is the possible bias from the gain obtained in calibration, energy correction, and mass fitting. The second one is that there is additional energy coming from other particles in the data, which cannot be separated from the photon and overestimates the π^0 energy. The last one is from the cluster finding. For high energy π^0, the decay photons are very close to each other and form a two-photon-type cluster. But there is a small chance that the cluster finding algorithm could identify it as two separated clusters. And the two FMS points from such clusters would tend to have an overestimated opening angle, thus have a higher mass. With all these reasons, 5% biases are understandable and acceptable for the analysis. The mass means being stable across the energies is good enough for most scenarios in the analysis, such as defining reasonable signal and background regions for fitting the mass distribution.

3.6 Jet Reconstruction

The Collins asymmetry analysis requires the reconstruction of π^0 within a jet. Thus the basic steps would be jet finding and correlation with the π^0. The

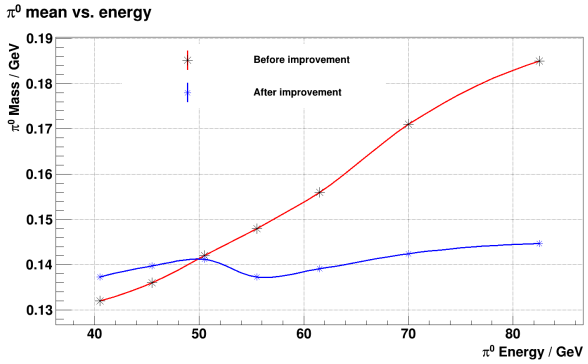

Figure 3.18: Comparison of π^0 mass shift as function of the energy in data. Blue line for after improvement, red line for before the improvement.

jet reconstruction for the analysis is similar to other jet analysis in STAR[13]. In this analysis, the anti-kT algorithm with jet parameter R=0.7 is used within the FastJet framework[80], because this algorithm proves to be less susceptible to diffuse soft background from pile-up and underlying events in the mid-rapidity jet analysis. Unlike the mid-rapidity jet analysis, the TPC does not come into use due to its limited coverage. So there would be no tracking for charged particles. Also, the FMS itself is unable to detect the charged hadrons. Therefore, the reconstructed jets are not the full jets but electromagnetic jets(EM-jets) since it only has the electromagnetic component. The word "jet" refers to EM-jet in the analysis without further notice unless in specific cases.

In practices, the jet finding algorithm is feed with the FMS points with their energies and positions instead of the clusters or towers. Since the FMS point energy suffers from the non-linear effect. It needs to be corrected before the jet finding to get better energy and position precision. For obvious reason, most of the cuts used in general jet analysis do not apply to the FMS. The only cut for jet finding is that the jet p_T is required to be larger than 2 GeV to reject soft background. Figure(3.19) shows the kinematics of the reconstructed jets. The energy and Pt distribution after the Pt cut are on the first row. The double peak in the pseudorapidity distribution on the bottom left is due to the trigger mixing. The ϕ distribution represents the acceptance and efficiency of the FMS.

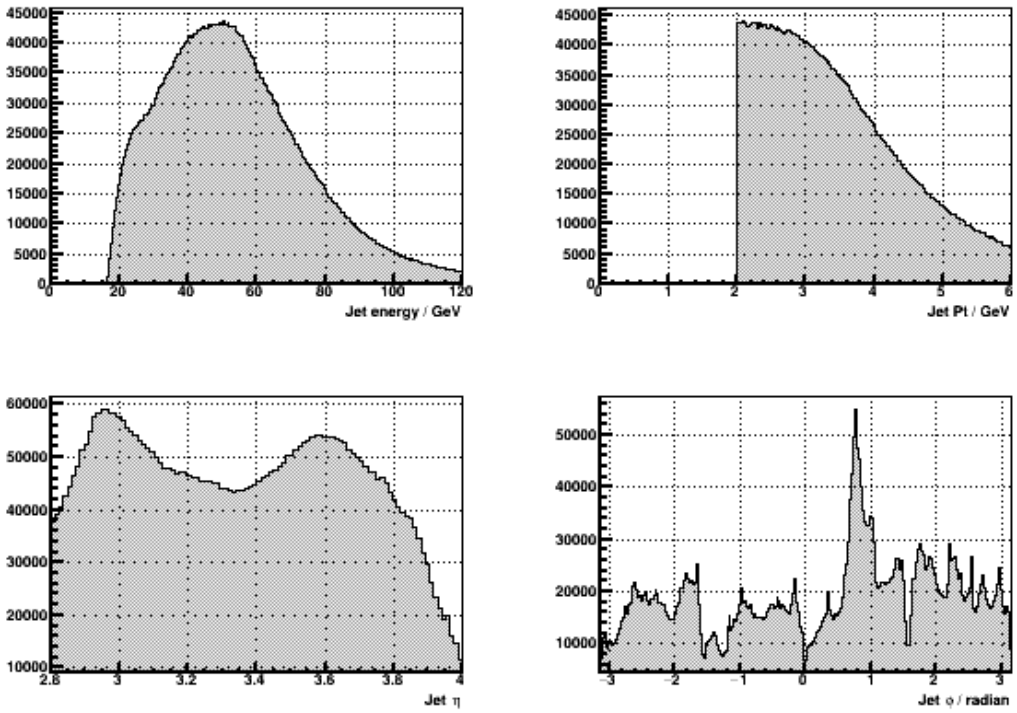

Figure 3.19: Example of Jet kinematics, top left: energy; top right: Pt; bottom left: pseudorapidity; bottom right: azimuthal angle.

3.7 Simulation

In order to learn about the background shape in the π^0 mass and the systematic uncertainty of the measurement, a Monte-Carlo simulation is done for this analysis. The simulation used the "starsim" program which is the standard simulation framework in STAR. This framework is based on GEANT 3[81]. The geometry of the whole STAR detector for a specific year has been stored in the database in GEANT format. PYTHIA 6.4[82] is chosen as the event generator, which provides the whole event information of the collision as the input of the simulation. The simulation receives the incoming particles from the event generator and put them through GEANT. These particles generate "hits" in GEANT when they travel through and interact with the material of the detectors. In the final step, the detector readout in the simulation will be stored and put into the data production chain so that it has the same format as in data and ready to be analyzed.

3.7.1 Simulation Setup

The PYTHIA version is chosen as 6.4.28. The tune version is *tuneA* with parameter PARP(90) set to 0.213. Input PDF is CTEQ6[83]. The version of the geometry of the STAR detector is y2011b, which has integrated with the attenuation model. The "ckin" parameter which describes the collision parton transverse momentum is set to three segments, 2-3 GeV, 3-5 GeV, and 5-8 GeV. The high ckin range is used to get more statistics for high energy π^0 event. In the end, all three parts will merge into one with a proper re-weighting. The weight for a specific ckin bin is determined by the overall luminosity of the simulation sample, which can be calculated by the cross-section and total attempt number provided by the event generator. The whole Run-11 simulation sample includes 3.5M filtered events for each ckin bin.

Since most of the events produced by the event generator are unable to deposit enough energy in the FMS in the simulation, it would be a waste of time trying to produce all of them. Usually, the simulation time is dominated by the detector level simulation and production. The generator level takes almost no time compared to them. Therefore, a way to increase simulation efficiency is to filter the events before they go into the detector level. The filter used in the simulation requires minimum energy targeting at a certain amount of area in the FMS. These areas are divided into two similar groups. For each group, the FMS is divided into four equal quadrants. The solid lines in Figure(3.20) represent one group and the dash lines represent the other which is just 45-degree rotation of the first group. This scheme is a very rough resemblance of the FMS board sum trigger.

The minimum energy is set to 70 GeV for the sum energy of the particles aiming at any one of these quadrants. The final state charged hadron only count as 75% of its energy in the sum energy. The particles heading to the FMS contain some final state stable charged hadrons, which at most cases leave minimum ionization energy about 100 MeV in the detector and at very small chance leave sizable energy in it. These hadrons provide valuable information about the background and therefore not suitable to be abandoned at the generator level. Therefore, if the energy threshold is set too low, the π^0 within might not be high enough energy for the analysis. So this threshold has to be set high enough to avoid wasting time producing useless simulation data. There could be concerns

that this cut filters some of the useful events which contain a high energy π^0 and low energy background. But after comparing the result from different cuts at 40 and 70 GeV, it shows that such influence is minimum.

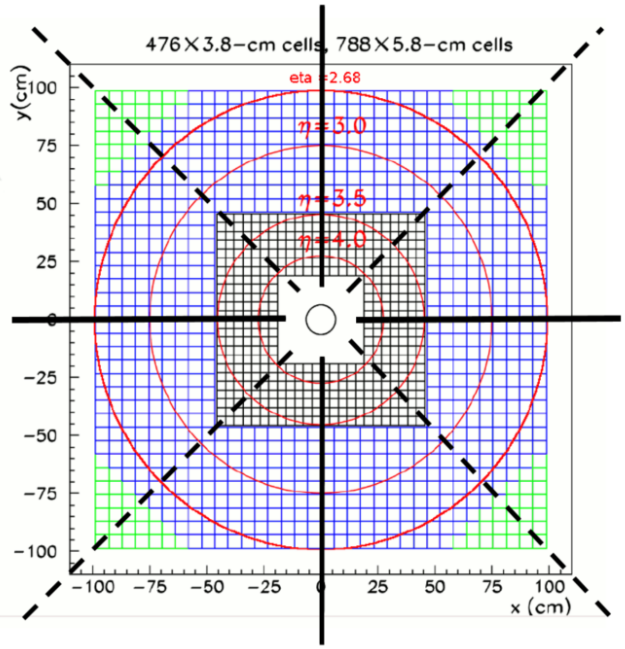

Figure 3.20: The area on the FMS used in the event filter.

In the Collins asymmetry analysis, it requires jet reconstruction. And it is also needed in the simulation to learn about the difference between detector level jet and particle level jet so that the detector effect can be understood and corrections can be made accordingly. In the simulation, the detector jet refers to the jet which is reconstructed with the particles that picked up by the detector and the particle jet refers to the jet that is reconstructed with the particles read from the output particle list of the event generator. So the differences between these two level of jets can reveal the effect of the detector. In order to make a meaningful comparison, the jet reconstruction algorithm, cuts, and parameters are the same as the one used in the data jet reconstruction. Note that in the data analysis, the jet is only EM-jet instead of a full jet. So the particle level jet also works in the same way by excluding the charged hadrons from the particle list.

3.7.2 Geometric Matching

In order to check any difference of an object before and after the detector response, a geometric match is needed for that. The object can be a photon or a jet. It aims at identifying the same object after the reconstruction by the detector. Normally the incident object is pretty close to its reconstructed position. In practice, the opening angle of the between the reconstructed object and the generator level particle is used to measure the distance between them. The direction of the two objects can form a cone, see Figure(3.21). The solid angle of the cone can represent how close the two objects are. For a small solid angle, it approximately equals to $\pi\theta^2$, where θ is the opening angle of the two objects. In this definition, the actual distance of the projection of the two objects on the FMS in the unit of centimeter can be simply calculated by $R\theta$, where R is the distance from the collision point to the hit on the detector. This is straight-forward in the geometric matching.

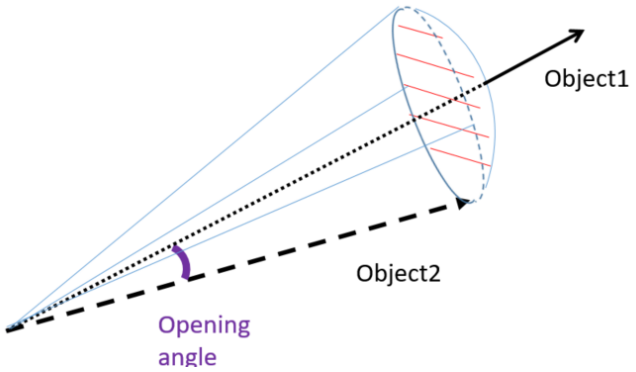

Figure 3.21: Opening angle in the geometric match.

All the FMS points will attempt to get a match with every particle in the generator particle list. For photons, the criteria for a match is $\theta < 0.008$ and $\Delta E < 1/3E$. This $\theta = 0.008$ approximately equals to 5-6 cm distance on the FMS. The energy cut is based on the energy distribution obtained in the single photon simulation. The Same criteria are applied to electrons although electron yield is negligible anyway. For charged hadrons, there is no energy requirement, since the energy deposition is unknown which can be from minimum ionization energy to a sizable portion of the hadron energy. If more than one possible match appears, it would be identified as the closest photon. The matched photons fall into three categories based on its mother particle, which could be π^0, η meson and others.

The FMS point pairs can be identified as signal and background based on the matching condition of these points. The signal is that two FMS points have matched with two different photons which come from the same mother particle of a π^0. The background includes everything else. The dominant source of background comes from 1.) one of the two FMS points is matched with a hadron 2.) two FMS points are matched with photons not from the same π^0. The matched single and background mass distribution is shown in Figure(3.22).

The particle jet is made of particles from the generator final state particle list. The list only keeps the electrons and photons and excludes everything else. The jet finding program is applied to these particles with the same algorithm as in data, which is anti-kT with parameter $R = 0.7$. There is also a minimum Pt=2 GeV requirement for the particle jet just like in the data. It has been observed that there is only one or zero particle jet per event. For such a particle jet, it will try to get a match with the detector jet, with the opening angle cut 0.04. If more than one detector jet is matched, it will choose the closest one which has the minimum ΔR.

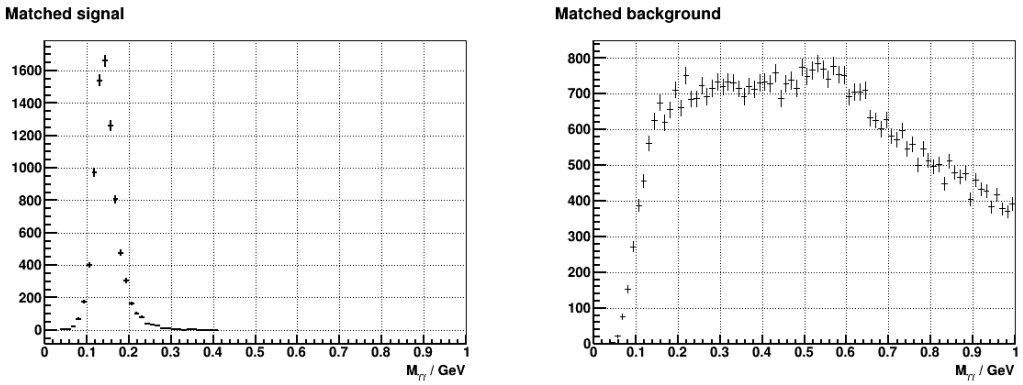

Figure 3.22: Matched signal and background mass distribution in energy 38-43 GeV.

The efficiency of the geometric matching for FMS point pair is about 60-70%. This is due to multiple reasons including misidentification and background interference. However, if the unmatched FMS point pairs have similar mass distribution as the matched one's, then this does not affect extracting the right signal and background shape for π^0 mass fitting. Figure(3.23) shows the comparison of the unmatched FMS point pairs(red) and the overall pairs in energy 38-43 GeV. It has been normalized in the mass window 0-0.4 GeV. It can be seen that two mass shapes are almost identical to each other. Same conclusions can be drawn

from other energies.

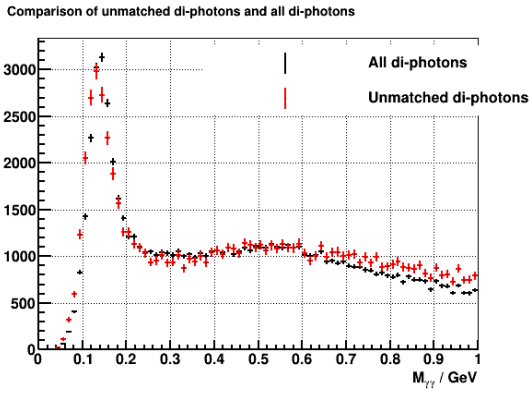

Figure 3.23: Comparison of the unmatched FMS point pairs(red) and the overall di-photons in energy 38-43 GeV.

3.7.3 Data-Simulation Comparison

One of the major task for the simulation is to get the signal and background shape for π^0 mass fitting. So it is important that the mass distribution in the simulation could reflect the feature of that in the data. Figure(3.24) shows the comparison of the mass in data and simulation within pion energy 38 to 43 GeV. It decomposes the mass into three types: both FMS points from the small cell, both points from the large cell, one point from the small cell and one point from the large cell. It shows that the former two types are pretty well described by the simulation. For the last type, the signal peak in the data seems to be lower than the exact π^0 mass. This could be explained by the difference of the geometry on the border of two cell type in the real detector and simulation. Fortunately, the yield of this type of FMS point pairs is relatively low compared to the other two types. Therefore it has limited impact in the mass window below 0.4 GeV. This comparison validates the method which uses the signal and background shape extracted from simulation in the data fitting.

In higher energies, the comparison does not appear as good as 40 GeV. It is mostly due to the following reasons. The first one is that the multiplicity in the simulation is less than that in the data. This is because either the cross section cannot be well described by the event generator, or some element like the beam remnant is poorly simulated. As a result, it makes less combinatoric background in the simulation. The second reason is that the energy smearing is worse in the data for higher energies which change the skewness shape and variance of

the π^0 signal. The third reason is that the simulation does not account for the trigger mix in the data. And the last reason is that the simulation does not suffer from any uncertainty from the calibration. Overall, it needs to loose some constraints of the parameters in the fitting which requires cautions. With all these inconveniences, it is always harder to get a decent fit for high energy π^0.

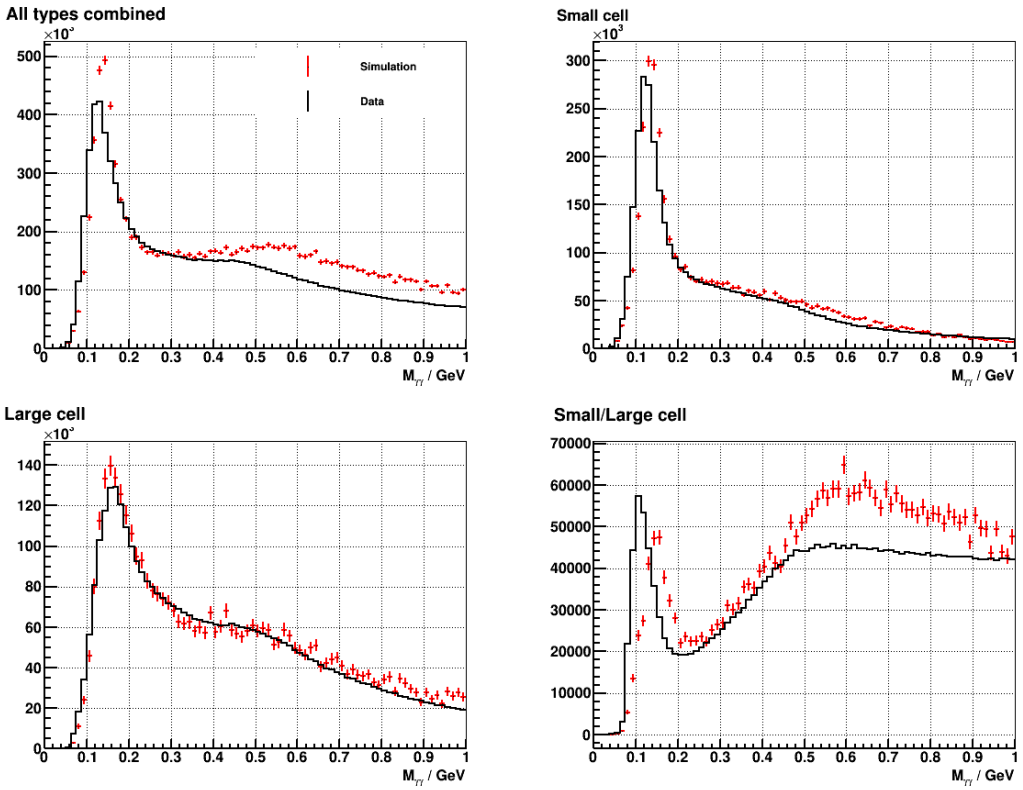

Figure 3.24: Data simulation comparison of pion mass distribution of different type. Top left: all types combined; Top right: small cell; Bottom left: large cell; bottom right: one point in small cell, one in large cell. Normalized in mass window 0 - 0.4 GeV. Red points for simulation, black points for data; Energy range: 38 to 43 GeV.

3.8 Calculation of the Asymmetries

The dataset is divided into several subsets, each corresponding to a fill. A fill represents an injection and store cycle of the proton beams in RHIC for collisions. A fill usually lasts about 6 to 8 hours for the proton-proton collision. The asymmetries are calculated fill-by-fill and then averaged.

In this analysis, the inclusive π^0 transverse single spin asymmetries(TSSA) are measured as function of the Feynman-x, which is defined as the longitudinal momentum fraction $x_F = 2p_L/\sqrt{s}$. It approximately equals to the π^0 energy divided by the proton beam energy. The Collins asymmetries are measured as function of z_{em} which is the π^0 energy fraction in a jet and the subscript em refers to the electromagnetic jet. The final results and estimation of their uncertainties will be discussed in the next chapter.

The calculations of the TSSA and Collins asymmetry are very similar in general. Both of them take advantage of the so-called cross-ration method. This section will use the TSSA as an example. And the difference will be discussed in the section of Collins asymmetry.

3.8.1 Cross-ratio Method

In the experiment, the measurement of π^0 TSSA in essential measures the azimuthal dependence of the π^0 production for polarized collision beam, like Equation(3.19). In the equation, N is the π^0 yield measured in the experiment; σ is the unpolarized differential cross-section of the π^0; ϵ is the acceptance and efficiency of the detector; $\mathcal{L}$ is the luminosity of the beam; pol is the polarization of the beam; the arrow represents the spin pattern of the polarized beam; the $cos\phi$ is the modulation of the azimuthal angle of π^0 relative to beam spin direction. It is pretty hard to calculate the asymmetry directly from this equation due to the nonuniform detector acceptance and time variant luminosity. The cross-ratio method takes advantage of the detector symmetry and cancels these factors in calculation. The A_N calculation is shown in Equation(3.20). It can be deduced from the form in Equation(3.19).

$$\begin{aligned} N^{\uparrow}(\phi) &= \epsilon \mathcal{L}^{\uparrow} \sigma^{\uparrow} \\ &= \epsilon \mathcal{L}^{\uparrow} \left(1 + pol * A_N \cos\phi\right) \ \sigma \end{aligned} \tag{3.19}$$

$$pol \cdot A_N^{\text{total}} \cos\phi = \frac{\sqrt{N^{\uparrow}(\phi) N^{\downarrow}(\phi+\pi)} - \sqrt{N^{\downarrow}(\phi) N^{\uparrow}(\phi+\pi)}}{\sqrt{N^{\uparrow}(\phi) N^{\downarrow}(\phi+\pi)} + \sqrt{N^{\downarrow}(\phi) N^{\uparrow}(\phi+\pi)}} \tag{3.20}$$

In practice, the N in the equation is the raw yield of the π^0 candidates in a certain spin pattern within some azimuthal angle range. The azimuthal angle ϕ

is divided into ten bins, see Figure(3.25). Since the bins of ϕ and $\phi + \pi$ are used simultaneously, eventually there are five data points in Equation(3.20). Each of them are plotted as function the $cos\phi$, where ϕ is center of the bin. In doing so, the result of the right hand side in Equation(3.20) should fall on a line and $pol * A_N$ is the slope of the 1st order polynomial fitting. Figure(3.26) shows an example of extracting the asymmetry from the raw yield.

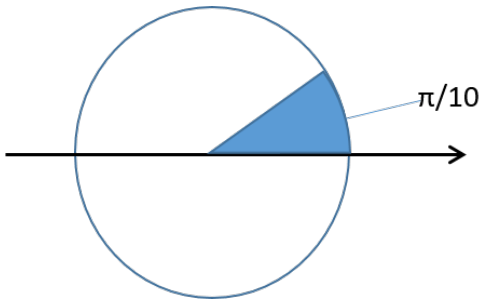

Figure 3.25: Ten ϕ bins divided in the FMS for asymmetry calculation. Blue shade is first bin centering at $\pi/10$.

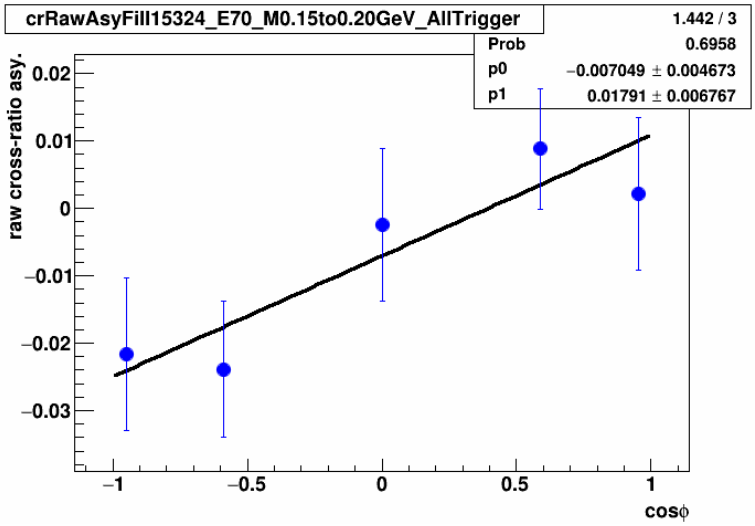

Figure 3.26: Example of getting the raw asymmetry for a specific mass and energy range using the cross-ratio method。

The spin patter in STAR has the definition as in Table(3.12). Each bunch of two collision beams has its own spin pattern and can be accessed at the event level. So by manipulating the combination of the spin patterns, one can get a data sample of physical interest. For example, the spin pattern "5"+"6" is for a polarized blue beam with upward spin direction.

Table 3.12: Spin pattern definition in STAR

Spin pattern	Blue beam spin direction	Yellow beam spin direction
5	down	down
6	down	up
9	up	down
10	up	up

3.8.2 Signal Extraction

The raw asymmetry is a combination of the signal and the background asymmetry. The non-trivial signal asymmetry need to be extracted using the Equation(3.21). The raw asymmetry is divided into two parts. One is calculated in the signal region, the other in the side band region. These regions are arbitrary defined mass windows which are considered rich in signal(signal region) and background(side band region). The whole mass range is chosen as $0.0 < M < 0.3GeV$. There is hardly any signal beyond this range. The signal region is chosen as $0.0GeV < M < 0.2$ GeV. The side band region is $0.2 < M < 0.3$ GeV. It is already assumed that the average background asymmetries are the same in the signal region and the two sideband regions. There are two terms, $f_{\mathrm{sig}_{sig}}$ and $f_{\mathrm{sig}_{sb}}$, representing fraction of signal in signal region and in side band region.

$$\begin{aligned} A_N^{\mathrm{raw}_{sig}} &= f_{\mathrm{sig}_{sig}} * A_N^{\pi^0} + (1 - f_{\mathrm{sig}_{sig}}) * A_N^{bkg} \\ A_N^{\mathrm{raw}_{sb}} &= f_{\mathrm{sig}_{sb}} * A_N^{\pi^0} + (1 - f_{sig_{sb}}) * A_N^{bkg} \end{aligned} \tag{3.21}$$

The signal and background shapes for π^0 invariant mass distribution in each energy bin are extracted from Monte Carlo simulation. In this analysis, the skewed Gaussian function in Equation(3.22) is used to fit the signal shape and background shape. For the signal, the skewed Gaussian function can describe the data better than a general Gaussian function because the shape is asymmetric with respect to the mass mean due to non-linearity on the reconstruction of energy, opening angle and $Z_{\gamma\gamma}$. For the background, using the skewed Gaussian function makes the fitting result more robust than using a polynomial function. The initial values and the limits for the parameters are easy to control since they have straight forward physical meaning. The data simulation comparisons are good for lower energy π^0, as is shown in the last section. But it is not always good, especially for high energy π^0, the parameters of the shape are allowed to

vary 10-20% during the fitting. Figure(3.27) shows an example of fitting the pion mass distribution, where the gray area is signal region and shaded areas is sideband region.

$$
\begin{aligned}
f(x) &= \frac{2}{\omega}\phi\left(\frac{x-\xi}{\omega}\right)\Phi\left(\alpha\left(\frac{x-\xi}{\omega}\right)\right) \\
\phi(x) &= \frac{1}{\sqrt{2\pi}}e^{-\frac{x^2}{2}} \\
\Phi(x) &= \int_{-\infty}^{x}\phi(t)dt = \frac{1}{2}\left[1+\mathrm{erf}\left(\frac{x}{\sqrt{2}}\right)\right]
\end{aligned}
\tag{3.22}
$$

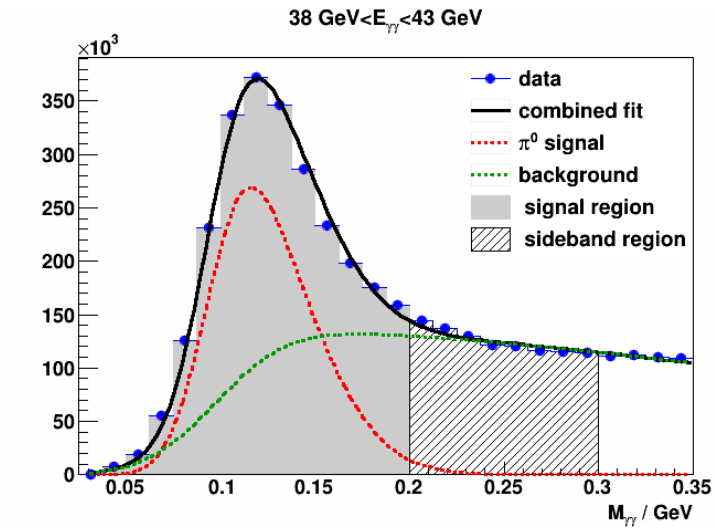

Figure 3.27: Example of fitting the pion mass of the energy between 38 to 43 GeV.

After the fitting, the yield of signal and background can be obtained by the integration of the signal and background function over the mass region. They are used to calculate the fractions in Equation(3.21). With the raw asymmetries and the fractions, one can get the asymmetry of the π^0 and background by simply solving Equation(3.21).

3.8.3 Jet Transverse Single Spin Asymmetry

The TSSA for jet can be calculated using the method just mentioned. Only the object is the jet instead of the π^0. Therefore no background subtraction is needed. Note that as a forward detector, there is no tracker coverage, it is possible that there are very few FMS points in the detector. In that case, even one or two FMS points can be reconstructed as a jet event. In this analysis, there is

no multiplicity cut on the FMS points. Those events are kept in the jet TSSA calculation.

3.8.4 Collins Asymmetry

The Collins asymmetry is the azimuthal angle dependence of the hadron with respect to the quark spin within a jet in the polarized proton-proton collision. It is similar to the TSSA which is the azimuthal angle dependence with respect to the proton spin. Equation(3.19) can be rewritten as Equation(3.23). ϕ_C, the Collins angle, can be considered as the azimuthal angle related to the quark spin. The change of the trigonometric function is due to the change of the zero point relative to the spin direction of the angle. Since the form of the two function remains mostly the same, the derivation of the cross-ratio method still holds. So the Collins asymmetry can be written as Equation(3.24).

$$\begin{aligned} N^{\uparrow}(\phi_c) &= \epsilon\mathcal{L}^{\uparrow}\sigma^{\uparrow} \\ &= \epsilon\mathcal{L}^{\uparrow}\left(1 + pol * A_{UT}\sin\phi_c\right)\ \sigma \end{aligned} \tag{3.23}$$

$$pol \cdot A_{UT}\sin\phi_c = \frac{\sqrt{N^{\uparrow}(\phi_c)N^{\downarrow}(\phi_c+\pi)} - \sqrt{N^{\downarrow}(\phi_c)N^{\uparrow}(\phi_c+\pi)}}{\sqrt{N^{\uparrow}(\phi_c)N^{\downarrow}(\phi_c+\pi)} + \sqrt{N^{\downarrow}(\phi_c)N^{\uparrow}(\phi_c+\pi)}} \tag{3.24}$$

The Collins angle is defined as $\phi_C = \phi_S - \phi_H$[33]. ϕ_S is the angle between the upward spin direction of the polarized proton and the jet-beam plane which is determined by the beam momentum and the jet momentum. ϕ_S ranges from 0 to 2π. ϕ_H is the angle between the jet-beam plane and the jet-pion plane which is determined by the π^0 momentum and the jet momentum. It also ranges from 0 to 2π. So ϕ_C should range from -2π to 2π. In this analysis, it was limited from $-\pi$ to π. The ϕ_S and ϕ_H is illustrated in Figure(3.28).

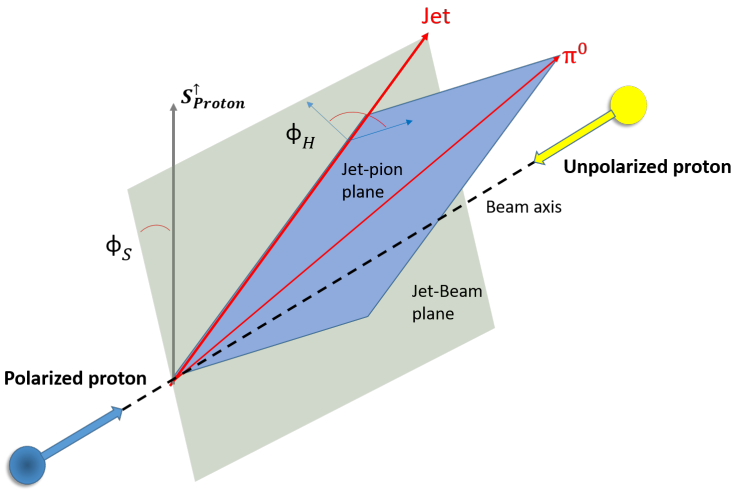

Figure 3.28: Definition in Collins asymmetry.

Chapter 4 Results and their Discussion

In this chapter, the results for the TSSA and Collins asymmetry will be shown and discussed. The estimation of the systematic uncertainties will be presented first.

4.1 Systematic Uncertainty

Since there are two observables presented in this thesis, their systematic uncertainties should be estimated independently. But there are some shared contributions in both estimations, for example, the uncertainty of the π^0 energy, so a large portion of the systematic uncertainty estimation is the same for both observables. It can be expected that the systematic uncertainty for the Collins asymmetry is more complicated since it involves the part for the jets.

4.1.1 Systematic Uncertainty for TSSA

4.1.1.1 Energy Scale Uncertainty

The TSSA result is reported as function of x_F, which equals $2p_L/\sqrt{s}$ with p_L being the longitudinal momentum. It approximately equals to the energy ratio of the π^0 over the incident proton beam as in Equation(4.1). The Collins asymmetry result is reported as function of z_{em} which is the energy ratio of the π^0 over the correlated electromagnetic jet, see Equation(4.1). Thus both energy uncertainties for the π^0 and the jet need to be estimated.

$$\begin{aligned} x_F &\approx E_{\pi^0}/E_{Proton} \\ z_{em} &= E_{\pi^0}/E_{jet} \end{aligned} \tag{4.1}$$

The π^0 and jet are composite objects made of the FMS points. Therefore their energy uncertainties come from the FMS point energy uncertainty, which can be divided into three parts as Equation(4.2). Each of them will be discussed below.

$$\Gamma\sigma_E = \sqrt{\sigma^2_{calibration} + \sigma^2_{correctioin} + \sigma^2_{radiation-damage}} \tag{4.2}$$

1. Calibration Uncertainty

   Since the calibration is done in the way of setting the π^0 mass to the right value, if the gains all fluctuate around its real value, from the point of view of the whole detector, the overall gain is not biased. The fluctuation only smears the energy distribution, but not altering the average of the gain. Only when the gains is biased to a direction for some reason, the energy uncertainty due to the calibration needs to be considered. As it is mentioned before, the FMS is calibrated by fixing the π^0 invariant mass. So in this way, the gains of all the channels are correlated. Supposed the gain of one channel is overestimated, to maintain the π^0 invariant mass, the gains of some neighboring channels have to be underestimated. These underestimated channels would caused the gains of some other channels overestimated. In such way of calibration, the overall gains of all the channels should be unbiased. The only places could introduce a bias are the reconstruction of the π^0 mass and the extraction of the π^0 mass mean. The invariant mass of π^0 is calculated by the energy of the FMS point and the distance of the two FMS points. For single-photon-type cluster which is used in the calibration, the reconstructed positions of the FMS points are accurate, thus the distance between them are also accurate. The energies are variables that need to be calibrated. So the only place that could introduce a bias is the extraction of the mass mean. Since the π^0 mass spectrum has certain amount of background, it needs a fit to extract the signal. Inappropriate background shape would cause the shift of the signal in the fitting. Therefore, the mass mean extracted from different background shape can be used to understand the energy uncertainty brought by the calibration.

   Figure(4.1) shows two cases of fitting result of π^0 which is made of two single-photon-type cluster, the left one is using the skewed Gaussian function with its background shape extracted from the simulation. The right one is using the 3-order polynomial function as background and assign all the parameters as free. The former one is considered to be the correct one, and the latter is considered similar in the calibration. The different mass mean extracted from each fitting can be assigned as the energy uncertainty brought by the calibration. Since in Run-11, the background is the highest,

such difference would be the largest. And the statistics is mainly from the small cell. So it is the only place that needs to be looked upon. The result shows that mass in the left figure in Figure(4.1) is 138.5 MeV while in the right figure is 133.8MeV. Thus the mass difference and the energy uncertainty brought by the calibration is 3.5%. In Run-15, the same comparison is done for the π^0 whose energy is 30GeV. The uncertainty is smaller due to the lower background, which is 2.5% for the large cell and 1% for the small cell.

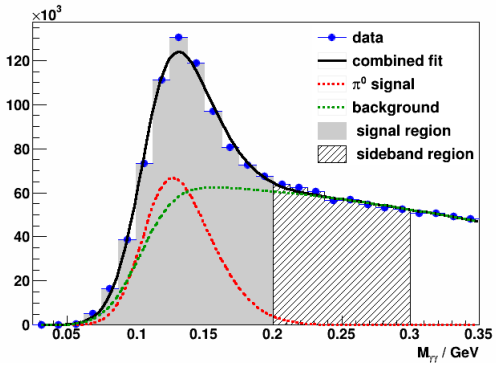

(a)

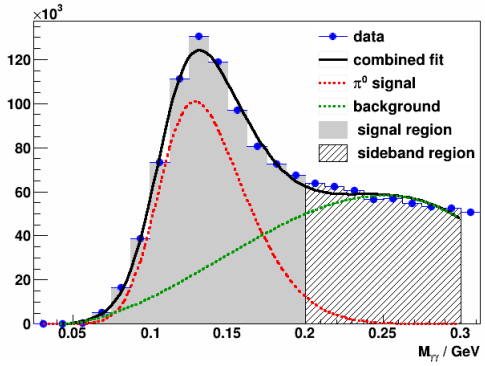

(b)

Figure 4.1: Comparison of different fitting result of the π^0 mass at 40 GeV for Run-11. Left panel is using the skewed Gaussian function with its background shape extracted from the simulation. The right panel is using the 3-order polynomial function as background and assign all the parameters as free.

2. Energy correction uncertainty

   Next, the uncertainty of the energy correction function is reviewed. The discussion in Section(3.5.2) shows there are two ways to get this correction. Both ways are consistent with each other. The one used in this analysis is

based on the attenuation model in simulation whose precision could suffer from the accuracy of the parameterization. In the other method, the precision of the Run-15 results which use the η mass could be impacted by different factors, like the calibration quality, the detector status in Run-15, and the η meson signal quality. It is critical to apply uncertainty to this energy correction. Since these two methods are developed independently and based on data from different years the difference between the two correction functions can be used to estimate the systematic uncertainty. The comparison shows the systematic uncertainty is less than 1.5% between 10-70 GeV.

3. Uncertainty due to Radiation Damage

   The radiation damage has been discussed in Section(2.3). It certainly will introduce some systematic uncertainty to the FMS point energy. The LED system is used to quantify this uncertainty.

   Before Run-15, some Zenner diodes caused some erratic behavior, which resulted in the PMT gains jumping around randomly within minutes. The LED system was installed to solve this problem. For every second, a LED light pulse with constant energy is directed into a tree of fiber optic cables that are connected to individual cells [76]. Observing the changes in the ADC value, which reflect the gain changes in the PMTs can help finding a correction factor to compensate these changes. In Run-15 and after, those problematic PMTs were replaced, the LED system now can be used to observe the long term gain changes caused by radiation damage. This information can be used to estimate the radiation damage and quantify the resulting energy uncertainty. It is noted that the fluctuation of the short term gain change is larger than the slow-changing one due to the radiation damage. So this method only works after the PMT problem was fixed.

   An effort to parameterize the radiation damage was done for Run-15 [76]. According to this study, the average gain change was observed to be 0.5% degradation per day for the large cells and 1.5% degradation per day for the small cells. The radiation damage of a tower is measured by the radiation absorbed by it. It is assumed that the radiation absorption rate is linear, like Equation(4.3) where $R(t)$ is the amount of the radiation a tower has absorbed. Solving this differential equation will get to Equation(4.4). The parameter C and the boundary condition $R(\infty)$, $R(0)$ are obtained from the

degradation rate and a GEANT simulation for photon tracking, for details see reference [76]. The simulation can also reproduce the pseudorapidity dependence of the radiation damage, see Equation(4.5). The parameters in Equation(4.4) are shown in Table(4.1). The energy change due to the radiation damage can be represented by the amount of radiation absorbed by the tower. The energy change over the data taking period is assigned as the uncertainty due to the radiation damage, as shown in Equation(4.6), where t is the time of the data taking in the units of day. Figure(4.2) shows the energy reduction due to radiation damage over time for the small cells, at pseudorapidity 3.5.

$$\frac{\mathrm{d}R(t)}{\mathrm{d}t} = C(R(\infty) - R(t)) \tag{4.3}$$

$$R(t) = R_{\infty} - (R(\infty) - R(0) * \exp^{-\lambda * t} \tag{4.4}$$

$$\lambda(\eta) = \lambda_0 * \exp^{(-h_0 + h_1 \eta)} \tag{4.5}$$

Table 4.1: Parameters for the radiation damage model.

Cell type	R_{∞}	R_0	$\lambda_0[day^-1]$	h_0	h_1
Large	4.46	1.0	0.0028	7.37	2.38
Small	3.44	1.0	0.0022	7.44	1.91

$$\frac{\sigma_{radiation}}{E(0)} = \frac{E(t) - E(0)}{E(0)} = \frac{R(t) - R(0)}{R(\infty) - R(0)}\Gamma \tag{4.6}$$

Naturally, the part of the FMS that suffers most of the radiation damage is at the high pseudorapidity range. The Pseudorapidity of 2.9/3.5 for large/small cells is used in the uncertainty estimation. The raw days in Run-11 are 20 (Day79-98), while it is 16 (Day66-93) in Run-15. The calibration done in Run-11 takes all the days but the calibration in Run-15 only takes several days for a segments. That means in Run-15 the number of days used in the estimation of energy uncertainty due to radiation damage is from the longest segment,which is five. The radiation damage research is based on the Run-15 gain change rate, which varies with the beam energy and luminosity. So for Run-11, the radiation damage in one day could be different from that in Run-15. The integral luminosity for one day in Run-15

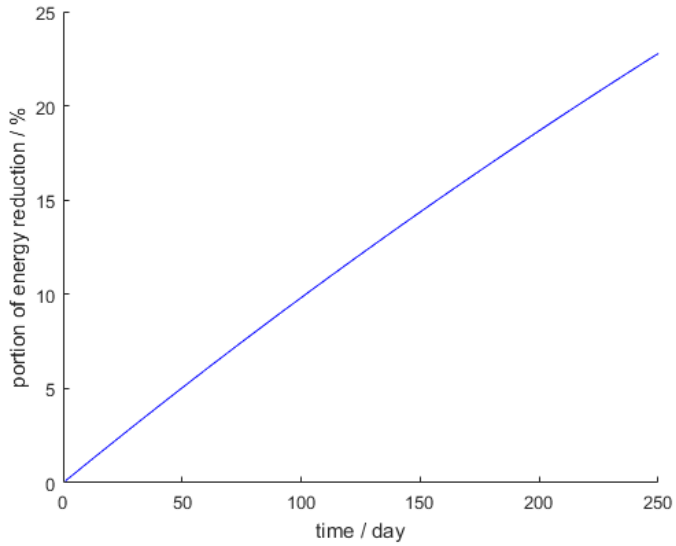

Figure 4.2: Energy reduction due to radiation damage for the small cells over time, at pseudorapidity=3.5.

is about 2.4 $pb^{-}1$, while it is 0.9 $pb^{-}1$ for Run-11. The collision energy for Run-15 is 2.5 times lower than Run-11. Assuming the cross-section is approximately linear with collision energy, then the radiation damage per day in Run-11 should be approximately the same to Run-15. The calculation shows, the uncertainty is 2.25%E/1.30%E for small/large cells in Run-11, and 0.5%E/0.2%E for small/large cells in Run-15. The uncertainty of the small cells, which is larger, is taken as the final uncertainty.

4. Uncertainty of the π^0 energy and x_F

   The π^0 consists of two photons. According to the error propagation, the uncertainty of the π^0 energy can be written as Equation(4.7). All the energy uncertainties discussed above are expressed as being linear to the photon energy, so the raw uncertainty of a photon is also linear to the photon energy with the coefficient R in Equation(4.7). It is easy to obtain a result for Run-11 $R = 4.42\%$, while in Run-15 $R = 2.95\%$, see Table(4.2). The upper limit for the sum of the quadratic term of the photon energy can be estimated with a an inequality, see Inequality (4.8). The Feynman-x x_F is the π^0 energy over the proton energy in the collision, which is 250 GeV in Run-11 and 100 GeV in Run-15. Its uncertainty is related to the energy uncertainty of the π^0. The result is shown in Table(4.3).

$$(\sigma_{E_\pi})^2 = \Sigma_{i=1,2}(\sigma_{E_i})^2 = \Sigma_{i=1,2}(R * E_i)^2 \tag{4.7}$$

$$(\sigma_{E_\pi})^2 < R^2 * {E_\pi}^2 \tag{4.8}$$

Table 4.2: Summary of photon energy uncertainty in Run-11 and Run-15.

Data	Calibration uncertainty	Energy Correction uncertainty	Radiation Damage uncertainty	Total uncertainty(R)
Run-11	3.5%E	1.50%E	2.25%E	4.42%E
Run-15	2.5%E	1.50%E	0.50%E	2.95%E

Table 4.3: Uncertainty of x_F for Run-11 and Run-15.

Energy bin	Energy mean in Run-11 (GeV)	x_F in Run-11	Uncertainty	Energy mean in Run-15 (GeV)	x_F in Run-15	Uncertainty
18-23				20.64	0.206	0.006
23-28				25.25	0.253	0.007
23-28				30.16	0.302	0.009
33-38				35.26	0.353	0.010
38-43	40.44	0.162	0.007	40.33	0.403	0.012
43-48	45.43	0.182	0.008	45.36	0.454	0.013
48-53	50.41	0.202	0.009	50.34	0.503	0.015
53-58	55.36	0.221	0.010	55.27	0.553	0.016
58-65	61.2	0.245	0.011	60.97	0.610	0.018
65-75	69.35	0.277	0.0124			
75-90	81.06	0.324	0.014			

4.1.1.2 Signal/Background Fraction Uncertainty

In calculating the transverse single spin asymmetry, the two fractions of $f_{\mathrm{sig}_{sig}}$ and $f_{\mathrm{sig}_{sb}}$ in Equation(4.9) can be obtained by fitting the π^0 mass distribution. The uncertainty of these fractions would propagate to the asymmetry. The result of signal and background asymmetries can be written as Equation(4.10). Equation(4.11) shows the error propagation of the systematic uncertainty of the fractions.

The uncertainty of the fractions in the fit is related to the eight fit parameters. The basic idea of getting the uncertainty is to introduce a Gaussian disturbance whose magnitudes are the standard error of the parameters into each of the fitting parameters and see how the fit result would change. The eight parameters are obviously correlated, so their covariances have to be considered. The most effective way to solve this is through a toy Monte Carlo simulation. The covariance matrix of the parameters can be obtained from the fit results then decomposed into the multiplication of one lower triangular matrix U and its Hermitian matrix by Cholesky decomposition like in Equation(4.12). In the toy Monte Carlo simulation, a set of random numbers following the Gaussian distribution is generated for each parameter and form a vector, which represents the initial disturbance input. Multiplying U with this vector will give the correlated disturbance vector whose component represents the disturbance for each parameter. Applying them to the original fit result will generate a new fit result with the added disturbance. This can be used to calculate the new fractions.

$$\begin{aligned} A_N^{\mathrm{raw}_{sig}} &= f_{\mathrm{sig}_{sig}} * A_N^{\pi^0} + (1 - f_{\mathrm{sig}_{sig}}) * A_N^{bkg} \\ A_N^{\mathrm{raw}_{sb}} &= f_{\mathrm{sig}_{sb}} * A_N^{\pi^0} + (1 - f_{sig_{sb}}) * A_N^{bkg} \end{aligned} \tag{4.9}$$

$$\begin{aligned} A_N^{\pi^0} =& \frac{(1 - f_{\mathrm{sig}_{sb}}) * A_N^{\mathrm{raw}_{sig}} - (1 - f_{\mathrm{sig}_{sig}}) * A_N^{\mathrm{raw}_{sb}}}{f_{\mathrm{sig}_{sig}} - f_{\mathrm{sig}_{sb}}} \\ A_N^{bkg} =& \frac{f_{\mathrm{sig}_{sb}} * A_N^{\mathrm{raw}_{sig}} - f_{\mathrm{sig}_{sig}} * A_N^{\mathrm{raw}_{sb}}}{f_{\mathrm{sig}_{sb}} - f_{\mathrm{sig}_{sig}}} \end{aligned} \tag{4.10}$$

$$\begin{aligned} (\delta A_N^{\pi^0})^2 =& \frac{\left((1 - f_{\mathrm{sig}_{sb}}) * (A_N^{\mathrm{raw}_{sig}} - A_N^{\mathrm{raw}_{sb}})\right)^2}{(f_{\mathrm{sig}_{sig}} - f_{\mathrm{sig}_{sb}})^4} (\delta f_{\mathrm{sig}_{sig}})^2 + \\ & \frac{\left((1 - f_{\mathrm{sig}_{sig}}) * (A_N^{\mathrm{raw}_{sig}} - A_N^{\mathrm{raw}_{sb}})\right)^2}{(f_{\mathrm{sig}_{sig}} - f_{\mathrm{sig}_{sb}})^4} (\delta f_{\mathrm{sig}_{sb}})^2 \\ (\delta A_N^{bkg})^2 =& \frac{\left((f_{\mathrm{sig}_{sb}}) * (A_N^{\mathrm{raw}_{sig}} - A_N^{\mathrm{raw}_{sb}})\right)^2}{(f_{\mathrm{sig}_{sig}} - f_{\mathrm{sig}_{sb}})^4} (\delta f_{\mathrm{sig}_{sig}})^2 + \\ & \frac{\left((f_{\mathrm{sig}_{sig}}) * (A_N^{\mathrm{raw}_{sig}} - A_N^{\mathrm{raw}_{sb}})\right)^2}{(f_{\mathrm{sig}_{sig}} - f_{\mathrm{sig}_{sb}})^4} (\delta f_{\mathrm{sig}_{sb}})^2 \end{aligned} \tag{4.11}$$

$$M = UU^T, M : Covariance\ matrix \tag{4.12}$$

The new fractions would deviate from the original one. Repeating this procedure will generate a Gaussian distribution whose variance will be assigned as the uncertainty of the fraction. Figure(4.3) shows an example of the signal fraction in the signal region distribution with the added disturbance from the toy Monte Carlo simulation. Its uncertainty can be obtained by fitting the distribution with a Gaussian function. The uncertainties of the fraction for Run-11 and Run-15 are listed in Table(4.4) and Table(4.5). The uncertainties propagating to the asymmetry is negligible based on these numbers.

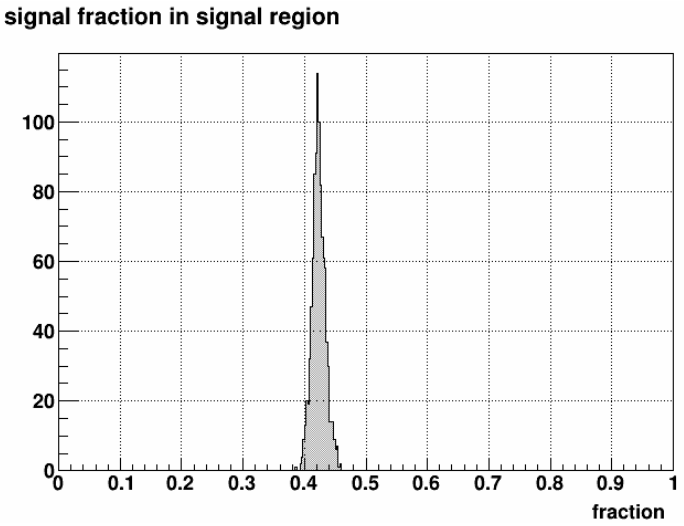

Figure 4.3: Example of the signal fraction in the signal region distribution under the disturbance in the toy Monte Carlo simulation.

Table 4.4: Uncertainty of the fraction for Run-11

Energy bin	$f_{\mathrm{sig}_{sig}}$	$\Delta f_{\mathrm{sig}_{sig}}$	$f_{\mathrm{sig}_{bkg}}$	$\Delta f_{\mathrm{sig}_{bkg}}$
38-43	0.568	0.003	0.017	0.000
43-48	0.586	0.000	0.019	0.000
48-53	0.621	0.001	0.025	0.000
53-58	0.704	0.000	0.049	0.000
58-65	0.734	0.000	0.103	0.001
65-75	0.731	0.001	0.116	0.001
75-90	0.758	0.013	0.185	0.003

Table 4.5: Uncertainty of the fraction for Run-15

Energy bin	$f_{\mathrm{sig}_{sig}}$	$\Delta f_{\mathrm{sig}_{sig}}$	$f_{\mathrm{sig}_{bkg}}$	$\Delta f_{\mathrm{sig}_{bkg}}$
18-23	0.660	0.000	0.044	0.000
23-28	0.786	0.000	0.045	0.000
28-33	0.819	0.000	0.082	0.000
33-38	0.846	0.000	0.150	0.000
38-43	0.883	0.000	0.378	0.001
43-48	0.893	0.000	0.459	0.001
48-53	0.895	0.002	0.525	0.002
53-58	0.902	0.003	0.596	0.018
58-65	0.895	0.001	0.674	0.002

4.1.2 Systematic Uncertainty for the Collins Asymmetry

The photon energy uncertainties discussed above for the TSSA are also valid for the Collins asymmetry analysis. Two sorts of additional uncertainties will be discussed below.

4.1.2.1 Jet Energy Correction and the Uncertainty on z_{em}

The jet energy can be biased by the detector effects. As in other STAR jet analysis, the standard way to correct this bias is to compare the jet energy at detector level and particle level event by event in simulation. The particle level jet refers to the jet reconstructed from particles from the event generator final particle list. In this analysis, since it is an electromagnetic jet reconstructed in the FMS, the particle jet would be reconstructed from photons and electrons only. The detector level jet refers to the jet that is reconstructed from the FMS points, which includes the detector effects. Since the Collins asymmetry result is reported as function of z_{em}, which equals to the π^0 energy divided by the jet energy, the z_{em} value, similar to the jet energy, needs to be corrected. The method is the same that one compares the z_{em} on detector level and on particle level. The detector level z_{em} is calculated by the reconstructed π^0 and its correlated detector jet. The particle level z_{em} is calculated by the matched π^0 and the matched particle jet. The matching scheme has been discussed in Section(3.7.2). The difference is used as the correction for a specific z_{em} bin. This correction is applied to Run-11 and Run-15. The results are shown in Table(4.6) and Table(4.7) .

Table 4.6: Correction and uncertainty of different z_{em} bins for the Collins asymmetry in Run-11

zbin	z_{rec}	Corrected z_{em}	z uncertainty Run-11
0.3-0.4	0.344	0.379	0.024
0.4-0.5	0.449	0.500	0.031
0.5-0.6	0.550	0.610	0.038
0.6-0.7	0.650	0.703	0.044
0.7-0.8	0.750	0.782	0.049
0.8-0.9	0.850	0.846	0.053

Table 4.7: Correction and uncertainty of different z_{em} bins for the Collins asymmetry in Run-15

zbin	z_{rec}	Corrected z_{em}	z uncertainty Run-15
0.3-0.4	0.345	0.356	0.015
0.4-0.5	0.449	0.466	0.019
0.5-0.6	0.550	0.571	0.023
0.6-0.7	0.649	0.665	0.027
0.7-0.8	0.749	0.755	0.031
0.8-0.9	0.846	0.832	0.034

The uncertainty of z_{em} is related to the uncertainty of the π^0 energy and jet energy. The former one has been discussed in Section(4.1.1.1). The jet energy uncertainty can be estimated in the same way. The jet is composed of several FMS points. The energy uncertainty of the jet is related to the number of FMS points and their energy, as in Equation(4.13) where the coefficient R is shown in Table(4.2). Similarly, the upper limit of the uncertainty can be estimated with Inequality (4.14).

The upper limit of the uncertainty of z_{em} is calculated using Inequality (4.15). Since the π^0 is within the jet, the π^0 energy is positively correlated with the jet energy. According to the error propagation, σ_Z equals the right part of the inequality and subtracting the positive covariance term. In this inequality, the uncertainty of the π^0 energy and jet energy have been discussed. The final result is shown in Table(4.6) and Table(4.7).

$$\sigma_{jetE}{}^2 = \Sigma\sigma_{E_i}{}^2 = \Sigma((R * E_i)^2\Gamma \tag{4.13}$$

$$\sigma_{jetE}{}^2 < R^2 * E_{jet}^2 \tag{4.14}$$

$$\begin{aligned}(\frac{\sigma_Z}{Z})^2 &< (\frac{\sigma_{E_\pi}}{E_\pi})^2 + (\frac{\sigma_{E_{jet}}}{E_{jet}})^2 \\ &< 2R^2\end{aligned} \tag{4.15}$$

4.1.2.2 ϕ_C Resolution

Due to the limitations of the detector resolution, the resolution of the angle, ϕ_C, which is used in calculating the Collins asymmetry is limited by the resolution of the FMS point position and the EM-jet position. A Monte Carlo simulation is used to estimate this uncertainty. In the simulation, the reconstructed π^0s can be matched with their sources in the PYTHIA record. The same is done for the reconstructed jets. The matching scheme has been discussed in Section(3.7.2). After the geometric match, comparing the ϕ_C angle calculated on detector level and generator level will give the angle smearing by the detector. The $\Delta\phi_C$ angle is shown in Figure(4.4) and fitted with three Gaussian functions.

The Collins asymmetry is expressed as a sinusoidal modulation with respect to the ϕ_C angle. Supposing that there is a disturbance term $\Delta\phi_C$ added

to the initial ϕ_{C_0} angle in the sinusoidal function, it can be written as Equation(4.16) where A is the asymmetry and the trivial constant term is not shown. Note that the disturbance term is averaged over the measurement, and the term $Acos(\phi_{C0})\langle sin(\Delta\phi_C)\rangle$ vanishes due to its odd nature. So the asymmetries measured in the data can be expressed as the physical asymmetry times the residual disturbance term $\langle cos(\Delta\phi_C)\rangle$, as shown in Equation(4.17). Therefore $A_{ture} = A_{measure}/\langle cos(\Delta\phi_C)\rangle$. It is obvious that the smearing of the ϕ_C angle, which is caused by the disturbance could reduce the measured asymmetries. The average of $cos(\Delta\phi_C)$ with $\Delta\phi_C$ following a certain distribution $f(x)$ can be calculated by Equation(4.18).

Using this result, the asymmetry reduction for each z_{em} bin can be calculated and the results are shown in Table(4.8).

$$Asin(\phi_{C0}+\Delta\phi_C) = Asin(\phi_{C0})cos(\Delta\phi_C) + Acos(\phi_{C0})sin(\Delta\phi_C) \tag{4.16}$$

$$Asin(\phi_C) = Asin(\phi_{C0})\langle cos(\Delta\phi_C)\rangle \tag{4.17}$$

$$\langle cos(\Delta\phi_C)\rangle = \int_{-\pi}^{\pi} cos(x)f(x)\mathrm{d}x \tag{4.18}$$

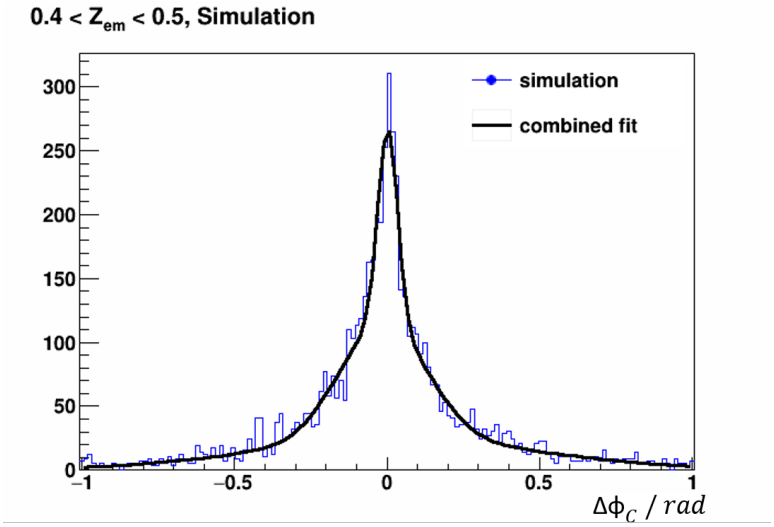

Figure 4.4: ϕ_C resolution in $0.4 < z_{em} < 0.5$.

4.1.3 Systematic uncertainty for the Jet TSSA

For the jet TSSA, the estimation of systematic uncertainty includes jet energy correction, and jet background correction. The jet energy correction and en-

Table 4.8: Correction due to the ϕ_C resolution for different z_{em} bins in the Collins asymmetry.

z_{em} bin	correction due to ϕ_C resolution
0.3-0.4	1.0%
0.4-0.5	1.1%
0.5-0.6	1.4%
0.6-0.7	2.1%
0.7-0.8	2.5%
0.8-0.9	3.9%

ergy uncertainty has been discussed in the systematic uncertainty for the Collins asymmetry. Here only shows the result in 4.9.

Table 4.9: Correction and uncertainty of the jet energy

Energy Bin	Corrected Energy in Run-11(GeV)	Uncertainty in Run-11(GeV)	Corrected Energy in Run-15(GeV)	Uncertainty in Run-15(GeV)
18-23			21.21	0.61
23-28			25.50	0.74
28-33	30.63	1.35	30.33	0.88
33-38	35.57	1.57	35.32	1.02
38-43	40.52	1.78	40.31	1.17
43-48	45.47	2.00	45.31	1.31
48-53	50.40	2.22	50.29	1.46
53-58	55.38	2.44	55.32	1.60
58-65	61.23	2.69	61.19	1.77
65-75	69.38	3.05		
75-90	81.05	3.57		
90-120	99.90	4.40		

Although there is no combinatoric background like in calculating the inclusive π^0 TSSA，it is found that there is some background of jet that needs to be dealt with. Figure(4.5) shows the high energy part of the jet energy distribution in Run-15. Since the beam energy in Run-15 is 100 GeV, the high energy jet events can not be physical. It could be from pile-up events. This kind of background events will decrease the TSSA for jet if they remains in the TSSA

calculation.

The effect from the background can be corrected if the background fraction in each jet energy bin is known, since the background asymmetry is assumed to be zero. In that case, Figure(4.5) shows the background shape is close to linear in very large energy range, which is 120 to 150 GeV. The signal can appear at larger than 100GeV due to the energy resolution. At this range, the signal should be small enough. The fitted result for the background in Figure(4.5) is $1742-10.82*Energy$. Using this function, it is found that the background fraction is significant after 65 GeV in Run-15, thus the highest energy bin is chosen as 58-65 GeV in Run15. The background fraction can be found in Table(4.10). The correction factor would be one minus background fraction. In Run11, since we are working at the energy range that is far away from the beam energy, the influence of the background is considered to be negligible.

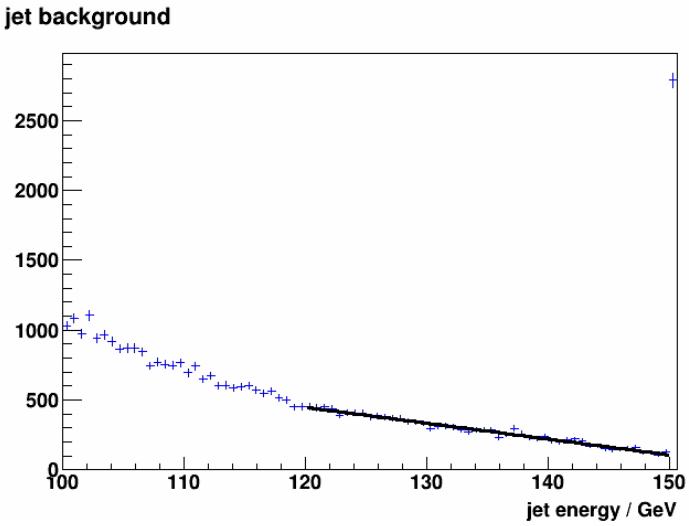

Figure 4.5: High energy part of jet energy distribution. The background is fitted with a linear function from 120 GeV to 150 GeV, where the background dominates.

The other correction is for the underlying events. The underlying event is a part of a jet but not from the parton fragmentation. It could be from secondary scattering or other processes. It puts additional energy to the jet, thus need to be subtracted. The method used for subtraction is called "off axis jet" estimation. For a reconstructed jet, it first fixes the axises two off axis jets at the same pseudorapidity of the reconstructed jet but at $\pm\pi/2$ relative to the azimuthal angle of the reconstructed jet. And then correlate the FMS points to each of the jet axises. The ΔR cut for the correlation is set to be

Table 4.10: Background fraction for each jet energy bin in Run-15

Energy Bin	Correction for asymmetry
18-23	0.014
23-28	0.007
28-33	0.006
33-38	0.006
38-43	0.008
43-48	0.012
48-53	0.018
53-58	0.027
58-65	0.045

$0.7(\Delta R = \sqrt{((\eta_{point} - \eta_{jet})^2 + (\phi_{point} - \phi_{jet})^2})$. These off cone axis jets are considered as underlying event background. With the assumption that the underlying events distribute randomly azimuthally, the energy of the correlated FMS points is considered from the underlying events. The underlying event Energy density can be calculated using $E/(\pi R^2)$. The energy needs to be subtracted equals to multiplicand of underlying event energy density and the jet area which is provided by the fastjet program[80]. The fastjet program uses a technique call ghost particle to calculate the jet area. It fills a bunch of very low energy particles beyond the edge of the detector to get the correct area for jets near the edge of the detector. The results of energy of the underlying even are shown in Figure(4.11).

4.1.4 Beam Polarization and its Uncertainty

Beam polarization and its uncertainty is used in all asymmetry calculations. As a habit, the beam polarization uncertainty is listed independently.

The beam polarization measurement is provided by the CNI group, which develops, maintains and operates the RHIC polarimeters. The results of polarization measurement can be found in these web pages[84][85]. The details of the measurements and calculations of the polarization can be found in reference [86][87]. The web pages provide the polarization at the start of each fill P_0 and the decay rate $\frac{dP}{dt}$ with the uncertainties. The average polarization of a run is calculated by Equation(4.19), where t_{run} is the time stamp at the center of the run. The average polarization of a fill is then summed up by the luminosity weighted P_{run} like Equation(4.20). Similarly, the overall polarization of the whole data

Table 4.11: Underlying event correction for jet energy in Run-11 and Run-15

Energy Bin	UE Energy in Run-11(GeV)	UE Energy in Run-15(GeV)
18-23	8.24	4.50
23-28	7.66	4.33
28-33	6.54	4.11
33-38	5.46	4.03
38-43	4.83	3.96
43-48	4.48	3.84
48-53	4.29	3.78
53-58	4.18	3.75
58-65	4.09	3.75
65-75	4.02	
75-90	3.95	
90-120	3.85	

sample is calculated by the weighted average polarization of each fill like Equation(4.21). The polarization of each fill is shown in Figure(4.6) and Figure(4.7).

$$P_{run} = P_0 + \frac{dP}{dt}(t_{run} - t_0) \tag{4.19}$$

$$P_{fill} = \frac{\Sigma_{run} L_{run} P_{run}}{\Sigma_{run} L_{run}} \tag{4.20}$$

$$P_{overall} = \frac{\Sigma_{run} L_{run} P_{run}}{\Sigma_{run} L_{run}} \tag{4.21}$$

The uncertainty of the polarization includes several parts as Equation(4.22), the scale uncertainty, fill-to-fill uncertainty and uncertainty from the profile correction procedure. The scale uncertainty comes directly from the polarimetry and the numbers are provided in the note. For example, in Run11 such uncertainty is 3.3%. The uncertainty from the profile correction procedure is due to the average process when measuring the polarization. It can be estimated as $2.2\%/\sqrt{M}$ where M is the number of fills that used in the analysis.

$$\sigma\left(P_{set}\right) = P_{set} \cdot \frac{\sigma(\text{ scale })}{P} \oplus \sigma(\text{ fill-to-fill scale }) \oplus P_{\text{set}} \cdot \frac{\sigma(\text{ profile })}{P} \tag{4.22}$$

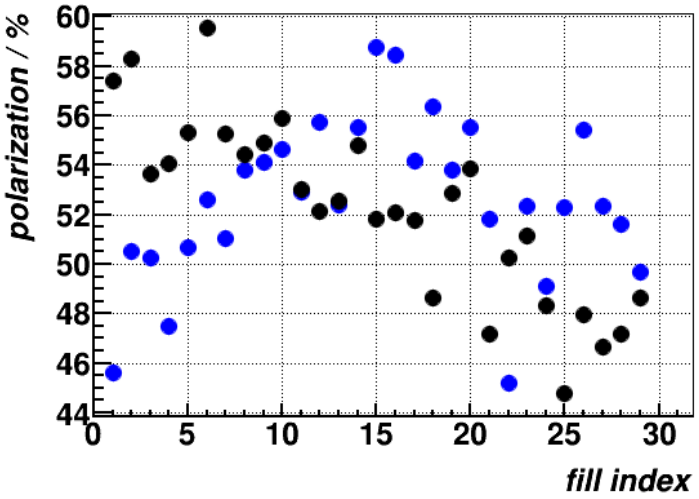

Figure 4.6: Fill by fill polarization of Run-11, blue/black points for blue/yellow beam.

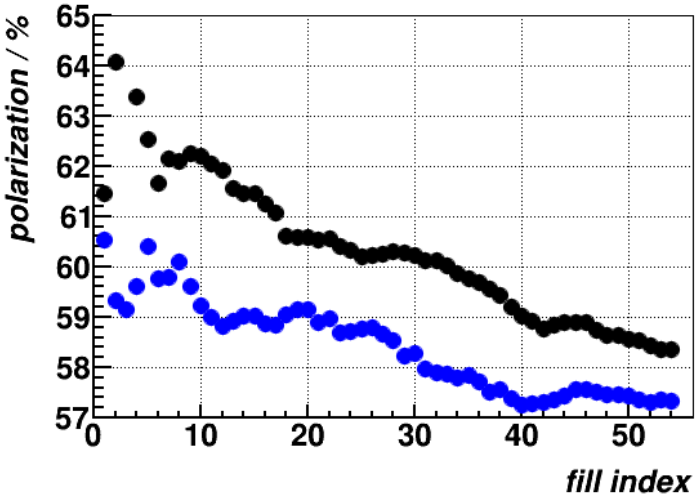

Figure 4.7: Fill by fill polarization of Run-15, blue/black points for blue/yellow beam.

The fill-to-fill scale uncertainty needs more calculations. It needs the polarization uncertainty for the dataset which is composed of the uncertainty of each fill, see Equation(4.24). The uncertainty of a fill is shown in Equation(4.23). According to the calculation of the polarization, the uncertainty is related to the uncertainty of P_0, $\frac{dP}{dt}$ and an additional term of the fill-to-fill uncertainty. This additional term is due to the sensitivity of the measurement of the energy scale of the nuclei in the pC polarimetry. They are usually small or negligible compared to the statistical uncertainties. By comparing the up- and down-stream pC polarimeter results, it shows the fill-to-fill uncertainty is 3.2%/0.9% for blue and yellow beam respectively in Run-11 and negligible in Run-15. The details can be found in reference [87]. Since a fill-to-fill uncertainty is already considered in each fill, it would be double counting when combining the overall polarization for the entire dataset. A correction factor of $\sqrt{1-\frac{M}{N}}$ is applied to the uncertainty of the dataset to compensate for the over-counting fill-to-fill uncertainty, see Equation(4.25). M is the number of fills analyzed and N is the number of fills used in the overall scale uncertainty study. For Run-11, M=29 and N=65. The final result of the polarization and its uncertainties in Run-11 and Run-15 is shown in Table(4.12).

$$\sigma^2_{P_{fill}} = \sigma^2_{P_0} + \sigma^2_{\frac{dP}{dt}} * (\frac{\Sigma_{run} t_{run} L_{run}}{\Sigma_{run} L_{run}} - t_0)^2 + (\frac{\sigma_{fill-to-fill}}{P})^2 * P^2_{fill} \tag{4.23}$$

$$\sigma^2_{P_{dataset}} = \frac{\Sigma_{fill} L^2_{fill} \sigma^2_{P_{fill}}}{(\Sigma_{fill} L_{fill})^2} \tag{4.24}$$

$$\sigma^2_{fill-to-fill-scale} = (1 - \frac{N}{M}) \sigma^2_{P_{dataset}} \tag{4.25}$$

Table 4.12: Result of polarization in Run-11 and Run-15

Beam	Polarization(%)	Uncertainty(%)	Uncertainty Ratio
Run-11			
Blue	52.36	1.77	3.4%
Yellow	50.14	1.70	3.4%
Run-15			
Blue	56.59	1.69	3.0%
Yellow	57.39	1.72	3.0%

4.1.5 Summary of Systematic Uncertainties

Here the summary of the discussion from the above sections is given. Table(4.13) shows the result of the uncertainties in both analyses.

4.2 Results and Discussion

The final results for the π^0 and jet's transverse single spin asymmetry and Collins asymmetry are presented in this section. In all plots, the statistical uncertainties are shown with error bars and the systematic uncertainties are shown as shaded error boxes.

4.2.1 Transverse Single Spin Asymmetry

The π^0 selection cuts are summarized here at the beginning. For the transverse single spin asymmetry A_N:

- $Pt > 2GeV$
- $2.7 < \eta < 4.0$
- $M_{\gamma\gamma} < 0.3GeV$
- $Z_{\gamma\gamma} < 0.7$

It has been discussed in Section(3.8) that the raw asymmetry, which is the combination of π^0 signal asymmetry and background asymmetry can be calculated using the cross-ratio method. With the fractions in Table(4.4), the TSSAs of π^0 signal and background can be calculated simultaneously using Equation(4.26). The A_N^{raw} for different mass regions is calculated fill by fill and averaged afterward. The fractions are considered unchanged for every fill.

$$\begin{aligned} A_N^{\text{raw}_{sig}} &= f_{\text{sig}_{sig}} * A_N^{\pi^0} + (1 - f_{\text{sig}_{sig}}) * A_N^{bkg} \\ A_N^{\text{raw}_{sb}} &= f_{\text{sig}_{sb}} * A_N^{\pi^0} + (1 - f_{sig_{sb}}) * A_N^{bkg} \end{aligned} \tag{4.26}$$

Manipulating the combination of spin patterns, one can get a data sample with polarized blue beam and unpolarized yellow beam or vice versa. Figure(4.8) shows the results of π^0 signal and background asymmetries in Run-11, in which the left panel is for the polarized blue beam and unpolarized yellow beam while

Table 4.13: Summary of systematic uncertainties for Run-11 and Run-15

Analysis	Uncertainties types					
	Photon energy	Jet energy correction	Fraction	ϕ_C resolution	Jet background	Beam polarization
π^0 TSSA	Table(4.4)	Table(4.2)	—	—	—	Table(4.12)
Collins asymmetry	—	Table(4.2)	Table(4.6)(4.7)	Table(4.8)	—	Table(4.12)
Jet TSSA	—	Table(4.2)	Table(4.9)	—	Table(4.10)	Table(4.12)

the right panel is for the polarized yellow beam and unpolarized blue beam. Figure(4.9) shows the results in Run-15 with different x_F ranges. The asymmetries are plotted as function of Feynman-x (x_F), which is calculated by the ratio of π^0 energy over the energy of the colliding proton. When the outgoing π^0 is at the forward direction of the polarized beam, the x_F is defined as positive, otherwise it is negative. In the left panels of Figure(4.8) and Figure(4.9), the π^0 is at the forward direction of the polarized beam (blue), which means the x_F is positive. Similarly, in the right panels of Figure(4.8) and Figure(4.9), the x_F is negative. For Run-11, the collision energy is 500 GeV while it is 200 GeV in Run-15. So for the same energy of π^0, the x_F range in Run-11 is lower than Run-15. Due to the limitation of the background level, quality of reconstruction and statistics, in Run-11, the π^0 energy range is from 38 to 90 GeV, while in Run-15, it is 18-65 GeV。

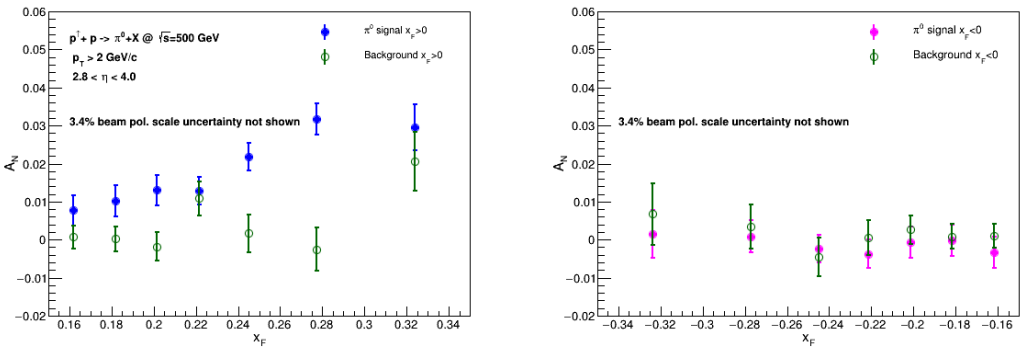

Figure 4.8: TSSA Results of π^0 signal and background for STAR Run-11 data. Left panel: for polarized blue beam, $x_F > 0$; Right panel: for polarized yellow beam, $x_F < 0$.

Large asymmetries for π^0 are observed at large positive x_F. The asymmetry increases with x_F. In Run-15, the x_F range is higher than that in Run-11, so the asymmetry is more significant in Run-15. For both year's data, the background asymmetries are consistent with zero within uncertainty, which means that the background subtraction is effective. For both Run-11 and Run-15, the asymmetries for negative x_F are consistent with zero within uncertainty. It is as expected because the backward (relative to the polarized yellow beam) π^0 is considered to have weak correlation with the polarized proton in the yellow beam but have strong correlation with the unpolarized yellow beam. So it should reflect the property of the unpolarized proton beam.

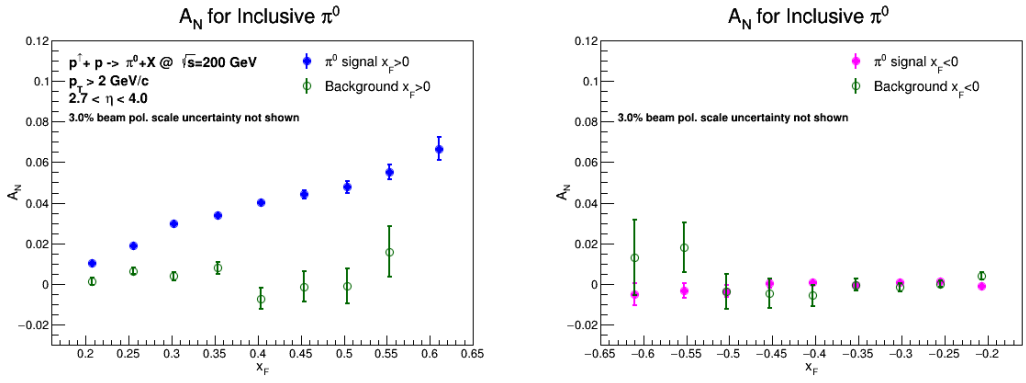

Figure 4.9: TSSA Results of π^0 signal and background for STAR Run-15 data. Left panel: for the polarized blue beam, $x_F > 0$; Right panel: for polarized yellow beam, $x_F < 0$.

Figure(4.10) shows the TSSA of the π^0 signal only. From Figure(4.10), the results of Run-11 and Run-15 are consistent, the trend of the asymmetries rising as x_F does not show significant differences between them, especially when one takes a look at the overlap region at x_F between 0.2 to 0.35.

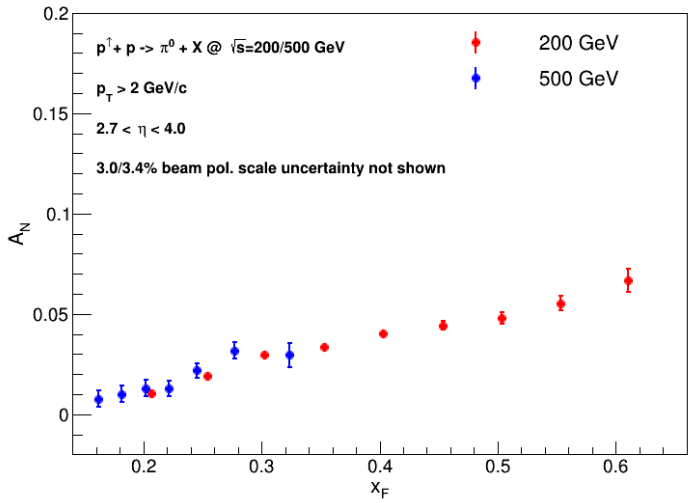

Figure 4.10: Combined results of the TSSA of only the π^0 signal at x_F in Run-11 and Run-15.

It has been shown that the TSSA for both years are consistent in the overlapped x_F region. It could be useful to check the traverse momentum dependence of the the TSSA in such x_F region which is 0.18 to 0.36. Figure(4.11) and Figure(4.12) shows the results for π^0 signal and background for STAR Run-11 and Run-15 data at x_F 0.18 to 0.36. Again, for the background, the asymmetries

are consistent with zero within uncertainty. The signal asymmetries at negative x_F are also consistent with zero within uncertainty for the same reason just discussed. For the signal at positive x_F, the 200 GeV TSSA result shows clear trend of the TSSA rising with traverse momentum. The 500 GeV result is consistent with the former one. But due to the limited statistics, the trend is not clear. The signal only result in Figure(4.13) shows more clear comparison.

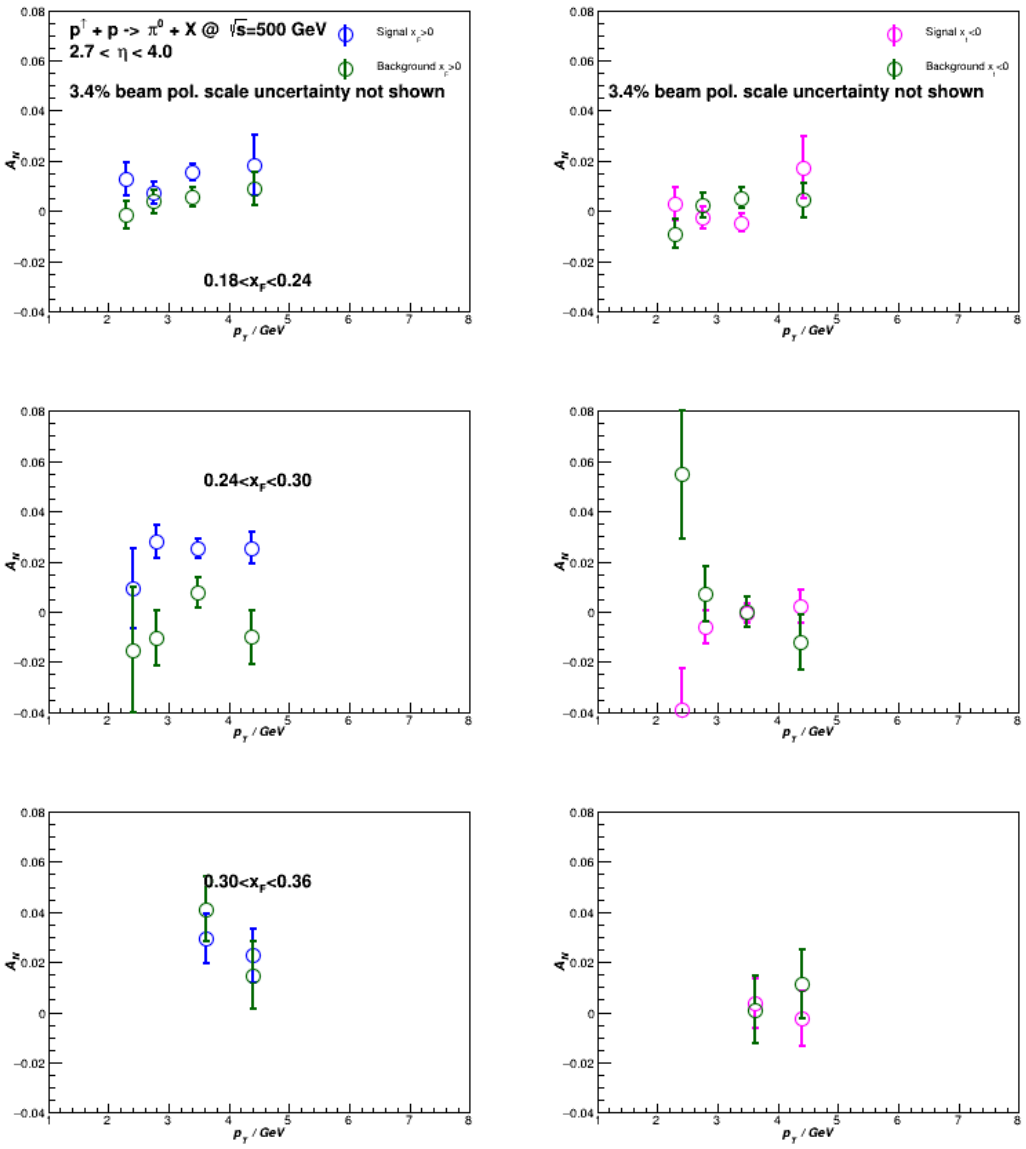

Figure 4.11: TSSA Results as function of Pt of π^0 signal and background for STAR Run-11 data at overlapped x_F region. Left panel: for polarized blue beam, $x_F > 0$; Right panel: for polarized yellow beam, $x_F < 0$.

Figure(4.14) shows the results of other proton-proton experiments, which

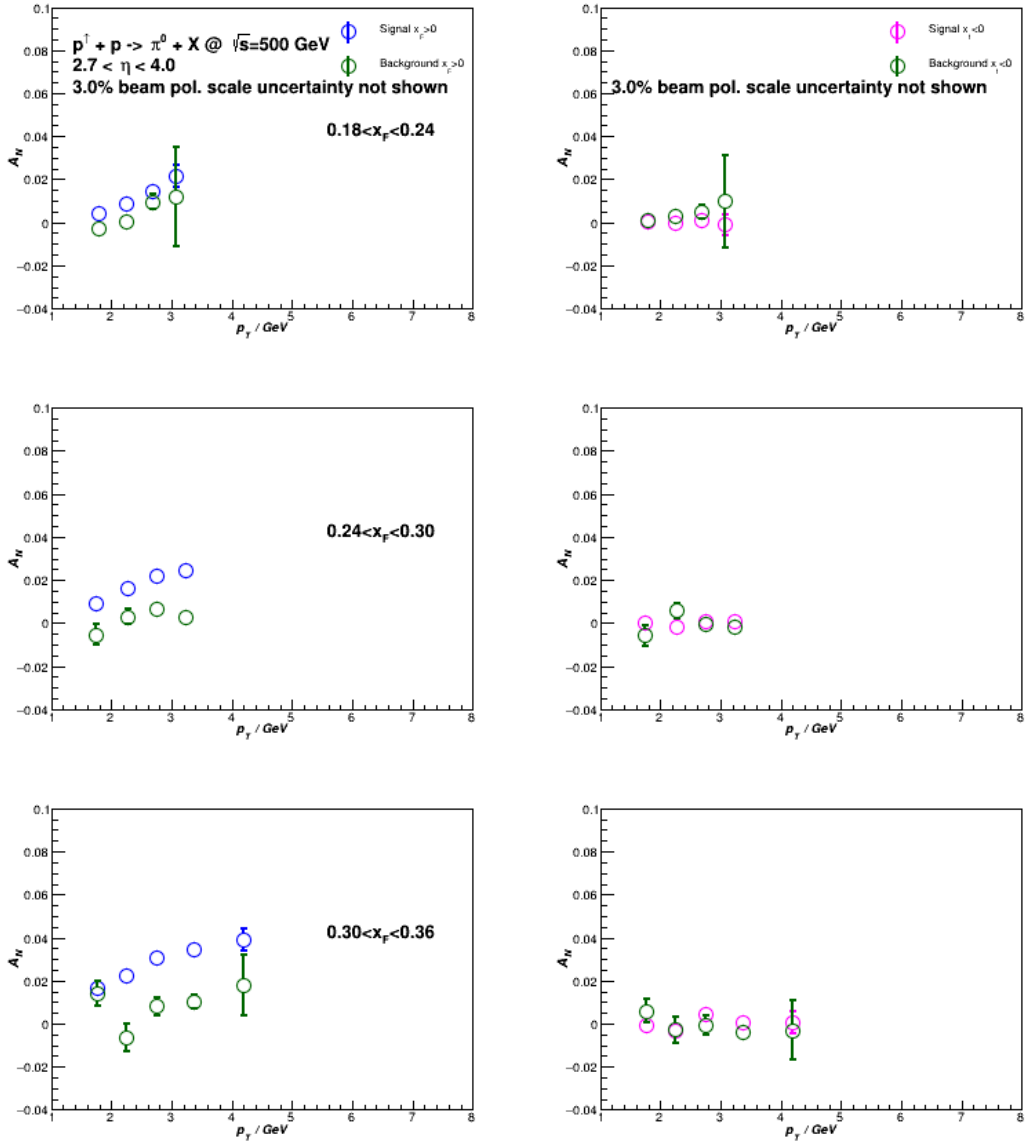

Figure 4.12: TSSA Results as function of Pt of π^0 signal and background for STAR Run-15 data at overlapped x_F region. Left panel: for the polarized blue beam, $x_F > 0$; Right panel: for polarized yellow beam, $x_F < 0$.

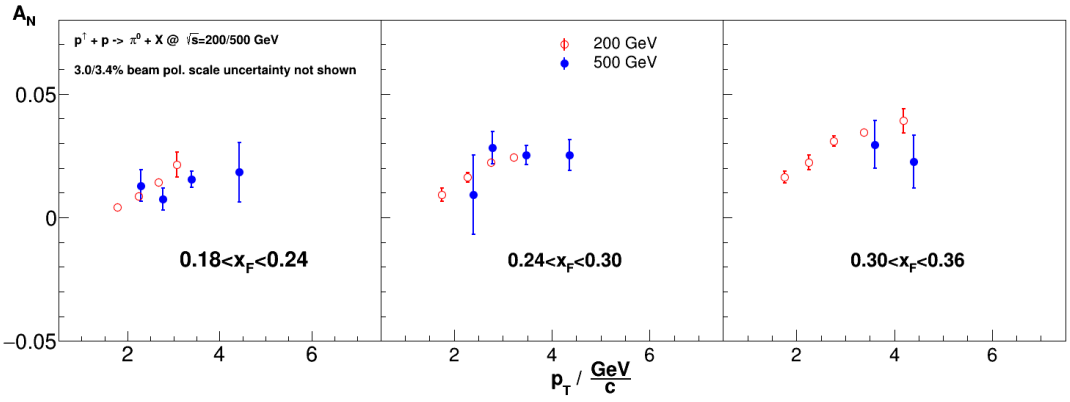

Figure 4.13: Combined results of the TSSA of only the π^0 signal at x_F in Run-11 and Run-15 at overlapped x_F region.

are mainly from STAR at forward pseudorapidity. It also includes the early E704 experiment[17] at Fermi National Accelerator Laboratory. The former STAR 200 GeV results[88] are shown in black and magenta markers in Figure(4.14), which was done using the FPD detector. The Run-15 result in this thesis with the same collision energy using the FMS covers a wider pseudorapidity range and has better statistics. Some bias could be seen from those two dataset in 200 GeV at low x_F. It could be due to different average transverse momentum. In this thesis the minimum transverse momentum is 2 GeV. In the previous measurement, the majority of the data points come from lower transverse momentum. As can be seen in the transverse momentum dependency discussed above, the asymmetries are lower in lower transverse momentum when in low x_F region. This could explain the difference of the previous STAR measurements. Other than that, the results from all the experiments are consistant in other x_F region. One important conclusion can be drawn from compared the result of different collision energy. The center-of-mass energies of these experiments range from 19.4 to 500 GeV. In such energy range, the asymmetries from different experiments are following the same trend with x_F, which suggest weak scale dependence. This means that the physical mechanism has very weak energy scale dependence. The result in Run-11 is the first measurement in 500 GeV which pushes the above conclusion to even high energy range.

In searching the origin of the transverse single spin asymmetry, one particularly interesting way is through the topological dependence of π^0 TSSAs. It refers to dividing the π^0 sample into two groups based on the π^0 event struc-

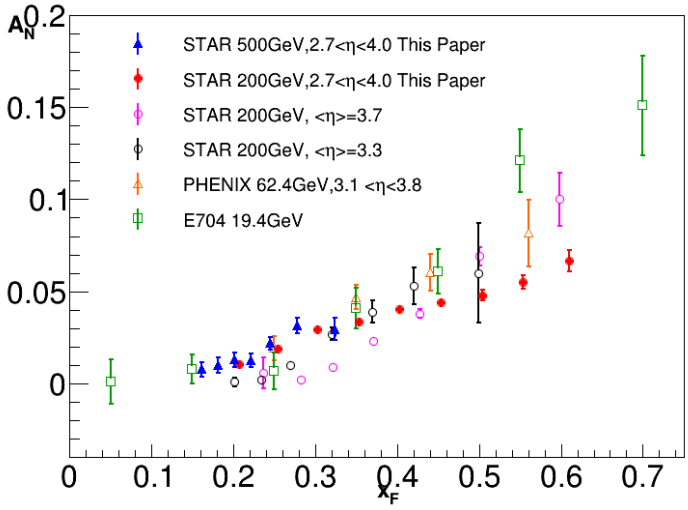

Figure 4.14: Multiple measurements of π^0 TSSAs [18].

ture. One group is the isolated π^0s, which refers to the π^0 with no other FMS points around. These isolated π^0s are considered not from parton hadronization. The other group contains the π^0s which are accompanied by other FMS points. Such π^0s are called non-isolated π^0 and are considered as a part of a jet which is fragmented from a parton.

In practice, the energy fraction z_{em} which is the π^0 energy over the jet energy is used to determine whether a π^0 is isolated or non-isolated. When z_{em} is close to one, it means that the π^0 energy takes almost 100% of the jet energy which suggests that no other FMS point is around. The jet reconstruction algorithm is anti-kT with the parameter R=0.7 which roughly indicates the $\eta - \phi$ coverage of a jet. It can now indicate the area where the π^0 is considered isolated.

Therefore the jet needs to be reconstructed first. And then the constituent FMS points of the jet are used to reconstruct the π^0 by their random combination. The reconstruction of π^0 is mostly the same as before. The only difference is now the FMS points which are used form pairs are restricted within the jet. Nevertheless, the two different reconstruction logic will have almost the same π^0 sample eventually because the trans-jet events are very limited, which means the decay photons of a π^0 belong to two different jets. Research shows that such events are less than 2% at the lowest x_F and 12% at the highest x_F.

Naturally, the π^0 selection remains the same as before. The distribution of the z_{em} of all π^0 candidate is shown in Figure(4.15). It can be seen that there is a clear separation between 0.95 and 1. When the π^0 energy ratio z_{em} is higher

than 0.98, it is considered isolated. In order to separate from isolated π^0s, the other group is required to have $z_{em} < 0.9$.

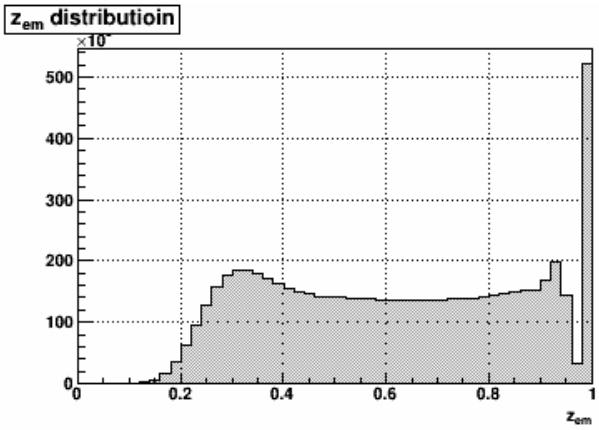

Figure 4.15: z_{em} distribution in the Collins asymmetry analysis.

Figure(4.16) shows the mass distribution of the two types of π^0 sample at 40 GeV, in Run-11. It is clear that the background fraction is rawly different since the isolated π^0s have a natural advantage in avoiding background because there are only two FMS points to begin with. To understand how much contributions to the overall TSSA from each group, Figure(4.17) shows the fractions of each group in the inclusive π^0 sample. Note that theses fractions are calculated with the π^0 signal, which is from the fitted result of the π^0 mass distribution. It can be seen that, for each year, the fraction of the isolated π^0 increase with x_F, therefore the isolated π^0s have more and more contributions to the overall inclusive TSSA.

Figure(4.18) and Figure(4.19) show the transverse spin asymmetries for both the isolated π^0 and non-isolated π^0 in Run-11 and Run-15. First of all, the background asymmetries are consistent with zero within uncertainty. For $x_F < 0$, the asymmetries in both year are consistent with zero within uncertainty as expected. But for $x_F > 0$, the asymmetries of the two groups are significantly different. Although they both rise as x_F increases, the asymmetries for the isolated π^0 are clearly larger than the asymmetries for the non-isolated π^0. It means the non-trivial asymmetries shown in Figure(4.8) and Figure(4.9) mainly come from the isolated π^0. The combined result of the TSSA of the π^0 signal at positive x_F is shown in Figure(4.20). It can be seen again that the results of the two dataset which differs in collision energy are consistent with each other. That is hint of weak energy dependence.

The energy correction in Table(3.7) shows the minimum reconstructed energy

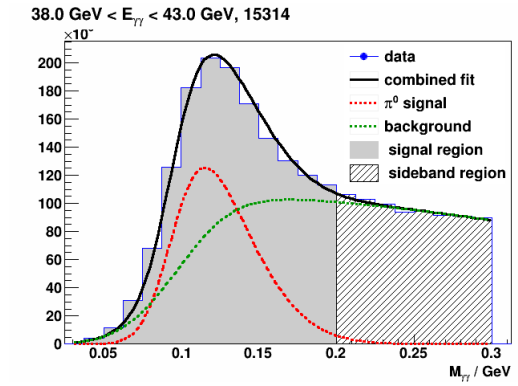

(a)

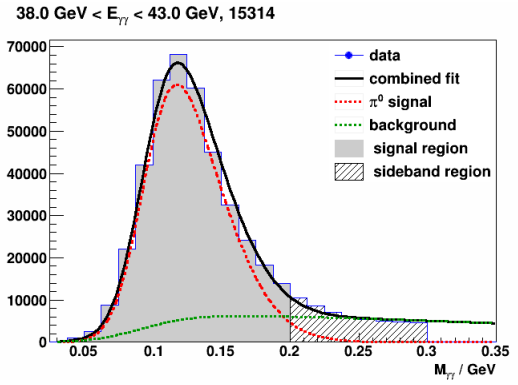

(b)

Figure 4.16: Example of the mass distribution for isolated π^0 in the right panel and non-isolated π^0 in the left panel at 40 GeV in Run-11.

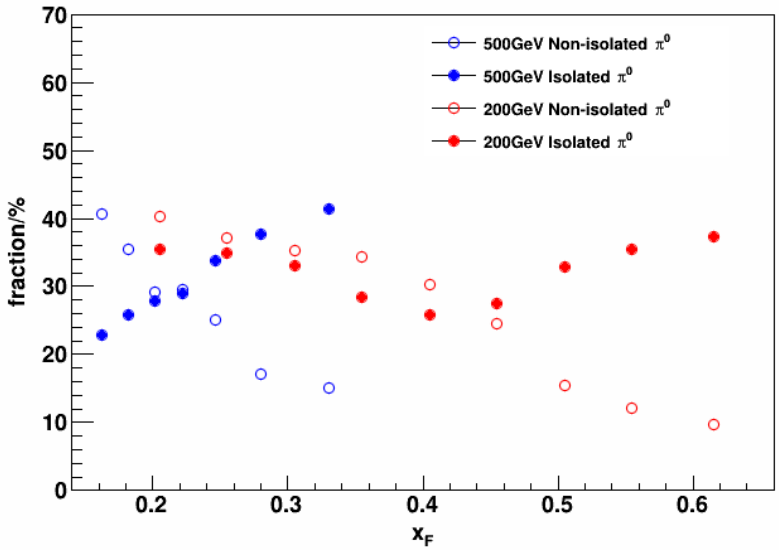

Figure 4.17: The signal fraction of the isolated/non-isolated π^0 in the overall inclusive π^0 sample in Run-11 and Run-15.

in the FMS is about 1 GeV. Since in very low energy region(about 1 GeV),the prediction of the correction function is a deduction from data points of other energies, the correction function is not very accurate in the low energy region. But what can be certain is the measured z_{em} would be a little bit higher than its actual value. So the isolated π^0 sample is not 100% pure even the z_{em} cut is very close to one. However, it does not change the conclusion of the above discussion.

It has been discussed in the introduction that the TSSA in proton-proton collision is considered originating from the twist-3 quark-gluon-quark correlations in the nucleon. However, this measurement puts some new insight into the discussion of the origin of the large TSSAs. The non-isolated π^0 is associated with parton fragmentation which is from the two to two QCD processes where the factorization works. The relatively lower asymmetries of the non-isolated π^0 could suggest that all the factorization models do not need to account for all of the large TSSAs.

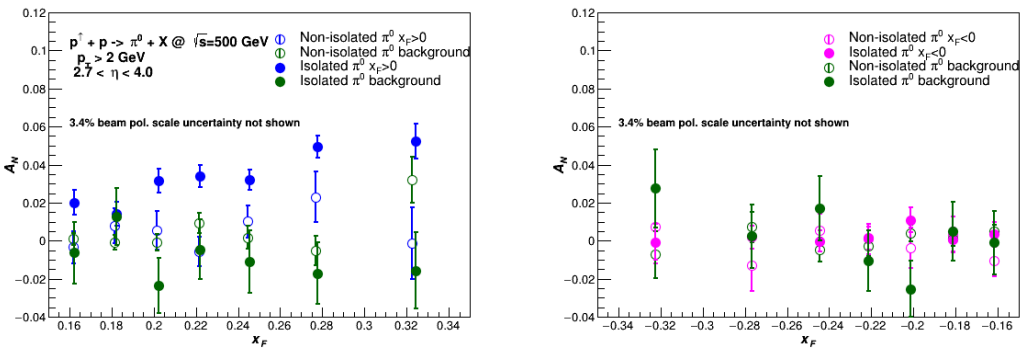

Figure 4.18: Results of Run-11 transverse single spin asymmetry of isolated/non-isolated π^0s. Left panel: for polarized blue beam $x_F < 0$; Right panel: for polarized yellow beam $x_F < 0$.

It has been pointed out in reference [18] that the isolated π^0 could be from diffractive processes. The diffractive processes refer to the events that one or both of the collision protons are intact after scattering. A Research[18] of PYTHIA-8 simulation shows that about 20% of the raw inclusive cross-section at forward rapidities is of diffractive nature. So these large TSSAs for the isolated π^0 are possibly large TSSAs of the diffractive processes. However, relevant experiments and theories about this relation are still very limited currently. A way to test this assumption is to analyze the correlations between forward scattered π^0s and tagged protons in the STAR data which is undergoing. Its result is crucial to

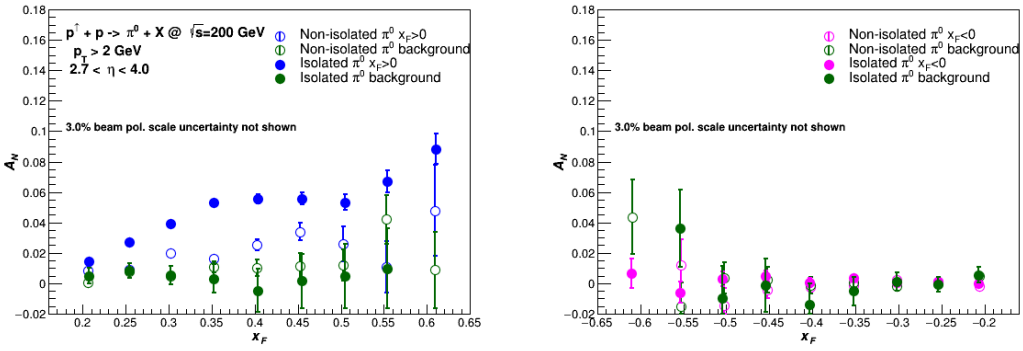

Figure 4.19: Results of Run-15 transverse single spin asymmetry for isolated/non-isolated π^0. Left panel: for polarized blue beam $x_F < 0$; Right panel: for polarized yellow beam$x_F < 0$

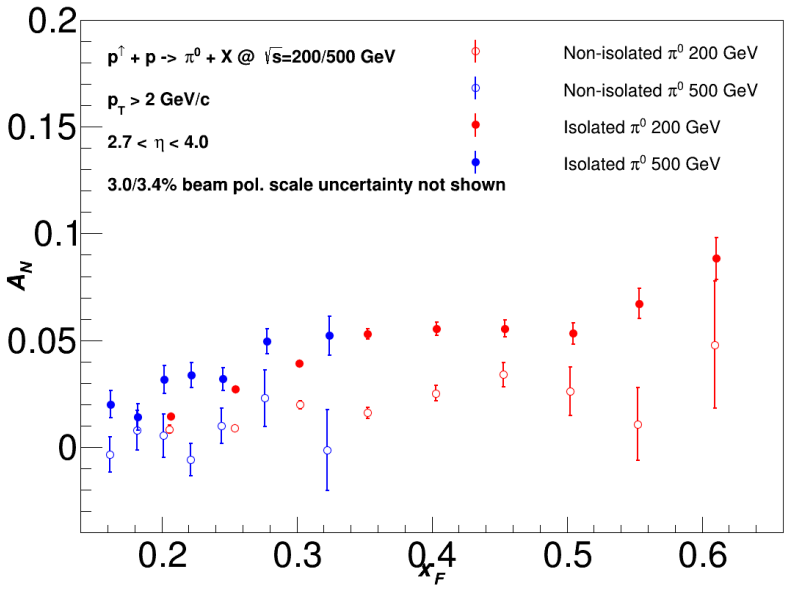

Figure 4.20: Combined results of the TSSA of only the isolated/non-isolated π^0 signal at $x_F > 0$ in Run11 and Run-15.

understand the origin of the large TSSA.

Note again that the jets mentioned here in this analysis are only the electromagnetic component of an actual jet due to the limited capability of the FMS being an electromagnetic calorimeter. Charged hadrons could change the current isolated/non-isolated classification. A more complete analysis can be done in the future with the new forward tracking system and the forward calorimeter system to be built by 2021 for STAR.

4.2.2 Transverse Single Spin Asymmetry of Jet

The jet selection cuts are summarized here. For jet selection:

- Algorithm: anti-kT R=0.7
- $2.7 < \eta < 4.0$
- $Pt > 2.0$

As mentioned before, the calculation of the jet TSSA is almost the same as the π^0 TSSA. Figure(4.21) and Figure(4.22) shows the results of the TSSA in Run-11 and Run-15. First of all, the background asymmetries are consistent with zero within uncertainty. For $x_F < 0$, the asymmetries in both year are consistent with zero within uncertainty as expected. For $x_F > 0$, the asymmetries are non-zero and rise as x_F. However the asymmetries are much smaller than the π^0's at the same x_F . Figure(4.23) shows the combined results of the jet TSSA at $x_F > 0$ in Run-11 and Run-15. It can be seen again that the results of the two dataset which differs in collision energy are consistent with each other. That is hint of weak energy dependence.

This is an interesting result, since the jet TSSA has no relation with the fragmentation function. So it should reflect the initial state effect to the TSSA. The jet is mainly the product of the parton fragmentation. The magnitude of its TSSA compared to the π^0's shows the overall initial state effect of the partons is very small. It suggests that the initial state effect should not be large enough to explain the large π^0 TSSA. However the nature of the electromagnetic jet makes it difficult to get a solid conclusion.

Note that there is no limitation on the photon multiplicity when reconstructing the jet. So a sole photon or two photons can be reconstructed as a jet. Figure(4.24) shows the photon multiplicity in the jet. Now consider the jet that contains only two photons. The photon pair could be from a decay pion which

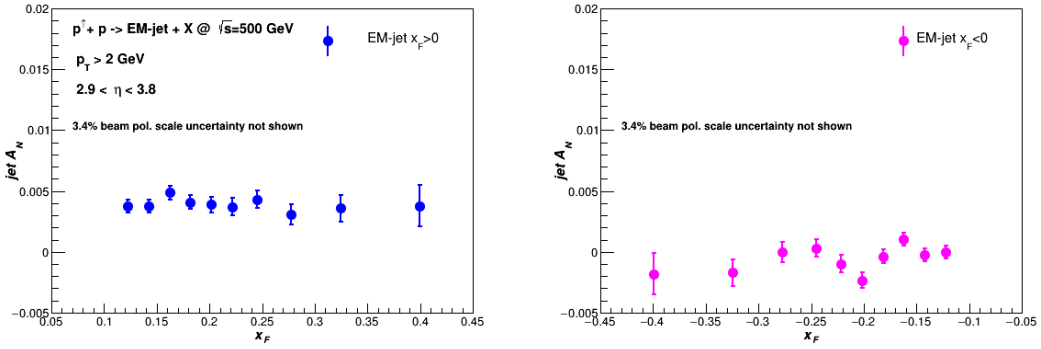

Figure 4.21: Results of Run-11 transverse single spin asymmetry of jet. Left panel: for polarized blue beam $x_F < 0$; Right panel: for polarized yellow beam $x_F < 0$.

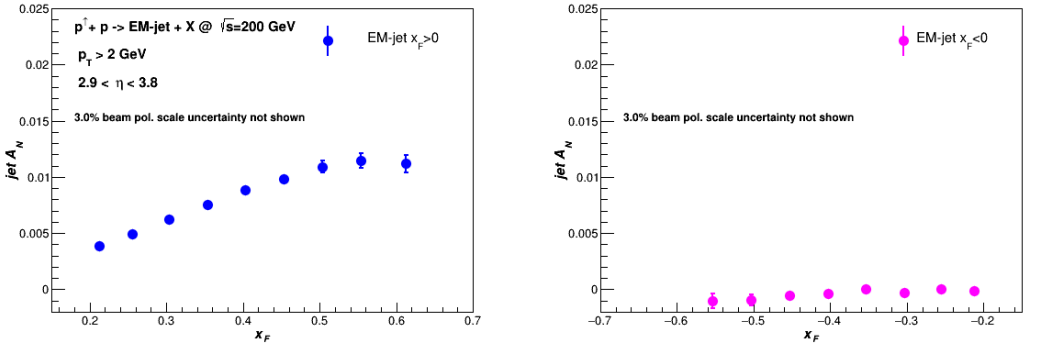

Figure 4.22: Results of Run-15 transverse single spin asymmetry of jet. Left panel: for polarized blue beam $x_F < 0$; Right panel: for polarized yellow beam $x_F < 0$.

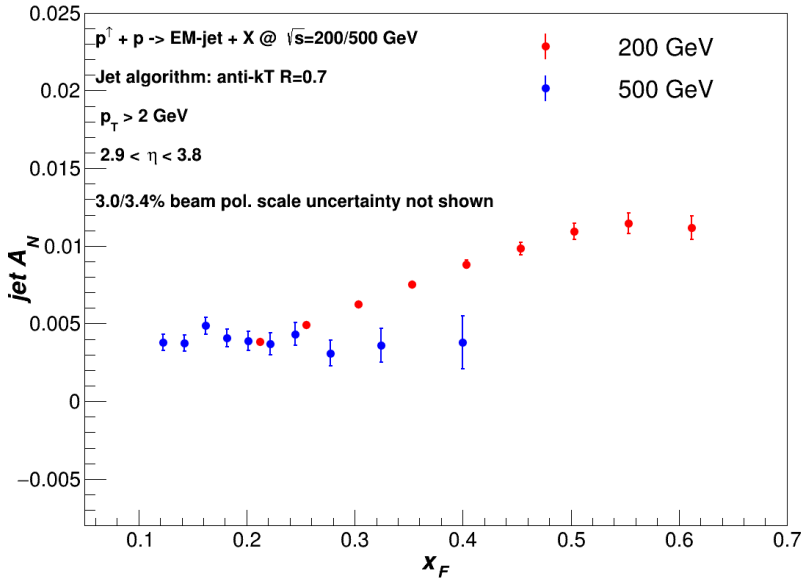

Figure 4.23: Combined results of the TSSA of jet at $x_F > 0$ in Run-11 and Run-15.

is exactly a isolated pion discussed in the pion TSSA measurement. Since it is known that such type of pion has the highest TSSA, it is not surprising that those events biased the jet TSSA. Therefore it is interesting to check the jet TSSA with photon multiplicity minimum requirement as three.

Figure(4.25) shows the combined results of the jet TSSA at $x_F > 0$ in Run-11 and Run-15 with and without the minimum multiplicity requirement. It is clear that the jet TSSAs with the minimum multiplicity requirement are smaller than the ones without the requirement, while the transverse momentum at each x_F of the two results is almost the same. It is anticipated as discussed above. Now check the energy dependence of the results with the minimum multiplicity requirement. The 200 GeV results are significantly larger than zero, while the 500 GeV results are consistent with zero, which shows strong energy dependence this time.

The black points are from a previous experiment of ANDY Collaboration[89]. The ANDY experiment was done in RHIC in 2011, using the data from 500 GeV transversely polarized proton-proton collision which is the same year as the Run-11 dataset in this thesis. The ANDY experiment is done with an electromagnetic colorimeter and a hadronic colorimeter. Therefore it can reconstructed a full jet. Its result show that the jet TSSA is consistent with zero. The Run-11 500 GeV

result with the minimum multiplicity requirement in this thesis is also consistent with zero. That means the TSSA of EM-jet with the minimum multiplicity requirement is a good resemblance of the full jet.

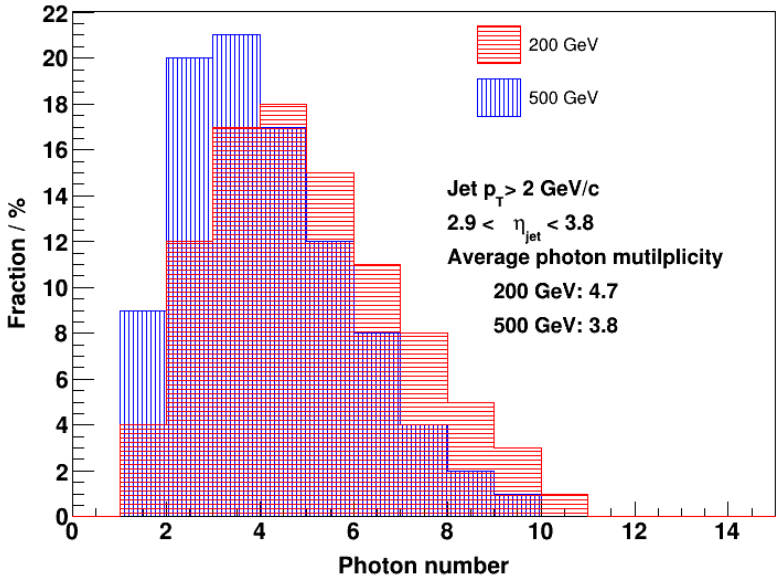

Figure 4.24: Photon multiplicity in the jet in Run-11 and Run-15

4.2.3 Collins Asymmetry

In the twist-3 factorization, the initial state effect and the final state effect are entangled in the π^0 TSSA result, which is an unavoidable disadvantage in studying the model from the π^0 TSSA result. A direct way to disentangle these two effects is to measure the Collins asymmetry. In the factorization scheme, the Collins asymmetry is related to the transversity PDF and the Collins fragmentation function, isolating itself from the initial state effect. So this measurement can provide useful separation of the two main sources of the TSSA.

The π^0 selection cuts are summarized here. For π^0 in a jet in Collins asymmetry A_{UT}:

For π^0 selection:

- $2.8 < \eta < 4.0$
- $Z_{\gamma\gamma} < 0.7$
- $M_{\gamma\gamma} < 0.3GeV$

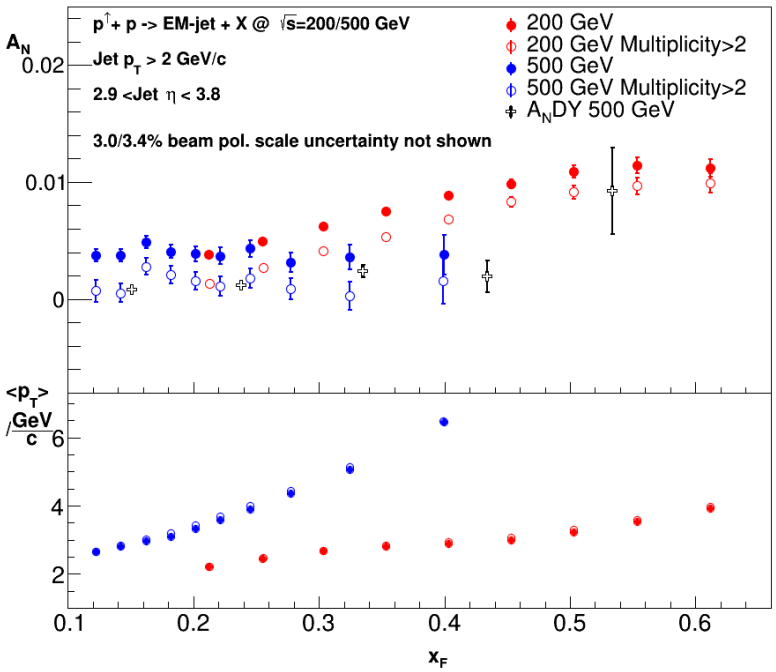

Figure 4.25: Combined results of the TSSA of jet at $x_F > 0$ in Run-11 and Run-15.

- $E_{\gamma\gamma} > 10GeV$

For jet selection:

- Algorithm: anti-kT R=0.7
- $2.8 < \eta < 4.0$
- $Pt > 2.0$
- $\Delta R > 0.04$

For the Collins asymmetry analysis, the reconstruction logic of the π^0 is slightly different from the random combination like in the TSSA analysis. The π^0 is required to be in a jet in the Collins asymmetry analysis. There is no need to include the π^0 candidates whose decay photons are not from the same jet. So the random combination is performed within a jet. These π^0 candidates share the same cuts as in the TSSA analysis except for the Pt cut and a new 10 GeV minimum energy requirement. The Pt cut is not needed because a Pt cut has been applied to the jet. The minimum energy requirement is due to the uncertainty in low energy FMS points and actually it is automatically met due to the other kinematic cuts.

Since the jet axis is not fixed, it is hard to have a clear definition of background. And the number of FMS points inside a jet is limited, so the correlation of the asymmetries in the signal and background is strong. The smaller the number of FMS points is, the stronger the correlation is. In some sense, the signal and the background is inseparable within a jet. Instead of trying to do a background subtraction like in π^0 TSSA measurement, the background is treated as signal in the Collins asymmetry analysis. The mass window is chosen as less than 0.3 GeV. In practice, all the FMS points are used only once in the π^0 reconstruction in order to reduce the background and avoid double counting. So, starting with the highest energy π^0 candidate, it will be checked if it can pass all the π^0 cuts. If it does, then its constituent FMS points will be excluded from the list. If it doesn't, then check the second highest energy π^0 candidate until a qualified candidate appears. After excluding the photons of the qualified π^0 candidate, the rest of them can form a new group of π^0 candidates. Then the same check applies to the highest energy π^0 candidate in this group. This process goes on and on until there are no more π^0 candidates to check.

One way to see the influence of the inseparable background is to check the mass dependence of the Collins asymmetry. Since the mass cut is placed on 0.3

GeV, as previous experience, the signal mostly concentrate in region 0-0.2 GeV. If the asymmetries for the signal and background are very different, it should show strong mass dependence. Figure(4.26) shows such mass dependence for both Run-11 and Run-15. It can be seen that for two dataset, the asymmetries for two mass region are all consistent with zero. And the mass dependence can not be found for both dataset.

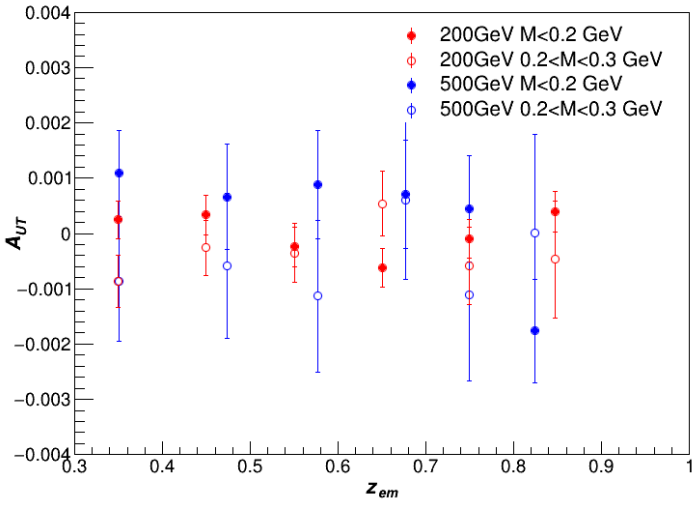

Figure 4.26: Mass dependence of Collins asymmetry for the polarized blue beam Run-11 and Run-15

The results of the Collins asymmetry are shown in Figure(4.27) for Run-11, and in Figure(4.28) for Run-15. For $x_F < 0$, the conclusion is the same as before: the asymmetries are consistent with zero within uncertainty in both years. For $x_F > 0$, the asymmetries for each set of points are also consistent with zero within uncertainty in both years. In every panel, there are two sets of data points for different j_T ranges, which is the transverse momentum of the π^0 versus the jet thrust axis. The Collins angle (ϕ_C) resolution is a major source of the asymmetry uncertainty, which was discussed in 4.1.2.2. When the direction of the momentum of the π^0 is close to the jet thrust axis, the uncertainty of the ϕ_H angle would become large. Such uncertainty would be propagated to the ϕ_C angle and thus brings uncertainty to the asymmetries. One could expect that there are many such events in the high z_{em} bin. Therefore, a ΔR cut should be applied to reject them in the analysis. $\Delta R = \sqrt{((\eta_{\pi^0} - \eta_{jet})^2 + (\phi_{\pi^0} - \phi_{jet})^2}$, which measures how close between the π^0 and the jet thrust axis. The setting of this cut has to be balanced with the benefit of excluding those large uncertainty events and the

statistics loss in high z_{em} bin. The final choice is $\Delta R > 0.04$. To examine this effect, the asymmetries are plotted in different j_T bins. Due to the limitation of the statistics, there are only two j_T bins, $j_T < 0.2$ GeV and $j_T > 0.2GeV$. The results show that for both j_T bins, the Collins asymmetries are zero within the uncertainty.

The Collins asymmetries of two j_T bins for 200 GeV shows a little bit difference, see the left panel of Figure(4.28). A further investigation of the j_T dependence can be found in Figure(4.29). The Collins asymmetries are separated into four j_T bins, in which the asymmetries of $j_T > 0.2GeV$ seems to be negative and $j_T < 0.2GeV$ to be positive in large z_{em}. The cause of the small j_T dependence is unknown.

Since there are no significant difference between the results of the two different j_T bins, it is suitable to combine the results of the two j_T bins. Figure(4.30) shows that the Collins asymmetries in Run-11 and Run-15 are consistent with zero within the uncertainty. Since the Collins asymmetry is considered originating from the fragmentation function, this result shows such contribution is consistent with zero. In another angle, the final state effect should be small in the π^0 TSSA.

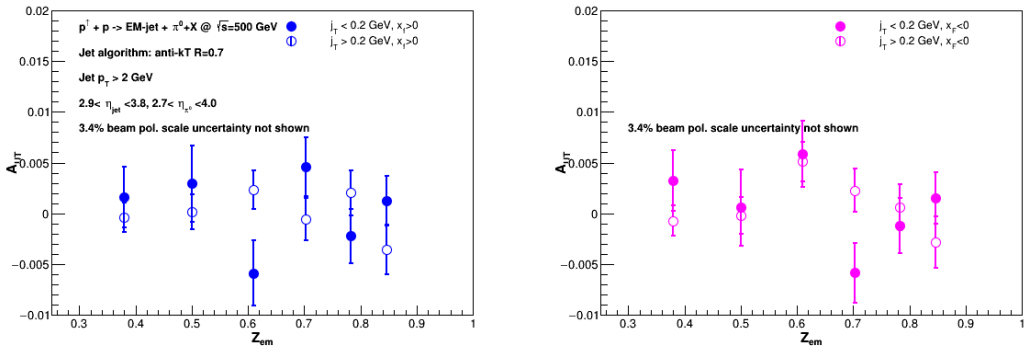

Figure 4.27: Results of Run-11 Collins asymmetry for the polarized blue beam and the polarized yellow beam. Left panel: for $j_T < 0.20$ GeV; Right panel: for $j_T > 0.20$ GeV

4.3 Comparison to Model Calculation

4.3.1 π^0 Transverse Single Spin Asymmetry

In reference [90], it presents the calculation of the TSSA of single pion production for proton-proton collisions. This calculation is dedicated to a proposed

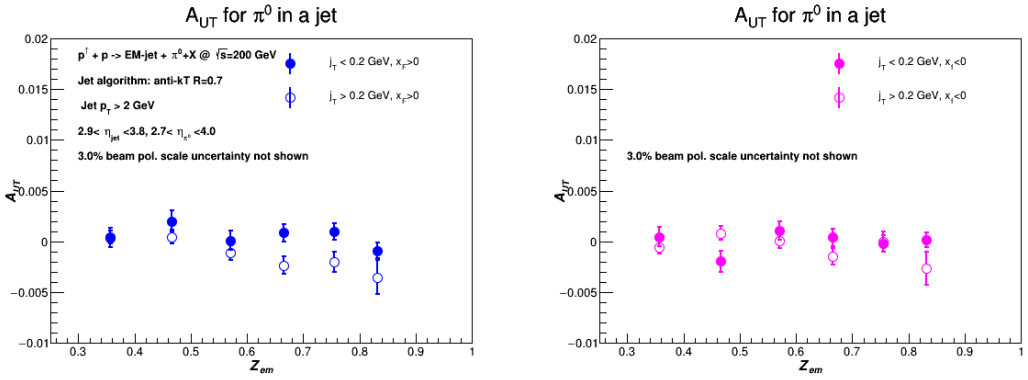

Figure 4.28: Results of Run-15 Collins asymmetry for polarized blue beam and polarized yellow beam. Left panel: for $j_T < 0.20$ GeV; Right panel: for $j_T > 0.20$ GeV

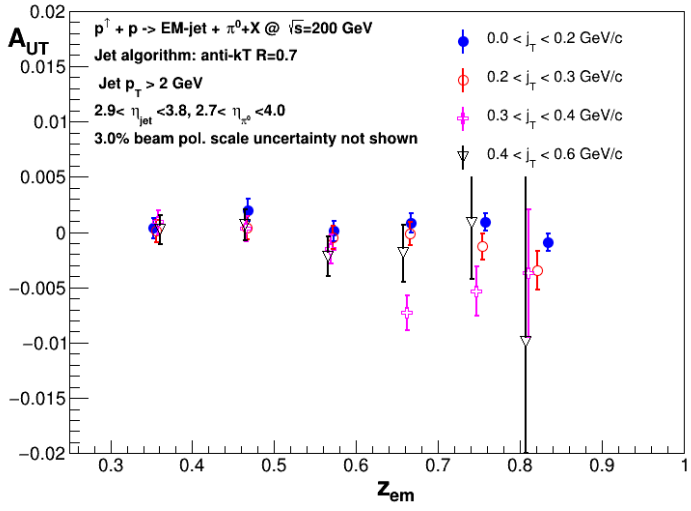

Figure 4.29: Result of j_T dependence of Run-15 Collins asymmetry for polarized blue beam.

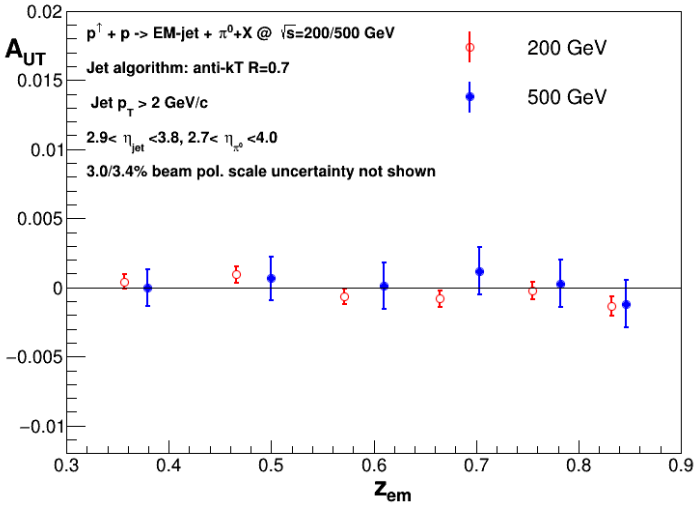

Figure 4.30: Result of Run-11 and Run-15 Collins asymmetry for polarized blue beam combining two j_T-bins.

experiment AFTER at LHC, which is a fixed target experiment at $\sqrt{s} = 115GeV$. The collision energy is different from the analysis in this thesis, which is 200 GeV in Run-15 and 500GeV in Run-11. Since the TSSAs do not strongly depend on energy scale from the discussion from Section(4.2), the theoretical prediction of the TSSA from reference [90] can be used to compare with the measurements in this thesis.

Figure(4.31) shows TSSAs versus x_F at $\sqrt{s} = 115GeV$ for inclusive pion. The pseudorapidity is fixed at 3.0 which is within the coverage of the FMS ($2.5 < \eta < 4.1$). In the measurement in this thesis, the average pseudorapidity for each x_F is different between 3.0 to 4.0. In principle, the TSSAs are pseudorapidity dependent so that this theoretical prediction is not suitable for quantitative comparison with the measurement in this thesis. Instead, we can only perform a qualitative comparison here.

The calculation in reference [90] is based on the TMD factorization, where the Sivers function and the Collins function are considered as the major source of the TSSA. It calculates these two effects individually like Equation(4.27) and adds them in the final result in Figure(4.31). The two panels in Figure(4.31) represent different TMD PDF and FF sets which are extracted from SIDIS data and electron-positron annihilation data. In the left panel, the Sivers function and the Collins function are extracted from reference [91][92] while in the right panel they are extracted from reference [93][94]. Note that, for both sets of the Sivers

functions, the gluon Sivers distributions are considered to be vanishing. It adopts the GRV98LO PDF set [95] as the unpolarized PDFs, while the DSS set [96]and the Kretzer set [97] as the fragmentation functions.

$$A_N = \frac{\left[d\sigma^{\uparrow} - d\sigma^{\downarrow}\right]_{\text{Sivers}} + \left[d\sigma^{\uparrow} - d\sigma^{\downarrow}\right]_{\text{Collins}}}{d\sigma^{\uparrow} + d\sigma^{\downarrow}} \tag{4.27}$$

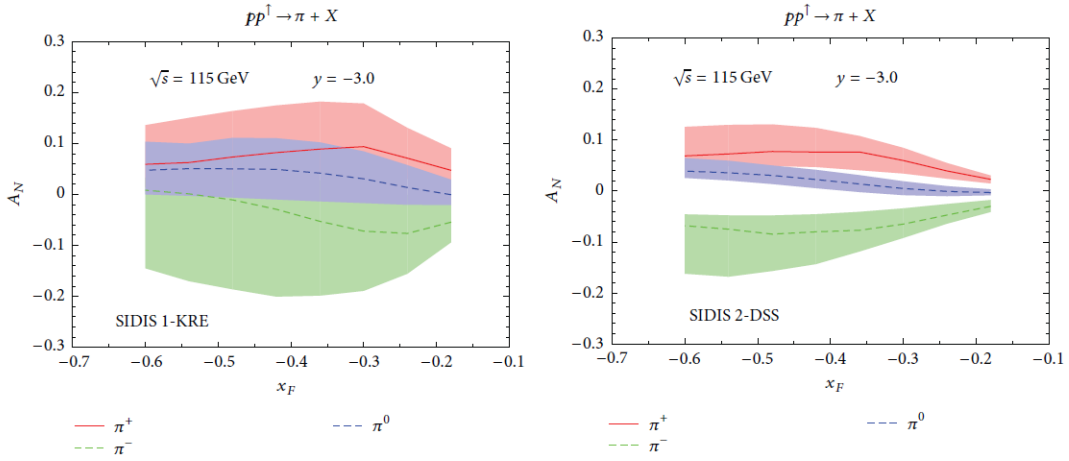

Figure 4.31: Theretical prediction for pion TSSA as function of x_F, purple line and shade is for neutral pion. Left panel: TMD set 1; Right panel: TMD set 2 [90].

Note that the minus sign of x_F and y (pseudorapidity) in Figure(4.31) is due to different definition. They are equivalent to the positive one in this thesis. Here the discussion would follow the definition in the thesis. For π^0, both of the theoretical calculations are consistent with each other. The TSSA rises from about 0.0 at $x_F = 0.2$ to about 0.05 at $x_F = 0.6$. The SIDIS-2 set has a much narrower uncertainty band which is obtained from a procedure described in reference[93].

Figure(4.10) combines the TSSA results in which $x_F > 0$ from Run-11 and Run-15. It provides a wide spectrum of TSSA verse the x_F from 0.15 to 0.6. Since the collision energy is lower in Run-15, the data points from Run-15 will fall on the right part of the figure where $x_F > 0.4$. The measurement result at low x_F in Figure(4.10) is slightly larger than zero which is within the uncertainty of the SIDIS-1 set and probably the SIDIS-2 set too. The prediction shows the TSSA rises as x_F, which is the conclusion of the measurement. And the SIDIS-2 set seems to be more close to the measurement result. At large x_F, the measurement shows the asymmetry is around 0.06 at the highest x_F, which is also consistent with both of the theoretical calculations within the uncertainty band. In general,

the behavior of the TSSA results can be described by this prediction.

But just as mentioned in the isolated/non-isolated π^0 TSSA result, the different asymmetry scale of the two subsets and the high asymmetry for the isolated π^0 is not understood at all, see Figure(4.20). And the theorist for the time being always consider that the TSSA comes from the initial state or final state effect, which has no information about these subsets of the data. This raises a lot of questions for the discussion. If the non-isolated π^0 is related to the parton fragmentation and the isolated π^0 is not, then the model calculation so far should account for the TSSA of the former subset only but not the whole TSSA. And the origin of the high asymmetry for the isolated π^0 must be out of the current TMD or twist-3 Collinear factorization framework.

4.3.2 Jet Transverse Single Spin Asymmetry

In reference[98], it summarized two theoretical predictions for the jet TSSA. In Figure(4.32), the red band and blue band represent two different prediction, the data points are from ANDY experiment at RHIC[89] for inclusive jet production at forward pseudorapidity 3.25 in 500 GeV polarized proton-proton collision.

The prediction of red band are based on the TMD factorization[99]. It uses the Sivers function from SIDIS directly in the calculation. The prediction of blue band use the twist-3 collinear factorization model[100] which also use the Sivers function extracted from SIDIS as input. Since a jet covers all the final states, it should be only sensitive initial effect. Since the TSSA of π^+ and π^- is of the similar magnitude but different in sign, the cancellation can be anticipated when it comes to the jet TSSA, which makes it small.

Figure(4.23) shows the combined results of the jet TSSA at $x_F > 0$ in 200 and 500 GeV. The asymmetry arises from zero at x_F 0.1 to 0.015 at x_F 0.6. Compared to the theoretical predictions, at low x_F, the measurement result is closer to the twist-3 factorization calculation; at high x_F, it is closer to the TMD factorization calculation.

Note that in this measurement, the jet is a partial jet. So it cannot fully represent the measurement result of a full jet. The influence the missing information is unknown to the measurement in this analysis. In reference[98], it points out that the jets triggered by the electromagnetic calorimeter bias the fragmentation by detecting more π^0 events, which tends to overestimate the TSSA. The TSSA of a full jet might be closer the the blue band than the electromagnetic jet.

Therefore it is not rawly appropriate to compare the TSSA of electromagnetic-jet to the prediction of a full jet.

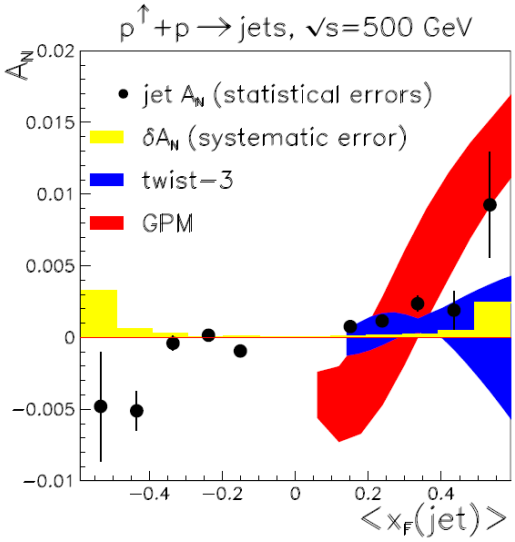

Figure 4.32: Theoretical prediction for jet TSSA as function of x_F[98].The red/blue bands are prediction from models considering the Sivers effect.

4.3.3 Collins Asymmetry

In reference [34], it calculates the Collins asymmetry for pion production in a jet in the proton-proton collision at $\sqrt{s}$=200GeV. It extracts the so-called 1/2-moment of the Collins function from the SIDIS data at HERMES[101]. Quark transversity distributions are parameterized in reference [102]. Figure(4.33) shows the Collins asymmetry as function of jet pseudorapidity(left panel) and of jet transverse momentum (right panel) for the pions. The green line represents the neutral pion and it is zero throughout the whole kinematic range. Note that the asymmetry for π^+ is negative which in other literature is positive. That is because in reference [34] the Collins angle is defined as $\phi_C = \phi_H - \phi_S$ while it is $\phi_C = \phi_S - \phi_H$ in other literature.

The small Collins asymmetry for π^0 can be understood as follows. It suffers from two possible cancellations: the opposite sign between and d quark transversity distributions and the opposite sign between the favored and disfavored Collins fragmentation functions[34], which describes relations between quark flavor and the final hadron species. Favored function is like $D_u^{\pi^+}$, which means the fragmentation function for u quark to a π^+. ， $D_u^{\pi^-}$ is unflavored in the other hand. As a

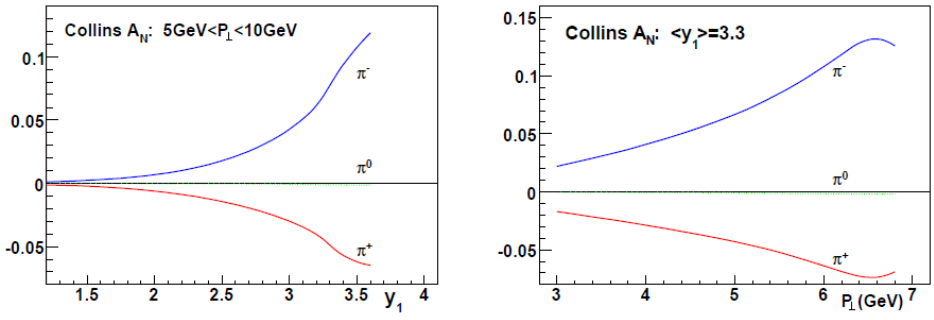

Figure 4.33: Theoretical prediction for Collins asymmetry of pion in a jet. Left panel: as function of jet pseudorapidity; Right panel: as function of jet transverse momentum [34].

comparison, the Sivers effect only has one cancellation between u and d flavors, since it couples to the unpolarized fragmentation functions. The existence of the cancellation for π^0 suggests that the charged pion would be a better probe to test the Collins asymmetry, which can be done after the STAR forward upgrade.

Note that in the Collins asymmetry measurement, the jet is a partial jet. The result from it cannot fully represent the measurement result from a full jet. So the lack of information of changed hadrons could simply just worsen the Collins angle resolution without changing its mean, therefore the current result would not be very different from that using a full jet. It is also possible that the Collins angle resolution becomes so bad that the any asymmetry cannot be seen from the data. However, the current detector does not allow to make any conclusion out of this. Future measurement after the STAR forward upgrade would be enough to answer it.

4.3.4 Summary

In summary the theoretical prediction which uses TMD PDFs extracted from the SIDIS and electron-positron annihilation experiment can describe the data of TSSA of inclusive π^0 and TSSA of inclusive electromagnetic jet and the Collins asymmetry of π^0 in an electromagnetic jet in 200 GeV and 500 GeV proton-proton collision at RHIC STAR. Further comparison to the theoretical prediction with better precision would require effort from both experimentalists and theorists. From the theorists' side, extraction of the Sivers function and Collins function can be updated with new SIDIS data in the recent years which will better constrain

the uncertainty band in the prediction. New calculation targeting the STAR and FMS kinematics is needed. And at last, how the isolated π^0 TSSAs relate to the theory needs to be clarified. On the experimental side, it not only requires new TSSA data of more particles after the STAR forward upgrade in the proton-proton collision but also more data of SIDIS and electron-positron annihilation experiment to get better extraction of the Sivers function, Collins function, and the transversity.

Chapter 5 Summary and Outlook

Transverse single spin asymmetries of particle production at large x_F have been observed in various processes from semi-inclusive deep inelastic scattering (SIDIS) to polarize proton-proton collisions over a wide range of center-of-mass energies. Two theoretical approaches as an extension of the collinear factorization are proposed in the past decade to explain the TSSAs. The two approaches are the one based on transverse momentum dependent parton distribution functions and the other based on twist-3 collinear factorization. Both models need to be tested in the experiment, which makes studying the polarized proton structure very important. The measurements described in this thesis represent one of the many efforts from the experimental side to test these models over a wide range of kinematics. TSSAs in polarized proton-proton collisions are complementary to SIDIS in kinematics and they represent an excellent test of universality for the transverse momentum dependent PDFs extracted from SIDIS and electron-positron annihilation.

In this thesis, we measured the transverse single spin asymmetry for π^0 production in 200 GeV and 500 GeV polarized proton-proton collision at RHIC. The Forward Meson Spectrometer, an electromagnetic calorimeter, at STAR is used to perform the measurements. It is observed that the TSSAs rise as x_F at wide range between 0.16 to 0.6. Large TSSAs are observed at large x_F which is consistent with earlier experiments. Combined with other measurements at different energies, it can show that the TSSAs weakly depend on the collision energy. Comparison are made with the theoretical predictions which are based on the TMD. The data is basically in agreement with the model [90]. A further examination of the TSSAs dividing the π^0 sample into two categories based on whether there is additional energy picked up by the FMS around the π^0. The asymmetries of the non-isolated π^0 are considered to be mainly from parton fragmentation while the isolated π^0 may be connected to the diffractive process. The TSSA of the isolated π^0 is significant larger than that of the non-isolated π^0 at wide x_F range. The larger asymmetries for the isolated π^0 suggests that the origin of the TSSA is more complicated than expected. However, the diffractive process is not fully understood and the role of the it in the TSSA is totally unfamiliar to the community. It requires further experiments to provide more

information.

To better isolate the initial state effect (Sivers effect) from the final state effect (Collins effect), the Collins asymmetry of π^0s in an electromagnetic jet is measured. The Collins asymmetry is considered to be only related to the final state effect. The obtained result is consistent with zero within the uncertainty. It is in good agreement with the theoretical prediction in reference[34] which predicts the Collins asymmetry to be close to zero. However, the influence of the usage of the electromagnetic jet instead of a full jet is unknown in this result. The TSSA of the electromagnetic jet which is considered to be only sensitive to initial state effect is also measured. The asymmetries are non-zero and rise as x_F. The asymmetries are much smaller than the π^0's at the same $x_F 0$. Model prediction in reference [98] shows that the jet TSSA should be small due to the cancellation of the u and d quark Sivers function. But since the jet is a partial jet in the measurement, it is not totally appropriate to compare the TSSA of electromagnetic-jet to the prediction of a full jet.

Combining all the three measurement in this thesis, the π^0 TSSA, the electromagnetic jet TSSA and the Collins asymmetry in the π^0, it generates a multi-dimensional picture of the origin of the relatively large π^0 TSSA. The jet TSSA result shows that the initial state effect should be small. However, in reference[99], it shows the relatively small jet TSSA and relatively large π^0 TSSA can co-exist. The Collins asymmetry result also shows that the final state effect should be small although the incomplete jet is always a obstacle to make a solid conclusion. The hard process in QCD should be unable to generate the large π^0 TSSA. Although there are calculations claiming that the initial state effect or the final state effect alone can generate the large π^0 TSSA, the measurement results now does not show very clear support. It only shows hints that the initial state effect could be promising. Also the isolated π^0 TSSA results propose that there could be a new origin of the large π^0 TSSA other than the initial state effect and the final state effect in all factorization schemes which may only need to account for the non-isolated π^0 TSSA. In summary, the origin of the large π^0 TSSA is still unknown. Future experiments and theoretical advancement are needed if one wants to fully understand this topic.

There are still many open questions to be answered in the transverse spin structure of the proton, for example, the validation of the factorization schemes, the universality of the Collins function and extraction of the TMD functions or

their counterpart in twist-3 collinear factorization. To get a full picture of the transverse spin structure of the proton, efforts from both experimentalists and theorists are needed. More experimental data from STAR with the upcoming forward upgrade and the future EIC would help clarify a lot of the questions.

STAR is currently designing a detector upgrade at forward rapidities ($2.4 < \eta < 4.2$). It includes a brand new tracking system and a forward calorimeter system. The tracking system is made of three layers of silicon mini-strip disks and four layers of small-Strip Thin Gap Chambers (sTGC). The calorimeter system consists of an electromagnetic calorimeter and a hadronic calorimeter. Both the tracking system and the calorimeter system have a coverage of $2.4 < \eta < 4.2$, similar to the current FMS. With the forward upgrade, STAR will have the ability to detect charged particles at forward pseudorapidity. This will have a great improvement to the analysis in this thesis. For the transverse single spin asymmetry and Collins asymmetry, more species mean the ability to probe the distribution functions for different quark flavors. For the Collins asymmetry and the jet TSSA, it will be possible to construct the full jet instead of the current partial electromagnetic jet. This will enable to construct the true Collins angle which will provide a precise Collins asymmetry.

In the future, the Electron Ion Collider as the next generation high energy physics accelerator will have high luminosity high polarized electron and ion beams and have better kinematic coverage than any current experiment. For nucleon structure, it will feature in multiple physics topics including spin and flavor structure of the nucleon, the confined motion of partons inside the nucleon and the spatial imaging of gluons and sea quarks. All this analysis will push our understanding of the proton structure to the next level.

Bibliography

[1] A. Pais. *Inward Bound: Of Matter and Forces in the Physical World*. Oxford paperbacks. Clarendon Press, 1988. ISBN: 9780198519973.

[2] S. Chekanov, D. Krakauer, S. Magill, et al. "ZEUS next-to-leading-order QCD analysis of data on deep inelastic scattering". In: *Physical Review D* 67.1 (2003), p. 012007.

[3] G. Zweig. "An SU(3) model for strong interaction symmetry and its breaking. Version 2". In: *DEVELOPMENTS IN THE QUARK THEORY OF HADRONS. VOL. 1. 1964 - 1978*. Ed. by D.B. Lichtenberg and Simon Peter Rosen. 1964, pp. 22–101.

[4] M. Gell-Mann. "A Schematic Model of Baryons and Mesons". In: *Physical Letter* 8 (1964), pp. 214–215.

[5] D. P. Barber et al. "Discovery of Three Jet Events and a Test of Quantum Chromodynamics at PETRA Energies". In: *Physical Review Letter* 43 (1979), p. 830.

[6] S.E. Kuhn, J-P. Chen, and E. Leader. "Spin structure of the nucleon—status and recent results". In: *Progress in Particle and Nuclear Physics* 63.1 (2009), pp. 1–50.

[7] J. Ashman, B. Badelek, G. Baum, et al. "A measurement of the spin asymmetry and determination of the structure function g1 in deep inelastic muon-proton scattering". In: *Physics Letters B* 206.2 (1988), pp. 364–370.

[8] C.A. Aidala, S.D. Bass, D. Hasch, and G.K. Mallot. "The spin structure of the nucleon". In: *Reviews of Modern Physics* 85.2 (2013), p. 655.

[9] M. Tanabashi, K. Hagiwara, K. Hikasa, et al. "Review of particle physics". In: *Physical Review D* 98.3 (2018), p. 030001.

[10] R.L. Jaffe and A. Manohar. "The g1 problem: Deep inelastic electron scattering and the spin of the proton". In: *Nuclear Physics B* 337.3 (1990), pp. 509–546.

[11] X. Ji. "Gauge-invariant decomposition of nucleon spin". In: *Physical Review Letters* 78.4 (1997), p. 610.

[12] X. Ji, J. Zhang, and Y. Zhao. “Justifying the naive partonic sum rule for proton spin”. In: *Physics Letters B* 743 (2015), pp. 180–183.

[13] L. Adamczyk et al. “Longitudinal and transverse spin asymmetries for inclusive jet production at mid-rapidity in polarized p+ p collisions at s= 200 GeV”. In: *Physical Review D* 86.3 (2012), p. 032006.

[14] D. de Florian, R. Sassot, M. Stratmann, and W. Vogelsang. “Evidence for polarization of gluons in the proton”. In: *Physical Review Letter* 113.1 (2014), p. 012001.

[15] R.D. Klem, J. E. Bowers, H. W. Courant, et al. “Measurement of Asymmetries of Inclusive Pion Production in Proton-Proton Interactions at 6 and 11.8 GeV/c”. In: *Physical Review Letter* 36 (16 1976), pp. 929–931.

[16] D.L. Adams, N. Akchurin, N.I. Belikov, et al. “Analyzing power in inclusive $\pi+$ and $\pi-$ production at high xF with a 200 GeV polarized proton beam”. In: *Physics Letters B* 264.3-4 (1991), pp. 462–466.

[17] D.L. Adams, Y. Onel, F. Lehar, et al. “Comparison of spin asymmetries and cross-sections in pi0 production by 200-GeV polarized anti-protons and protons”. In: *Physics Letters* 261.ANL-HEP-PR-91-14 (1991), pp. 201–206.

[18] E.C. Aschenauer, A. Bazilevsky, K. Boyle, et al. “The RHIC spin program: achievements and future opportunities”. In: *arXiv preprint arXiv:1304.0079* (2013).

[19] V. Barone and P.G. Ratcliffe. *Transverse spin physics*. World Scientific, 2003.

[20] X. Ji, J. Qiu, W. Vogelsang, and F. Yuan. “Unified picture for single transverse-spin asymmetries in hard-scattering processes”. In: *Physical Review Letter* 97.8 (2006), p. 082002.

[21] L. L. Pappalardo, Hermes Collaboration, et al. “Accessing TMDs at HERMES”. In: *AIP Conference Proceedings*. Vol. 1441. 1. AIP. 2012, pp. 229–232.

[22] F. Gautheron, W. Eyrich, V. Konstantinov, et al. *Compass-ii proposal*. Tech. rep. 2010.

[23] H.A. Avakian. “TMD measurements at CLAS”. In: *Nuovo Cim.* 36.JLAB-PHY-14-1836; DOE/OR/23177-3016 (2013).

[24] A. Accardi, J.L. Albacete, M. Anselmino, et al. “Electron-ion collider: The next QCD frontier”. In: *The European Physical Journal A* 52.9 (2016), p. 268.

[25] D. Sivers. “Single-spin production asymmetries from the hard scattering of pointlike constituents”. In: *Physical Review D* 41 (1 1990), pp. 83–90.

[26] S.J. Brodsky, D.S. Hwang, and I. Schmidt. “Final-state interactions and single-spin asymmetries in semi-inclusive deep inelastic scattering”. In: *Physics Letters B* 530.1-4 (2002), pp. 99–107.

[27] A. Airapetian, N. Akopov, Z. Akopov, et al. “Single-spin asymmetries in semi-inclusive deep-inelastic scattering on a transversely polarized hydrogen target”. In: *Physical Review Letters* 94.1 (2005), p. 012002.

[28] J. Collins. “Leading-twist single-transverse-spin asymmetries: Drell–Yan and deep-inelastic scattering”. In: *Physics Letters B* 536.1-2 (2002), pp. 43–48.

[29] J. Collins. “Fragmentation of transversely polarized quarks probed in transverse momentum distributions”. In: *Nuclear Physics B* 396.1 (1993), pp. 161–182.

[30] A. Airapetian, N. Akopov, Z. Akopov, et al. “Effects of transversity in deep-inelastic scattering by polarized protons”. In: *Physics Letters B* 693.1 (2010), pp. 11–16.

[31] B. Parsamyan. “Transverse spin azimuthal asymmetries in SIDIS at COMPASS: Multidimensional analysis”. In: *International Journal of Modern Physics: Conference Series*. Vol. 40. World Scientific. 2016, p. 1660029.

[32] X. Qian, K. Allada, C. Dutta, et al. “Single Spin Asymmetries in Charged Pion Production from Semi-Inclusive Deep Inelastic Scattering on a Transversely Polarized He 3 Target at Q 2= 1.4–2.7 GeV 2”. In: *Physical Review Letter* 107.7 (2011), p. 072003.

[33] L. Adamczyk et al. “Azimuthal transverse single-spin asymmetries of inclusive jets and charged pions within jets from polarized-proton collisions at s= 500 GeV”. In: *Physical Review D* 97.3 (2018), p. 032004.

[34] F. Yuan. “Azimuthal Asymmetric Distribution of Hadrons Inside a Jet atHadron Collider”. In: *Physical Review Letters* 1.LBNL-63437; RBRC-689 (2007).

[35] U. D' Alesio, F. Murgia, and C. Pisano. "Azimuthal asymmetries for hadron distributions inside a jet in hadronic collisions". In: *Physical Review D* 83.3 (2011), p. 034021.

[36] Z. Kang, A. Prokudin, F. Ringer, and F. Yuan. "Collins azimuthal asymmetries of hadron production inside jets". In: *Physics Letters B* 774 (2017), pp. 635–642.

[37] J. Qiu and G. Sterman. "Single transverse-spin asymmetries in hadronic pion production". In: *Physical Review D* 59.1 (1998), p. 014004.

[38] R.L. Jaffe, H. Meyer, and G. Piller. "Spin, twist and hadron structure in deep inelastic processes". In: *Lectures on QCD*. Springer, 1997, pp. 178–249.

[39] R. L. Jaffe. "Chiral-Odd Parton Distributions and Polarized Drell-Yan". In: *Spin and Isospin in Nuclear Interactions*. Springer, 1991, pp. 145–153.

[40] D. Boer and P. J. Mulders. "Time-reversal odd distribution functions in leptoproduction". In: *Physical Review D* 57 (9 1998), pp. 5780–5786.

[41] K. Kanazawa, Y. Koike, A. Metz, and D. Pitonyak. "Towards an explanation of transverse single-spin asymmetries in proton-proton collisions: the role of fragmentation in collinear factorization". In: *Physical Review D* 89.11 (2014), p. 111501.

[42] S. Ozaki and T. Roser. "Relativistic Heavy Ion Collider, its construction and upgrade". In: *Progress of Theoretical and Experimental Physics* 2015.3 (2015), 03A102.

[43] RHIC. *Run overview of the RHIC*. 2018. URL: http://www.rhichome.bnl.gov/RHIC/Runs/.

[44] B.V. Jacak and B. Müller. "The exploration of hot nuclear matter". In: *Science* 337.6092 (2012), pp. 310–314.

[45] I. Alekseev, C. Allgower, M. Bai, et al. *Configuration manual polarized proton collider at RHIC*. Tech. rep. Brookhaven National Laboratory (BNL) Relativistic Heavy Ion Collider, 2006.

[46] A. Zelenski, J. Alessi, B. Briscoe, et al. "Optically pumped polarized H- ion source for RHIC spin physics". In: *Review of scientific instruments* 73.2 (2002), pp. 888–891.

[47] E.D. Courant and H.S. Snyder. “Theory of the alternating-gradient synchrotron”. In: *Annals of physics* 3.1 (1958), pp. 1–48.

[48] V. Bargmann, L. Michel, and V.L. Telegdi. “Precession of the polarization of particles moving in a homogeneous electromagnetic field”. In: *Physical Review Letters* 2.10 (1959), p. 435.

[49] Y.S. Derbenev, A.N. Skrinsky, Y.M. Shatunov, et al. “Radiative polarization: obtaining, control, using”. In: *Particle Accelerator* 8 (1978), pp. 115–126.

[50] H. Wieman. “STAR TPC at Rhic.” In: *APS Division of Nuclear Physics Meeting Abstracts*. 1996.

[51] M. Beddo, E. Bielick, T. Fornek, et al. “The STAR barrel electromagnetic calorimeter”. In: *Nuclear Instruments and Methods in Physics Research Section A: Accelerators, Spectrometers, Detectors and Associated Equipment* 499.2-3 (2003), pp. 725–739.

[52] C.A. Whitten Jr et al. “The Beam-Beam Counter: A Local Polarimeter at STAR”. In: *AIP Conference Proceedings*. Vol. 980. 1. AIP. 2008, pp. 390–396.

[53] W.R. Leo. *Techniques for nuclear and particle physics experiments: a how-to approach*. Springer Science & Business Media, 2012.

[54] R. Wigmans and R. Wigmans. *Calorimetry: Energy measurement in particle physics*. Vol. 107. Oxford University Press, 2000.

[55] Y. Pan. “Measurement of Transverse Single Spin Asymmetries for π^0 and Jets at Large x_F in $\sqrt{\{s\}}$= 500 GeV Polarized Proton Collisions at STAR”. PhD thesis. UCLA, 2015.

[56] F.S. Bieser, H.J. Crawford, G. Engelage J .and Eppley, et al. “The STAR trigger”. In: *Nuclear Instruments and Methods in Physics Research Section A: Accelerators, Spectrometers, Detectors and Associated Equipment* 499.2-3 (2003), pp. 766–777.

[57] C. Dilks. “Longitudinal double-spin asymmetry of forward neutral pions from 510 GeV polarized proton-proton collisions at STAR”.

[58] A. Ogawa. *shower shape width and dgg bias*. 2012. URL: http://www.star.bnl.gov/public/trg/TSL/Software/FMS.pdf.

[59] M. Goldberg, P.L. Mattern, K. Lengweiler, and P.W. Levy. "Radiation induced coloring of Cherenkov counter glasses". In: *Nuclear Instruments and Methods* 108.1 (1973), pp. 119–123.

[60] K.W. Delong, V. Mizrahi, G.I. Stegeman, et al. "Color-center dynamics in a lead glass fiber". In: *Journal of the Optical Society of America B* 7.11 (1990), pp. 2210–2216.

[61] A. Bishay. "Radiation induced color centers in multicomponent glasses". In: *Journal of Non-Crystalline Solids* 3.1 (1970), pp. 54–114.

[62] E.J. Friebele and M.E. Gingerich. "Photobleaching effects in optical fiber waveguides". In: *Applied optics* 20.19 (1981), pp. 3448–3452.

[63] R.J. Araujo. "Kinetics of bleaching of photochromic glass". In: *Applied optics* 7.5 (1968), pp. 781–786.

[64] I. Nakagawa, I. Alekseev, A. Bazilevsky, et al. "p-Carbon Polarimetry at RHIC". In: *AIP Conference Proceedings*. Vol. 980. 1. AIP. 2008, pp. 380–389.

[65] A. Zelenski, A. Bravar, D. Graham, et al. "Absolute polarized H-jet polarimeter development, for RHIC". In: *Nuclear Instruments and Methods in Physics Research Section A: Accelerators, Spectrometers, Detectors and Associated Equipment* 536.3 (2005), pp. 248–254.

[66] I.G. Alekseev, A. Bravar, G. Bunce, et al. "Measurements of single and double spin asymmetry in p p elastic scattering in the CNI region with a polarized atomic hydrogen gas jet target". In: *Physical Review D* 79.9 (2009), p. 094014.

[67] C. Dilks. *Run15 FMS Trigger Rate QA*. 2015. URL: https://www.star.bnl.gov/protected/spin/dilks/trgmon15/200/trigger.html.

[68] O. Eyser. *FMS Run 15 QA (p+p 200 GeV) II*. 2016. URL: https://drupal.star.bnl.gov/STAR/blog/oleg/fms-run-15-qa-pp-200-gev-ii.

[69] C. Kim. *FMS Bit Shift QA*. 2017. URL: https://drupal.star.bnl.gov/STAR/system/files/note_9.pdf.

[70] C. Kim. *Samples for good/bad looking FMS cells*. 2018. URL: https://drupal.star.bnl.gov/STAR/blog/ckimstar/samples-goodbad-looking-fms-cells.

[71] L.K. Eun. "Transverse Single Spin Asymmetries and Cross-Sections for Forward pi0 and eta Mesons at Large xF in sqrt {s}= 200 GeV p+ p Collisions at STAR". In: (2011).

[72] A. Ogawa. *FMS Cluster categorization by Sigma Max*. 2016. URL: https://www.star.bnl.gov/protected/spin/akio/fms2015/sigmax.html.

[73] A.A. Lednev. "Electron shower transverse profile measurement". In: *Nuclear Instruments and Methods in Physics Research Section A: Accelerators, Spectrometers, Detectors and Associated Equipment* 366.2-3 (1995), pp. 292–297.

[74] O. Eyser. *BBC timing calibration*. 2016. URL: https://drupal.star.bnl.gov/STAR/blog/oleg/bbc-timing-calibration-slewing-correction-run-15.

[75] STAR ZDC Polarimetry Group. *ZDC Scaler Polarimetry*, 2011. URL: https://drupal.star.bnl.gov/STAR/blog/bma/geant-cerenkov-summary.

[76] C. Dilks. *STAR note PSN0682:Longitudinal double-spin asymmetry of forward neutral pions from 510 GeV polarized proton-proton collisions at STAR*. Tech. rep. 2018.

[77] A. Ogawa. *shower shape width and dgg bias*. 2012. URL: https://www.star.bnl.gov/protected/spin/akio/fms2017/twopi2/index.html.

[78] F.S. Bieser, H.J. Crawford, J. Engelage, et al. "The STAR trigger". In: *Nuclear Instruments and Methods in Physics Research Section A: Accelerators, Spectrometers, Detectors and Associated Equipment* 499.2-3 (2003), pp. 766–777.

[79] A. De Angelis. "Three-dimensional parametrization of photon-initiated high energy showers". In: *Nuclear Instruments and Methods in Physics Research Section A: Accelerators, Spectrometers, Detectors and Associated Equipment* 271.3 (1988), pp. 455–463.

[80] M. Cacciari, G.P. Salam, and G. Soyez. "FastJet user manual". In: *The European Physical Journal C* 72.3 (2012), p. 1896.

[81] R. Brun, AC. McPherson, P. Zanarini, et al. *GEANT 3: user's guide Geant 3.10, Geant 3.11*. Tech. rep. CERN, 1987.

[82] T. Sjöstrand, S. Mrenna, and P. Skands. "PYTHIA 6.4 physics and manual". In: *Journal of High Energy Physics* 2006.05 (2006), p. 026.

[83] J. Pumplin, D. R. Stump, J. Huston, et al. "New generation of parton distributions with uncertainties from global QCD analysis". In: *Journal of High Energy Physics* 07 (2002), p. 012.

[84] RHIC Spin Group. *Final Results for RHIC polarized pp data analysis*. 2012. URL: https://wiki.bnl.gov/rhicspin/Run_11_polarization.

[85] RHIC Spin Group. *Final Results for RHIC polarized pp data analysis*. 2016. URL: https://wiki.bnl.gov/rhicspin/Run_15_polarization.

[86] Chang Z. *Example calculation of fill-to-fill polarization uncertainties*. 2016. URL: https://wiki.bnl.gov/rhicspin/upload/1/1c/ExampleFillToFill.pdf.

[87] The Polarimetry Group. *RHIC polarization for Runs 9-15*. 2016. URL: https://wiki.bnl.gov/rhicspin/upload/e/e4/Pol_resultsMay2016.pdf.

[88] B. I. Abelev et al. "Forward Neutral Pion Transverse Single Spin Asymmetries in p+p Collisions at s**(1/2) = 200-GeV". In: *Physical Review Letter* 101 (2008), p. 222001.

[89] L. C. Bland et al. "Cross Sections and Transverse Single-Spin Asymmetries in Forward Jet Production from Proton Collisions at $\sqrt{s} = 500$ GeV". In: *Physics Letters B* B750 (2015), pp. 660–665.

[90] M. Anselmino, U. D' Alesio, and S. Melis. "Transverse single-spin asymmetries in proton-proton collisions at the AFTER@ LHC experiment in a TMD factorisation scheme". In: *Advances in High Energy Physics* 2015 (2015).

[91] M. Anselmino, M. Boglione, U. D' Alesio, et al. "Extracting the Sivers function from polarized semi-inclusive deep inelastic scattering data and making predictions". In: *Physical Review D* 72.9 (2005), p. 094007.

[92] M. Anselmino, M. Boglione, U.o D' Alesio, et al. "Transversity and Collins functions from SIDIS and e+ e- data". In: *Physical Review D* 75.5 (2007), p. 054032.

[93] M. Anselmino, M. Boglione, U. D' Alesio, et al. "Sivers effect for pion and kaon production in semi-inclusive deep inelastic scattering". In: *The European Physical Journal A* 39.1 (2009), pp. 89–100.

[94] M. Anselmino, M. Boglione, U. D'Alesio, et al. "Update on transversity and Collins functions from SIDIS and e+ e- data". In: *Nuclear Physics B (Proceedings Supplements)* 191 (2009), pp. 98–107.

[95] M. Glück, E. Reya, and A. Vogt. "Dynamical parton distributions revisited". In: *The European Physical Journal C-Particles and Fields* 5.3 (1998), pp. 461–470.

[96] D. de Florian, R. Sassot, and M. Stratmann. "Global analysis of fragmentation functions for protons and charged hadrons". In: *Physical Review D* 76.7 (2007), p. 074033.

[97] S. Kretzer. "Fragmentation functions from flavor inclusive and flavor tagged e+ e- annihilations". In: *Physical Review D* D62 (2000), p. 054001.

[98] L. C. Bland. "Transverse Single Spin Asymmetries in Hadronic Interactions: an experimental overview and outlook". In: *EPJ Web Conference* 85 (2015), p. 01008.

[99] M. Anselmino, M. Boglione, U. D'Alesio, et al. "Sivers effect and the single spin asymmetry A_N in $p^{\uparrow}p \to hX$ processes". In: *Physical Review D* 88 (5 2013), p. 054023.

[100] L. Gamberg, Z. Kang, and A. Prokudin. "Indication on the Process Dependence of the Sivers Effect". In: *Physical Review Letter* 110 (23 2013), p. 232301.

[101] A. Airapetian, N. Akopov, Z. Akopov, et al. "Single-spin asymmetries in semi-inclusive deep-inelastic scattering on a transversely polarized hydrogen target". In: *Physical Review Letter* 94.1 (2005), p. 012002.

[102] O. Martin, A. Schäfer, M. Stratmann, and W. Vogelsang. "Soffer' s inequality and the transversely polarized Drell-Yan process at next-to-leading order". In: *Physical Review D* 57.5 (1998), p. 3084.

Acknowledgment

回想当初决定来山大念研究生的决定，眨眼之间7年便已过去。还记得2013年4月份到济南复试时是雨天，凌晨三四点下飞机来到的泉城广场，人冷得发抖。如今辗转三地，风尘仆仆，安坐家中等候毕业的当下，让人不敢相信竟然已是快七年光景。回头看来，身边的人与事都变化万千，而个人也经历了一轮又一轮的挑战。当初选择粒子物理作为研究方向，是我顺从内心呼唤的选择。能与世界上众多出色的科学家一起，探索世界的本源，即便在今天想来，也觉得是不可思议，激动人心。在此之后，便是许多许多的得得失失：有过孤立无援困苦，也有过少有所得的轻快；少不了对未来的担忧与迷惑，但又磕磕碰碰的坚持了下来；面临过被腰斩的危机，也有过心想事成的幸运。总的来说，还是十分感恩各种机会，各种人事。

在这七年里，我从当初无知莽撞的年轻人，渐渐成长为能够独当一面的博士生。我首先要感谢我的导师徐庆华教授，在我进入山大学习期间一直孜孜不倦的教导我，不仅是在学术上对我悉心指导，还在生活上给我无微不至的关怀。无论是我在专业上感到困惑，还是在毕业的最后阶段疲倦无力，徐老师都尽力帮助我和理解我，他的支持是我永远难以忘怀的。我要感谢在美国期间我的合作导师elke-Caroline Aschenauer博士，在布鲁克海文期间，在她身边工作让我在学业上取得了长足的进步。她总是在我在工作上遇到困难的时候给我信心和指导。她的乐观豁达总是让我钦佩。

我要感谢粒子组里各位老师，他们渊博的知识和严谨的治学态度让我获益良多，包括梁作堂教授，徐长补教授，祝成光教授，黄性涛教授，李世渊教授，焦健斌教授，马连良教授，吴群教授，王萌教授，李海峰教授，鲍守山副教授，董辉副教授，邓建副教授等。我要感谢实验室里与我一起，在大事小事上对我帮助甚多的各位同学，分别有杨钱博士，聂茂武博士，张金龙博士，梅金成博士，沈付旺博士，王帅博士，田野，苟兴瑞，陈佳，李长丰等。我要感谢研究生期间与我相处两年的室友梁辉，蒋佳和董文正，让我收获了宝贵的友谊。我要感谢众多在学术上和生活上帮助过我的，来不及一一列明的太多太多人。

最后我要感谢我敬爱的父亲，母亲和兄长，这些年来漂泊在外，很多事情上无法照顾他们，让我心感惭愧。而他们多年以来却是对我毫无保留的支持与照顾，让我能够走到博士毕业这一天。